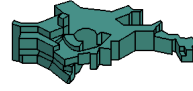




Technische Universität München



Max-Planck-Institut für Astrophysik

Fakultät für Physik

Multi-Dimensional Simulations of Convective Core Hydrogen Burning

Johann Higl

Vollständiger Abdruck der von der Fakultät für Physik der Technischen Universität München zur Erlangung des akademischen Grades

Doktor der Naturwissenschaften (Dr. rer. nat.)

genehmigten Dissertation.

Vorsitzende/-r:	Prof. Dr. Lothar Oberauer
Prüfer der Dissertation:	1. apl. Prof. Dr. Ewald Müller
	2. Prof. Dr. Alejandro Ibarra

Die Dissertation wurde am 14.10.2019 bei der Technischen Universität München eingereicht und durch die Fakultät für Physik am 22.11.2019 angenommen.

Abstract

The lifetime of stars is determined by the available amount of hydrogen in the central nuclear burning region. Convective motions inside stellar cores can mix hydrogen from the envelope into the burning region and prolong the star's life. The inclusion of these processes in one dimensional stellar evolution calculations requires an appropriately parametrized mixing model, which has to be tested against multi-dimensional hydrodynamic simulations. Due to the exceptionally subsonic flows in stellar interiors, specialized low Mach number simulations are required to investigate the magnitude and extent of convective mixing events, and to estimate their effects on the much longer timescales of stellar evolution.

The hydrodynamical simulations in this study show that the region of mixed zones in the interior of stars should extend beyond the convective boundary set by stability considerations. Comparing two and three dimensional simulations it is shown that two dimensional simulations provide an acceptable approximation for the mixing at convective boundaries. Therefore, a series of two dimensional simulations is used to restrict the parameters and applicability of one dimensional mixing models.

Zusammenfassung

Die Lebensdauer von Sternen wird bestimmt durch die zur Verfügung stehende Menge an Wasserstoff in der zentralen nuklearen Brennzone. Konvektive Strömungen im Zentrum von Sternen können Wasserstoff aus der Hülle in die Brennzone mischen und das Leben des Sterns verlängern. Diese Prozesse in eindimensionalen Sternentwicklungsberechnungen einzubeziehen setzt ein passend parametrisiertes Mischungsmodell voraus, welches in mehrdimensionalen Simulationen verifiziert werden muss. Aufgrund der aussergewöhnlich subsonischen Strömungen im Sterninneren ist es nötig, Simulationen durchzuführen, die auf niedrige Mach Zahlen abgestimmt sind, um den Umfang und die Ausdehnung des Mischens an konvektiven Grenzen sowie dessen Einfluss auf die Sternentwicklung, die sich auf deutlich längeren Zeitskalen abspielt, zu untersuchen.

Die hydrodynamischen Simulationen, die in dieser Arbeit vorgestellt werden, machen deutlich, dass der gemischte Bereich an konvektiven Grenzen größer sein sollte als aufgrund von Stabilitätskriterien vorhergesagt. Indem zwei- und dreidimensionale Simulationen verglichen werden, wird gezeigt dass zweidimensionale Simulationen eine ausreichende Näherung für das Mischen an konvektiven Grenzen darstellen. Deswegen wird eine Reihe von zweidimensionalen Simulation genutzt, um die Parameter und Verwendbarkeit von eindimensionalen Mischungsmodellen einzuschränken.

Contents

1 Motivation	1
2 Stellar Mixing Processes	5
2.1 Mixing Length Theory	5
2.2 Overshooting	8
2.3 Internal Gravity Waves	14
2.4 Entrainment	16
3 Low Mach Number Hydrodynamics	21
3.1 Euler Equations	21
3.2 Timescales	27
3.3 Sound-proof Methods	29
3.4 MAESTRO	32
3.5 Code Verification	38
3.6 Initial Models	47
4 2D Simulations	53
4.1 Transient	53
4.2 Convective Boundary	61
4.3 Internal Gravity Waves	66
4.4 Overshooting Calibration	69
4.5 Entrainment	83
4.6 Temperature Gradients	87
4.7 Mass Dependence	91
5 3D simulations	105
5.1 Transient	105
5.2 Flow Field	115
5.3 Convective Boundary	118
5.4 Mixing	120
6 Conclusion and Outlook	125
Bibliography	131

Chapter 1

Motivation

The structure and dynamics of turbulent flows have been described by Prandtl (1926) as "unpleasantly complicated" and despite almost a century of continuous research this statement is still true today. In astrophysical plasmata like in stars the complexity increases even further. To understand the influence of turbulent convective motions on stellar evolution it is necessary to consider the effects of small scale turbulence on structures that are many orders of magnitude larger than that. Furthermore it is known that stellar convective motions usually change on timescales of months to years. On the other hand, stellar structures evolve on timescales of millions to billions of years.

This separation of scales makes it impossible to include precise models of turbulence in stellar evolution calculations.

One dimensional stellar evolution models therefore use approximations to the intrinsically 3D processes of turbulent convection. The most commonly used convection model is the so-called Mixing-Length-Theory (MLT) (Böhm-Vitense, 1958). It assumes that convection can be simplified in terms of mass elements that are accelerated over a certain distance — the mixing length — before they dissipate in their surrounding.

Due to the reduction of a three dimensional process to an one dimensional model some information is lost. While MLT provides an acceptable model for the energy transport in convectively unstable regions, it fails to provide accurate information about the chemical mixing around the boundaries of unstable regions. The actual size of the mixed region associated with a convective zone (CZ) can therefore not be recovered from MLT.

Comparing observations of eclipsing binary systems and populations of stellar clusters with MLT models one finds indications that the mixed region around CZs should be larger than the CZ itself. Recently asteroseismological observations have become sensitive enough to identify oscillations on stellar surfaces that are connected to the stellar structure near the core region of certain stars. These observations confirm the need for an enlarged mixing layer around CZs.

In stellar evolution this effect is usually called overshooting and several parametrized one dimensional models exist. However, due to the uncertainties of the observations it is currently not possible to calibrate these free parameters reliably.

Arguably the most important CZ in stars more massive than $\approx 1.2M_{\odot}$ is their central CZ during core hydrogen burning on the main sequence. It is not only the most persistent CZ, existing for $\approx 90\%$ of the stars total lifetime, the mixed region associated with it also influences the lifetime directly by defining the amount of fuel available for the fusion process. The uncertainty of the size of convective cores from observations leads to an uncertainty of a star's age of up to 30%. Moreover, an increased amount of fuel will also lead to a more massive He-core at the end of the main sequence which will influence the star's remaining life significantly, e.g., whether a star becomes a Cepheid during its He-burning phase, and might even determine the end product of stellar evolution.

Over the years the development of new numerical tools and the continuous growth in computational power made it possible to follow stellar turbulence in numerical simulations for several convective turnover times. While this is very small compared to the evolutionary timescale, early two dimensional simulations (e.g., Freytag et al., 1996) of stellar surfaces already improved our understanding of the overshooting process in convective envelopes.

However, a CZ on the surface is fundamentally different from an interior CZ. The main difference is the driving mechanism of convection. Interior CZs are driven by the heat release of nuclear fusion, while outer CZs are mostly powered by the loss of energy through radiation at the surface of stars (Spruit, 1997). Furthermore, interior CZs also have a stiffer convective boundary and tend to be more shallow than surface CZs.

All this makes it very questionable to use the same approximation for interior and surface CZs. Yet it is still common practice to assume that all CZs in all types of stars follow the same convection and overshooting model with the same parameters.

Rather recently it has also become possible to perform three dimensional simulations of CZs in the deep interior of stars (e.g., Meakin & Arnett, 2007; Herwig et al., 2007). However, these simulations only cover a small number of convective timescales due to the low Mach number flows in these kinds of CZs. In fact, in most of the simulations the energy input had to be increased by a large factor to boost the velocities and consequently reduce the convective timescales. It is questionable if such fundamental modifications to the input physics will provide physically relevant answers.

Specialized low Mach number codes like MAESTRO have the capability to perform simulations of stellar interiors over many convective turnover times with the actual

energy input at reasonable computational cost, i.e, these type of codes are appropriate tools to investigate the effects of the short term evolution of convection on the long term evolution of stars.

Using the MAESTRO code, this study will investigate the mixing in convective hydrogen burning cores of intermediate mass stars between 1.3 and $3.5 M_{\odot}$ in two and three dimensional hydrodynamic simulations. The goal is to define the size of the homogeneously mixed core and to reduce the uncertainty of overshooting parameters. These simulations will also allow to identify the dominant mixing processes. Besides the chemical mixing this also includes the mixing of entropy and the resulting consequences for the temperature stratification around the convective boundary. Comparing the long term simulations with mixing models proposed from short term simulations will also give new insight on the applicability of such models in one dimensional stellar evolution models.

This thesis is structured in the following way:
Chapter 2 will introduce the important turbulent mixing processes in stars and how they are treated in one dimensional stellar evolution. The numerical tools necessary to study main sequence convection will be discussed in Chap. 3. The Chapters 4 and 5 will then analyse results of two and three dimensional simulations, respectively. The final Chapter 6 will summarize the results and give an outlook on possible future developments.

Chapter 2

Stellar Mixing Processes

Dynamical mixing processes in stars are intrinsically multi dimensional processes. In order to include them in a 1 dimensional model they need to be parametrized. In this chapter we discuss how this is and can be done for non-rotating stars without magnetic fields.

2.1 Mixing Length Theory

The transport of energy by convection in 1D stellar evolution codes is usually described by rising and sinking blobs in the so called Mixing-Length-Theory (MLT). The concept is based on Prandtl (1926), who defines two characteristic length scales of convective motion. One is set by the characteristic size of a single convective element (a blob of mass), and the other is the average distance such an element can travel, before it mixes with neighbouring elements. In the MLT the latter one is referred to as the "mixing length" α and can be interpreted as a blob's mean free path.

In pressure equilibrium convective blobs start rising (sinking) when their temperature is higher (lower) than their surrounding due to buoyancy. In the process the blobs will expand (contract). Comparing the blob's new density with the surrounding density, buoyancy force now either continues to point in the direction of the motion, creating an unstable layer, or back to the blob's original position, stabilizing the flow.

Assuming that blobs rise adiabatically while maintaining pressure equilibrium with their surrounding, it is possible to derive a stability criterion based on the temperature gradients $\nabla = \frac{d \log T}{d \log P}$ involved in the process. ∇ can be defined based on the temperature T and pressure P of the blob (∇_b), the surrounding (∇), the radiative energy transport (∇_{rad}), and the local adiabat (∇_{ad}).

The famous Schwarzschild criterion requires $\nabla_{\text{ad}} < \nabla_b$ for a convectively unstable layer. Since $\nabla_b \leq \nabla_{\text{rad}}$ (Vitense, 1953), this is equivalent to $\nabla_{\text{ad}} < \nabla_{\text{rad}}$, which is the more commonly used version.

Based on this picture, the energy transport can now be expressed in terms of the energy flux F through a mass shell in a star. Following the formulation of Böhm-Vitense (1958) one can split F into a convective F_{conv} and a radiative F_{rad} part. F_{conv} describes the energy excess of convective blobs as they pass through a shell and F_{rad} gives the energy transported by radiation. The fluxes can be computed based on the temperature perturbation of the convective blob ΔT and ∇ , which is initially unknown

$$F_{\text{conv}} = \rho v c_p \Delta T \quad (2.1)$$

$$F_{\text{rad}} = \frac{4acG}{3} \frac{T^4 m}{\kappa P r^2} \nabla \quad (2.2)$$

$$F = F_{\text{conv}} + F_{\text{rad}}. \quad (2.3)$$

Here ρ , κ , c_p , and v are the density, opacity, specific energy, and velocity of the convective blob respectively. c , G , and a are the speed of light, gravitational constant and radiation density constant respectively. r is the radius of the mass shell with mass coordinate m .

ΔT can be related to ∇ and ∇_b if one assumes that on average a convective blob has passed half of its mixing length when it passes through the shell.

$$\frac{\Delta T}{T} \approx (\nabla - \nabla_b) \frac{\alpha}{2H_p}, \quad (2.4)$$

where $H_p = -dr/d \ln P$ is the local pressure scale height of the shell.

Convective blobs are accelerated by buoyancy and therefore gain kinetic energy while moving. The buoyancy force depends on the density perturbation of the blob $\Delta \rho$. In pressure equilibrium $\Delta \rho / \rho$ is directly proportional to $\Delta T / T$. The proportionality factor is Q . Using equation 2.4 and assuming that $Q(\nabla - \nabla_b) / H_p$ as well as the gravitational acceleration g are constant over one mixing length, the average velocity of a blob can be written as

$$\bar{v}^2 = gQ \frac{\alpha^2}{4H_p} (\nabla - \nabla_b) \quad (2.5)$$

Using equations 2.5 and 2.4 and putting them back into 2.1, one finds that

$$F_{\text{conv}} \propto v^3, \quad (2.6)$$

which is a relationship that can easily be tested by hydrodynamical simulations of convection (see 3.5).

In order to close the system of equations, one can look at the ratio of temperature gradients in different situations. Neglecting the energy exchange E_{rad} of a blob

with its surrounding is equivalent to $\nabla_b = \nabla_{ad}$, i.e., the element is expanding adiabatically. If there is an energy exchange due to an energy excess (deficiency), it will be proportional to the difference $\nabla_{ad} - \nabla_b$, because the blob will try to establish an adiabatic gradient. On the other hand an element is also gaining energy due to its increasing velocity. This energy increase E_{excess} is proportional to $\nabla_b - \nabla$. Combining these two proportionalities one can define the ratio of energy excess to energy loss as

$$\frac{E_{\text{excess}}}{E_{\text{rad}}} = \frac{\nabla_b - \nabla}{\nabla_{ad} - \nabla_b}. \quad (2.7)$$

A blob can exchange energy with its surrounding via radiation on its surface S . The energy loss E_{rad} of a spherical blob with diameter d can then be written as

$$E_{\text{rad}} = \frac{8acT^3}{3\kappa\rho} \Delta T \frac{S}{d}. \quad (2.8)$$

In a convectively unstable region ΔT will monotonically increase during the lifetime of a blob, until it reaches ΔT_{max} , before it mixes with the surrounding. Assuming that the initial ΔT is much smaller than ΔT_{max} , the radiative losses can be best described when ΔT in equation 2.8 is replaced by an average $\bar{\Delta T} = 0.5\Delta T_{\text{max}}$.

At the end of its lifetime the blob will release its energy excess E_{excess} into the surrounding fluid. The amount of energy is proportional to the volume of the blob V

$$E_{\text{excess}} = c_p \rho \Delta T_{\text{max}} V v. \quad (2.9)$$

Following Böhm-Vitense (1958) one can assume that convective blobs have a typical surface to volume ratio of 6/1. The energy balance of blobs can then be written as

$$\frac{E_{\text{excess}}}{E_{\text{rad}}} = \frac{\kappa \rho^2 c_p d v}{6acT^3}. \quad (2.10)$$

Assuming that the typical size of a convective blob corresponds to the mixing length ($d = \alpha$), equations 2.1, 2.2, 2.3, 2.5, and 2.10 form an equation system for the 5 unknowns F_{conv} , F_{rad} , \bar{v} , ∇ , and ∇_b .

The only free parameter remaining is α , which is calibrated to match our Sun, as the best observed star. To do that a stellar model with $1M_{\odot}$ and solar metallicity needs to reproduce the solar radius and luminosity after 4.7 Gyr. By this way one finds typical values for α between ≈ 1.7 and ≈ 2.1 (see, e.g., Weiss & Schlattl, 2008; Magic et al., 2010).

This study focuses on convective core hydrogen burning, where $\nabla - \nabla_{ad} < 10^{-8}$ is a typical value. This implies that $\nabla - \nabla_b < 10^{-8}$, which will be important for the simulation setup (see 3.6).

To derive the MLT equations it was necessary to make two basic assumptions: First convective blobs were assumed to be in pressure equilibrium with their surrounding at all times. Pressure is equilibrated by sound waves propagating in the medium. MLT predicts that in the deep interiors of stars convection is highly subsonic. We will see in the simulations presented in Chapters 4 and 5 that this is actually the case. This means that the sound crossing timescale is much smaller than the convective timescale and thus sound waves can establish pressure equilibrium before significant convective energy transport occurs.

Second convective blobs were assumed to move adiabatically, i.e. that they don't exchange energy with their surrounding during their motion. Adiabatic expansion is only justified if the blobs are assumed to be big enough, such that their surface is small compared to their volume. The size is, however, also limited by the assumption that a blob only has small variations in temperature, pressure, etc. This limits the size of a blob to the respective scale height.

For large Reynolds Numbers Re the size of a blob and its mixing length only differ by a constant factor (Prandtl, 1926).

$$Re = \frac{v\rho\alpha}{\eta} \quad (2.11)$$

where v is the typical velocity of a convective blob, ρ is its density and η is the viscosity of the surrounding fluid. In stellar environments η is close to zero, such that Re is expected to have values of the order of 10^{15} . Which characterises an extremely turbulent flow.

MLT is a time independent theory and thus it can only represent a snapshot of a "frozen-in" convection. Due to the large separation in timescales between convective motions and nuclear evolution, this approach is in most cases an acceptable assumption. The simulations shown in Chapter 4 and 5 show that most convective properties can be well described by time and space averaged quantities. The short term variations only become relevant, when the convective and evolutionary timescales become comparable, as it is for example the case for Si-burning shortly before a massive ($\gtrsim 8M_{\odot}$) star collapses and ends its life in a supernova.

2.2 Overshooting

MLT was constructed to describe the convective energy transport in stars, but since it provides estimates of the convective velocities it can also be used to predict the chemical mixing in CZs. Considering that the convective timescale (i.e., the radial

extent of a CZ divided by the MLT velocity) in a typical CZ is much smaller than the evolutionary timescale, it is justified to treat the chemical mixing as instantaneous. In fact, a homogeneous composition profile is expected for almost all stellar CZs. However, when the evolutionary and convective timescales become comparable it can be beneficial to treat the chemical mixing as a diffusive process in order to couple it directly with the nuclear burning inside the CZ. Using the MLT estimated convective velocities a diffusion coefficient can be derived. In convective cores on the main sequence the diffusion coefficient has typical values of $10^{13} \text{ cm}^2/\text{s}$. At the interface to an adjacent stable layer, however, MLT has less predictive power in terms of chemical mixing.

In a stable layer a blob with an energy excess will start to rise, but buoyancy will soon pull it back to its original position. It therefore does not gain any extra energy, but instead starts radiating away the energy excess. The blob does that until $\nabla_b = \nabla$. According to equation 2.5 this situation corresponds to $v = 0$. MLT therefore predicts that the velocity drops to exactly zero, once a stable layer is reached. This also means that blobs that start, e.g., half a mixing length inside the CZ, will accelerate until they reach the boundary and then suddenly stop. Already Böhm-Vitense (1958) pointed out that this is a problematic finding and that convective boundaries require special treatment.

In a realistic scenario one would expect that blobs that get accelerated towards the boundary will travel into the stable layer. Buoyancy is now pointing in the opposite direction, decelerating the blob and finally pulling it back into the CZ. This so called ballistic overshooting will not only lead to non-zero velocities in the vicinity of a convective boundary, but will also drag some matter from the stable layer into the CZ. Ballistic overshooting is the main driving effect of extended mixing around convective zones in shallow convective envelopes (Freytag et al., 1996; Pratt et al., 2017).

Convective boundaries deep inside of stars, however, are much stiffer. This means that blobs will be pulled back quicker. Lattanzio et al. (2017) gives an estimate for the mixing depth of ballistic overshooting, by comparing the energy budget of a mass element that penetrates the convective boundary, with the restoring buoyancy force. Integrating the forces, they determined an upper limit of overshooting in deep stellar envelopes that is smaller than the usual resolution of 1D models. The same is true if one uses the same argument for convective cores or shells. Nevertheless observations of the width of the main sequence in young open clusters can only be explained by an extended mixed region around convective cores in intermediate mass stars between 2 and $9M_{\odot}$ (Maeder & Mermilliod, 1981). Reproducing the shape of the main sequence turnoff in old open clusters with stellar models also requires some ex-

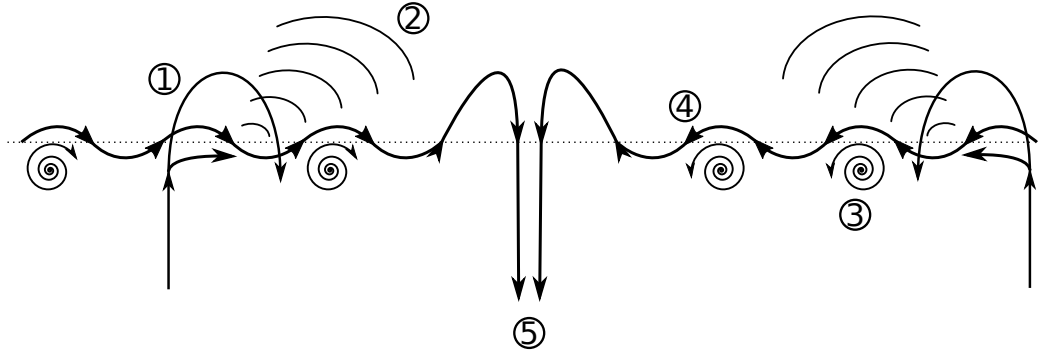


Figure 2.1: Schematics of mixing at convective boundaries, where each number indicates a different mixing process (see text).

tra mixing in the range of $1 - 2M_{\odot}$ (see, e.g., Aparicio et al., 1990; Bertelli et al., 1992).

Therefore, mixing deep inside of stars has to be driven by other processes. Fig. 2.1 gives an overview of different mixing processes that can occur at convective boundaries.

To describe other mixing processes it is easier to relax the MLT picture of blobs into flows of mass. If a flow of mass hits a convective boundary it will initially penetrate it (1 in Fig. 2.1). Besides the ballistic overshooting, the stream will also launch a set of internal gravity waves (IGW; 2 in Fig. 2.1) as each blob in the stream starts to oscillate around the boundary due to buoyancy. 2.3 is discussing the properties and mixing effects of IGWs in more detail. 4.3 will show that IGWs also play an important role in interpreting our simulation results.

A continuous flow will pile up at the boundary and start to deflect the remaining stream sideways, converting radial into tangential velocities. 4.2 will show that the tangential velocity profile is therefore a good indicator for the position of the convective boundary. A flow that is shearing along the convective boundary can set off Kelvin-Helmholtz instabilities (3 in Fig. 2.1).

Shear flows that remain stable will most likely produce a surface gravity wave (4 in Fig. 2.1). A surface wave lets the whole boundary oscillate around its equilibrium point. As such it does not produce any mixing. However, if two surface waves of opposing direction run into each other, they will pile up and finally break (5 in Fig. 2.1).

In that process matter from the stable layer will be entrained into the convective zone.

In 1D stellar evolution, all these effects are combined into a single parameter, that describes the mixing around the CZ.

In modern 1D codes there are two main implementations of overshooting. The classic one simply extends the CZ by a fixed fraction α_{ov} of H_p . α_{ov} is a free parameter and needs to be calibrated based on observation.

Based on simulations of convective envelopes of A stars Freytag et al. (1996) came up with a more physical approach that defines the additional mixing in a diffusive fashion. In their simulations Freytag et al. (1996) found that the diffusion constant D decreases exponentially as a function of the distance to the convective boundary z .

$$D(z) = D_0 \exp \frac{-2z}{f_{ov}H_p}, \quad (2.12)$$

where D_0 is the diffusion constant at the convective boundary and f_{ov} is the free parameter of this theory.

Empirical estimates typically give $f_{ov} \approx 0.02$ corresponding to $\alpha_{ov} \approx 0.2$ (see e.g., Ventura, 2007), but many observables can also be reproduced without any overshooting (Pols et al., 1997; Valle et al., 2016) at all, leaving us with large errorbars on the overshooting parameters (Lastennet & Valls-Gabaud, 2002; Constantino & Baraffe, 2018). Simulations also produce a rather large range of inferred overshooting parameters ranging from 0.2 to $0.5H_p$ (see, e.g., Pratt et al., 2017; Edelmann et al., 2019; Freytag et al., 1996).

More recent simulations of convective envelopes from different groups showed that simulation data can be interpreted in a variety of ways and that the mixing properties can be explained by several functional forms. For example Pratt et al. (2017) used statistical arguments of ballistic overshooting to derive that the diffusion constant D should decline as an exponential of an exponential (Gumbel-profile) rather than Eq. 2.12. Korre et al. (2019) on the other hand argued that the mixing should have a Gaussian shape based on simulations of the solar envelope.

Here it should be noted that surface convective zones, as used to determine the diffusive overshooting model, are fundamentally different from core convective zones. In the surface layers the temperature gradient is partially superadiabatic, while in the central regions, convective zones are always very close to being adiabatic as predicted by MLT. This suggests that surface convective zones are much more vigorous than internal CZs and that the properties of the convective flow is dominated by the superadiabatic boundary (see Freytag et al., 1996).

Furthermore, Spruit (1997) argues that surface convection is mainly driven by the cooling from the surface layer, which was confirmed in numerical simulations by Käpylä et al. (2017). Viallet et al. (2013) find that in convective envelopes a

significant amount of kinetic energy is transported by pressure fluctuations. Interior CZs, on the other hand, are driven by internal heating and the buoyancy terms are the dominating energy transport mechanism (Viallet et al., 2013). So, from first principles there is no reason why internal CZs should have the same overshooting behaviour as surface CZs.

Yet again Moravveji et al. (2016) finds that an overshooting prescription like in 2.12 fits asteroseismic observations of a $3.2M_{\odot}$ mass star best in the immediate vicinity of the convective boundary.

The study, however, also shows that asteroseismic observations can be reproduced even better, if an additional weak mixing process is included far away from the boundary. In the literature one can find different forms of such an extended mixing region, starting with a constant (diffusive) mixing by some undefined process (Moravveji et al., 2016) up to a more realistic diffusive mixing profile based on IGWs Rogers & McElwaine (2017).

All the overshooting descriptions mentioned above, parametrize the extend of the mixed region in terms of H_p . This leads to problems when we deal with convective zones that extent less than a pressure scale height. 2.12 would predict that the CZ is surrounded by a significantly enlarged mixed region. It is unclear which mixing process could be responsible for that. This problem becomes severe in small convective cores. H_p diverges towards the centre of a star and therefore low mass stars ($\approx 1.2M_{\odot} - \approx 2.0M_{\odot}$) will show an extreme mixed area on the main sequence. With $f_{ov} = 0.02$, the mixed region of a $1.3M_{\odot}$ star is ≈ 7 times more massive than the CZ. Since mixing is essentially instantaneous this directly translates into an increased main sequence lifetime by a factor of 7 (see Fig. 4.25).

One way around this problem is to use a mass dependent overshooting parameter. Claret & Torres (2016, 2017) found a linear trend with mass for their overshooting parameter by matching observations of eclipsing binaries with 1D models and confirmed it in consecutive papers (Claret & Torres, 2018, 2019). They identified the critical mass range to be $1.2 - \approx 2.0M_{\odot}$. The mass dependency is, however, challenged by other groups that do not see such a strict relation, mostly because the error bars on the estimated overshooting parameters are too large to make any qualitative statement (see, e.g., Deheuvels et al., 2016; Constantino & Baraffe, 2018; Stancliffe et al., 2015).

Another way to limit the overshooting to realistic values is to restrict the mixed region based on the extent of the CZ ΔR_{CZ} itself. Theoretical estimates of the energy budget by Roxburgh (1992) defined an upper limit of the overshooting area of less than $0.2\Delta R_{CZ}$ in the limit of vanishing convective cores. Magic et al. (2010) introduced a more general limit by replacing H_p with \tilde{H}_p in 2.12, where \tilde{H}_p is defined

as

$$\tilde{H}_p = H_p \cdot \min \left[1, \left(\frac{\Delta R_{CZ}}{2H_p} \right)^2 \right]. \quad (2.13)$$

Overall this approach gives good agreement with cluster ages (Magic et al., 2010), but seems to be too restrictive in the region around $2M_\odot$ (Higl et al., 2018).

So far the overshooting descriptions were only used to quantify the chemical mixing across convective boundaries. Mixing by dynamical effects, however, also carries some convective energy. This will also lead to an energy transport by convection in the stable layer, which will alter the temperature gradient there. Böhm-Vitense (1958) assumed that these changes to the temperature stratification are negligible and therefore the radiative temperature gradient should be used in the overshooting region.

Zahn (1991) describes the situation differently. He divides the mixing at convective boundaries into two regimes. In a region beyond the formal Schwarzschild boundary the convective flow is still very efficient in transporting heat even though the radiative diffusion would already be able to transport all the energy. In order to keep the energy balance, radiative diffusion needs to be limited, which is done by increasing the temperature gradient to an almost adiabatic one. This is what he calls the penetration regime. Further away from the convective boundary radiative diffusion finally takes over the energy transport, since the convective flow is no longer efficient. The convective flow, however, can still mix elements without altering the temperature stratification. This is what he calls overshooting, in agreement with our 1D models where the overshooting region is set by f_{ov} and only influences the mixing of elements. In simulations of red giants Viallet et al. (2013) indeed identified such a penetration layer, where $\nabla > \nabla_{rad}$. It is, however, difficult to make a reliable prediction from these kind of simulations, because they do not cover a thermal timescale, which is needed to adjust the temperature stratification based on the energetic and structural changes due to convection.

Penetration layers have also been found in simulations of the solar envelope (Korre et al., 2019), and in stellar evolution models that are using one dimensional averages of the hydrodynamical equations instead of MLT (Li, 2017).

This makes it necessary to distinguish between the convective region defined by the Schwarzschild boundary, and the mixed region defined by the composition gradient. The latter one provides the fuel for the nuclear burning that drives convection.

2.3 Internal Gravity Waves

Internal gravity waves (IGW) have already been introduced in 2.2 as one of the mixing processes at convective boundaries. Here their properties and diagnostic character are discussed in more detail.

IGWs are produced if a mass element is displaced in a stable stratification. Buoyancy will accelerate the mass element until it reaches its original position, but its inertial momentum will move it beyond its initial stable position. Now Buoyancy will work in the opposite direction. The mass element will first decelerate, then accelerate towards the stable position and finally overshoot. This process repeats with the mass element oscillating around its stable position. This gives IGWs a characteristic frequency, called the Brunt-Väisälä, or buoyancy frequency N which can be calculated based on the gravitational acceleration g

$$N^2 = -\frac{g\xi_T}{\xi_\rho H_p} \left(\nabla_{ad} - \nabla - \frac{\xi_\mu}{\xi_T} \nabla_\mu \right). \quad (2.14)$$

Here $\nabla_\mu = d \ln \mu / d \ln p$ is the molecular gradient and $\xi_\rho = \partial \ln p / \partial \ln \rho|_{T,\mu}$; $\xi_\mu = \partial \ln p / \partial \ln \mu|_{\rho,T}$; $\xi_T = \partial \ln p / \partial \ln T|_{\rho,\mu}$ are quantities derived from an equation of state (EOS).

Displacing a mass element in the direction of gravity, will lead to a wave with frequency $\omega = N$. If the mass element, however, is displaced at an angle Θ with respect to gravity, one finds

$$\omega = N \cos(\Theta) = N \frac{|\mathbf{k}_\perp|}{|\mathbf{k}_\parallel + \mathbf{k}_\perp|}, \quad (2.15)$$

where \mathbf{k}_\parallel and \mathbf{k}_\perp are the wave vectors parallel and perpendicular to the gravity vector, respectively.

Therefore N represents an upper limit for the frequency an IGW can have. From 2.15 one can see that one characteristic of IGWs is that their phase velocity ($\mathbf{v}_{ph} = (\omega/|\mathbf{k}|^2) \cdot \mathbf{k}$ with $\mathbf{k} = \mathbf{k}_\parallel + \mathbf{k}_\perp$) is perpendicular to their group velocity ($\mathbf{v}_{gr} = \nabla_{\mathbf{k}} \omega$, where $\nabla_{\mathbf{k}}$ is the gradient operator with respect to \mathbf{k}). This makes it possible to distinguish IGWs from pressure waves.

N^2 can also be used to characterize the stability of a layer. $N^2 > 0$ represents a stable layer, while $N^2 < 0$ is convectively unstable, i.e., no IGWs are allowed inside of CZs.

IGWs can be found in many geophysical circumstances. For example, they have been found to be of importance for the mixing of deep ocean layers (Mashayek et al., 2017) as well as the quasi-biennial oscillation in the stratosphere over earth's equator

(Baldwin et al., 2001; Couston et al., 2018).

They are also created at every convective boundary inside a star. One characteristic of a stellar stratification is that there exists a maximum in N^2 , creating a cavity between the surface and the core to trap IGWs (Tassoul, 1980; Smeyers & van Hoolst, 2010). Since IGWs get reflected once their frequency matches the Brunt-Väisälä frequency, standing g-modes can be excited inside those cavities. Thus g-modes can be observed as brightness oscillations at the surface of stars. An asteroseismic analysis of these oscillations allows one to probe the deep interiors of stars, where the g-modes propagate.

Pedersen et al. (2018) showed that a careful analysis of the observed spectra allows to distinguish between different mixing profiles around convective boundaries proposed in the literature (see 2.2). However, the observational data is not good enough yet to give a fully conclusive answer.

IGWs are also the only diffusive mixing process described in 2.2, which gives them the power to produce a continuous entrainment across convective boundaries if the diffusion constant is large enough. While this has not been confirmed so far, Rogers & McElwaine (2017) proposed that diffusive mixing due to IGWs is able to transport heavier elements from the deep interior to the surface of stars. Baraffe et al. (2017) also relate the lithium depletion in F stars to such an additional diffusive mixing component.

So far, only linear IGWs have been considered, but non-linear effects are expected to play a major role in stellar evolution, because the amplitude of IGWs scales as $\propto \rho^{-1/2}$. In a $3.5M_{\odot}$ star this implies that the amplitude of a wave generated at the boundary of the convective core increases by 5 orders of magnitude until it reaches the photosphere. This is somewhat counteracted by damping of the wave due to radiative diffusion, but it is very likely that some waves cannot be treated in a linear fashion throughout the star (Ratnasingam et al., 2019).

If the amplitude gets too large, IGWs break and deposit their energy and angular momentum into the surrounding medium. Fuller et al. (2015) therefore propose that IGWs, produced in convective burning shells, can spin up stellar cores. This would reduce the tension introduced by observations of the ratio of core to envelope rotation rates in red giants that does not fit the predictions by stellar evolution (see, e.g., Cantiello et al., 2014).

Breaking IGWs might also be responsible for strong outburst in pre-supernova models (Fuller, 2017), which would strip the star from its remaining hydrogen envelope and create a possible candidate for a type Ib supernova.

2.4 Entrainment

Atmospheric and oceanographic sciences have a different approach towards the overshooting problem. They found that convective motions transport mass at a constant rate over a convective to stable interface. The entrained mass is then quickly distributed over the CZ. A composition or density interface at the convective boundary is therefore shifted outwards, which can be interpreted as a continuously growing CZ.

Tracking the position of the composition interface r_i , one can define an entrainment rate $u_{er} = dr_i/dt = \text{const.}$ (see e.g., Turner, 1986).

Dimensional arguments and experiments (see, e.g., Deardorff et al., 1969; Turner, 1986; Hannoun et al., 1988) suggest that the entrainment rate depends on the stiffness of the boundary, i.e., on how stable the stable layer is compared to the convective one. A measure for that is the bulk Richardson number Ri_b , which compares the difference in buoyancy across the interface Δb with the typical size L and speed v_{rms} of the convective motions

$$Ri_b = \frac{\Delta b L}{v_{\text{rms}}^2}. \quad (2.16)$$

The buoyancy jump Δb is defined as an integral of the Brunt-Väisälä frequency N over the width of the interface d_i

$$\Delta b = \int_{r_i - d_i}^{r_i + d_i} N^2 dr. \quad (2.17)$$

As Arthur et al. (2017) point out Ri_b can also be interpreted as the effect of stratification on the smallest turbulent motions down to the Kolmogorov scale.

The mixing speed is generally found to depend on Ri_b as a power law. Following, e.g., Turner (1986) the dimensionless entrainment coefficient E can then be defined as

$$E = \frac{u_{er}}{v_{\text{rms}}} = A Ri_b^{-n} \quad (2.18)$$

where A and n are parameters that need to be calibrated. Typical values for n range from ≈ 1 to ≈ 1.75 (see, e.g., Linden, 1975; Fernando & Long, 1983; Fernando et al., 1989). In geophysical studies the normalization constant A is generally found to be in the order of 0.1 (Stevens & Bretherton, 1999).

Recently agreement with such an entrainment law has also been found in the stellar hydrodynamical context. Meakin & Arnett (2007) were able to extract an entrainment law for a oxygen burning shell, as well as in a model of a $25M_{\odot}$ main

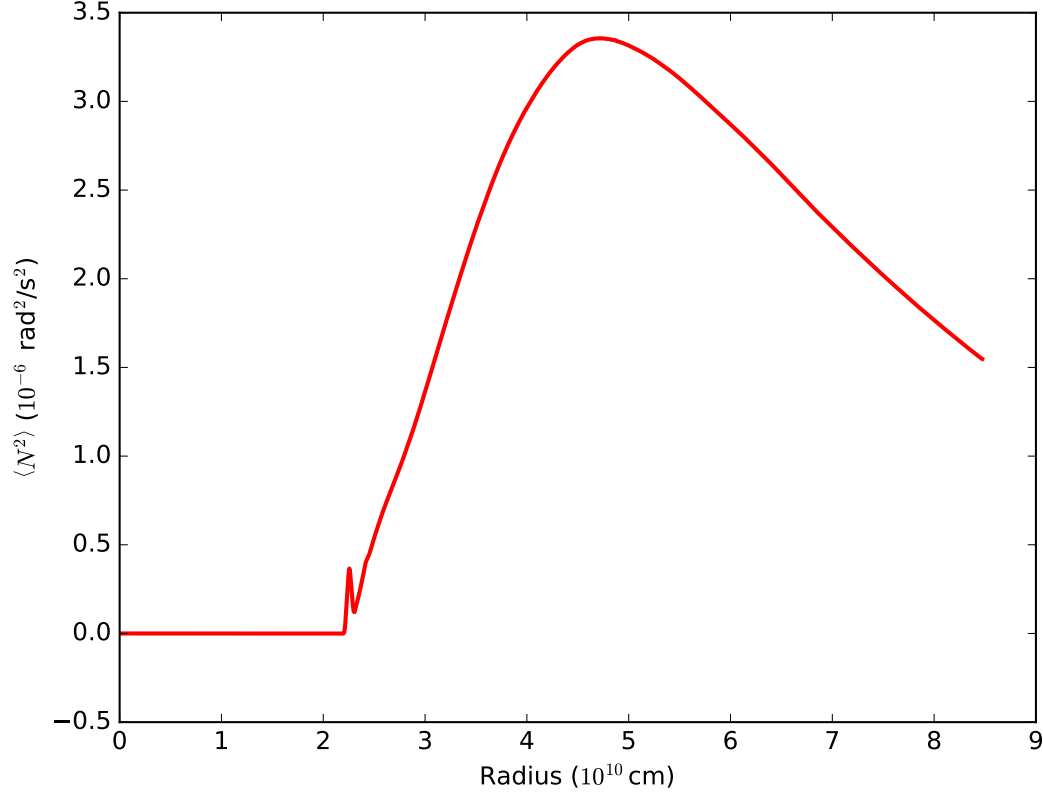


Figure 2.2: Spherically averaged N^2 profile of a $3.5 M_{\odot}$ star taken from the ImHrk simulation.

sequence star. They inferred $A = 0.027 \pm 0.38$ and $n = 1.05 \pm 0.21$ in agreement with geophysical studies. Similar results were found by Cristini et al. (2017) for the case of a carbon burning shell, as well as in Gilet et al. (2013) for a $15 M_{\odot}$ main sequence star.

The inferred entrainment rates, however, are enormous, considering the long evolutionary timescale of stars, e.g., the simulations by Gilet et al. (2013) found that the CZ entrains matter at a rate of $\approx 3.5 \cdot 10^{22}$ g/s. Over the typical main sequence life time of a $15 M_{\odot}$ mass star of roughly 10 Myr the convective core would then grow by almost $6000 M_{\odot}$. The convective core would therefore quickly consume the whole star and evolve homogeneously afterwards. Such a behaviour is, however, not observed. This result makes it clear that entrainment needs to stop eventually when long timescales are involved.

In general, N^2 increases with increasing distance to the CZ (a typical stellar

profile can be seen in Fig. 2.2). An entrainment process that shifts the convective boundary outwards without altering the remaining stellar structure would therefore continuously increase the stiffness of the boundary. One could imagine that the entrainment rate therefore rapidly drops to a negligible value.

In the setups considered in this study a typical convective boundary interface has a width that corresponds to 1/100th of the star’s radius. N^2 close to the convective boundary is approximately 1/10th of the maximum N^2 . Thus we can estimate a maximal Δb . In the worst case scenario where $N^2 = N_{\text{max}}^2$ throughout the star and the integration length corresponds to the stellar radius one finds that Δb cannot be larger than 1000 times the initial Δb . Using $n = 1$ as found by Meakin & Arnett (2007) and assuming that the convective velocity and L stay constant during the entrainment process, one finds that the entrainment rate can, at most, drop by a factor of 1000 regardless of how far the convective boundary has moved.

Using the Gilet et al. (2013) results this still corresponds to an entrainment of $6M_{\odot}$ over the main sequence lifetime. Even this lower limit of entrainment is still unrealistically large, which means that the increasing boundary stiffness cannot be the only process that stops entrainment.

Looking back at the different mixing processes at convective boundaries described in 2.2 it can be expected that all processes except for IGWs will only mix matter up to a certain distance from the Schwarzschild boundary. The size of the mixed zone is therefore set by the farthest mixing process. In order to extend the mixed zone, the Schwarzschild boundary itself needs to migrate. Hence a continuously growing mixed zone given by the entrainment law needs to entrain entropy at the same time. The energy required to entrain entropy has to be provided from convection. However, one would expect that the amount of convective energy decreases with the distance to the convective boundary, as radiation begins to dominate the energy transport.

The energy argument can also be expanded to the chemical mixing, where mixing of buoyant matter into the CZ requires energy to overcome the counteracting buoyancy force.

Indeed, Linden (1975) showed that the entrainment rate depends on how much kinetic energy is available to overcome buoyancy at the interface. He argued that this requires $n \approx 1$, but also showed that the available kinetic energy is not necessarily the energy that has been put into the system, since dissipation and radiative diffusion transform and transport a fraction of the available energy as well. The energy carried away by IGWs is also lost for the entrainment.

Similarly Jones et al. (2017) and Andrassy et al. (2018) were able to show that the entrainment rate scales with the luminosity input into the convective zone in stellar environments as well.

It is important to not that all these studies either neglected radiative energy transport

or were not able to cover thermal timescales in their simulation. This, however, is necessary in order to establish an energy balance.

Considering the effects of radiative energy transport one would expect that entrainment stops as soon as a balance between the entrainment of entropy and buoyant matter, and the radiative energy transport that tries to restore the entropy gradient has been found. This happens on a thermal timescale, which is usually orders of magnitude longer than the convective timescale that we can simulate (see 3.2).

Therefore one can argue that entrainment is limiting the speed of overshooting, but provides very little information about the actual extent of the mixed region on timescales longer than the thermal timescale. Spruit (2015) used a similar argument in order to get an upper limit for the overshooting of a convective helium burning core.

If the evolutionary timescale, however, becomes comparable with the entrainment timescale it needs to be considered as well.

Chapter 3

Low Mach Number Hydrodynamics

Convection in stellar interiors is predicted to be extremely subsonic. The treatment of such low Mach number flows in hydrodynamic simulations requires special techniques in order to do long term simulations that cover a significant amount of convective turnover times. Such simulations also react considerably sensitive to changes in the initial setup.

In this chapter we will introduce the necessary tools and methods in order to perform simulations in the low Mach number regime and to set up a proper initial state based on 1D stellar evolution models.

3.1 Euler Equations

In 2.1 it was established that the typical size of a convective blob has the size of a pressure scale height. This is much larger than the mean free path of a single gas particle inside of stars. It is therefore safe to assume that the gas behaves as a continuum and that individual particle motions can be neglected.

Furthermore, stellar interiors only have a tiny viscosity, e.g., the timescale for viscosity to influence the velocity distribution inside the Sun is of the order of 10^{22} s, much longer than the age of the Universe. It is therefore safe to assume that viscosity can be neglected in simulations of stars. In fact, the numerical viscosity of a grid based hydrodynamical scheme is always orders of magnitudes larger than the actual viscosity of stellar interiors. Therefore, it is not necessary to include an explicit viscosity into the code. This allows the usage of the Euler equations in stellar interiors to simulate motions inside of stars.

The Euler equations can be written as the conservation of mass, momentum, and

energy in the following form

$$\frac{\partial \rho}{\partial t} + \nabla \rho \mathbf{U} = 0 \quad (3.1)$$

$$\frac{\partial \rho \mathbf{U}}{\partial t} + \nabla (\rho \mathbf{U} \cdot \mathbf{U}) + \nabla p = -\rho g \mathbf{e}_r \quad (3.2)$$

$$\frac{\partial \rho E}{\partial t} + \nabla (\rho \mathbf{U} E + p \mathbf{U}) = \nabla (\kappa \nabla T) - \rho g (\mathbf{U} \cdot \mathbf{e}_r) - \sum_k \rho q_k \dot{\omega}_k + \rho H_{\text{ext}}, \quad (3.3)$$

here ρ , t , \mathbf{U} , and p are density, time, velocity, and pressure respectively. g stands for the gravitational acceleration and \mathbf{e}_r is the unit vector in radial direction. $E = \mathbf{U} \cdot \mathbf{U}/2 + E_{\text{int}}$ is the specific total energy, where E_{int} is the internal energy of the gas with opacity κ at temperature T . For each species k we include the abundance changes $\dot{\omega}_k$ with the respective heating rate q_k . H_{ext} stands for an external heating source.

The right hand side of 3.1 is equal to 0 indicating that no mass is added or lost.

The momentum equation 3.2 has a simple source term on the right hand side due to the gravitational acceleration in direction \mathbf{e}_r .

Equation 3.3 describes the evolution of E and contains contributions from all different physical effects considered in our simulations. The first term on the right hand side gives the energy transport due to radiation depending on T and κ in the diffusive approximation. The diffusive approximation is only valid in an optically thick regime. In stellar interiors this is always fulfilled.

The second term covers the potential energy due to gravity and the last two terms introduce heating sources due to reactive heating of each species k and due to external sources H_{ext} .

3.1.1 Microphysics

The Euler equations as given in 3.1 – 3.3 need to be supplemented by a set of microphysics modules. This includes a way to obtain realistic opacities, a nuclear reaction network to follow q_k and abundance changes $\dot{\omega}_k$ of each species k , as well as an equation of state (EOS), providing a relation between ρ , p , and T .

The MAESTRO simulations produced for this study use the Helmholtz EOS (Timmes & Swesty, 2000). This EOS includes effects of radiation, ionization, degeneracy of electrons and Coulomb corrections in a semi analytical tabulated form. In order to obtain thermodynamically consistent results while interpolating in the EOS table, all thermodynamic quantities are computed as derivatives of the Helmholtz free energy, hence the name of the EOS.

The Helmholtz EOS as provided by Timmes & Swesty (2000) includes routines to

compute the pressure and all other thermodynamic quantities for a given density ρ , temperature T , mean atomic weight \bar{A} and mean charge \bar{Z} . In 3.4 it will become clear that it is sometimes necessary to call the EOS with different input quantities. When, e.g., the enthalpy h has been updated, creating a thermodynamically consistent state requires to call the EOS with h as an input quantity instead of ρ or T . The Helmholtz EOS has no interface for this, but it is possible to create one based on the provided routines. First one checks whether the old values of ρ and T still reproduce the updated h . In case this does not match, the EOS provides all thermodynamic derivatives necessary to construct a Newton-Raphson iterator that will find a pair ρ , T that corresponds to the updated h . The accuracy of this iterator is usually set to 10^{-13} .

The simulations follow three species. ^1H , ^4He and a CNO element, the latter representing a combination of all elements involved in the CNO cycle of hydrogen burning. The atomic weight and charge of the CNO element is defined as 14.87 and 7.43 respectively. These values are based on the atomic weight and charge of C, N, and O and their respective abundance ratios in the solar composition.

Hydrogen burning is a slow process lasting millions to billions of years, while the longest simulation in Chap. 4 extends for only ≈ 6 years. During that time only a negligible fraction of hydrogen would be burned. It was therefore decided not to follow the abundance changes due to reactive burning. $\dot{\omega}_k$ in 3.3 is then set equal to zero, which makes the simulations computationally cheaper since no network calculations need to be done.

Nevertheless it is necessary to include the energy release of the nuclear burning into the simulations in order to drive convective motions. The nuclear heating term is based on hydrogen burning equilibrium rates for the pp (H_{pp}) and the CNO (H_{cno}) cycle, according to Kippenhahn et al. (2012).

$$H_{pp} = 2.57 \cdot 10^4 \psi f g_{pp} \rho X^2 T_9^{-2/3} \exp\left(-3.381/T_9^{1/3}\right) \quad (3.4)$$

$$g_{pp} = 1 + 3.82T_9 + 1.51T_9^2 + 0.144T_9^3 - 0.0114T_9^4 \quad (3.5)$$

$$H_{cno} = 8.24 \cdot 10^{25} g_{cno} \rho X_{CNO} X T_9^{-2/3} \exp\left(-15.231T_9^{-1/3} - (T_9/0.8)^2\right) \quad (3.6)$$

$$g_{cno} = 1 - 2.00T_9 + 3.41T_9^2 - 2.43T_9^3, \quad (3.7)$$

where X and X_{CNO} are the abundances of hydrogen and the CNO element respectively and T_9 is the temperature in units of 10^9 K. f and ψ in 3.4 are the shielding factor and a correction factor for energy branches in different branches of the pp-cycle respectively. f accounts for the shielding of the potential of hydrogen atoms by nearby electrons which increases the probability of a reaction between two ^1H atoms slightly. The influence of electron shielding decreases with increasing temperature, i.e., $f \gtrsim 1$. ψ ranges from 1 to 2 and effectively describes how many of

the slow ${}^1\text{H} + {}^1\text{H}$ reactions are needed to create one ${}^4\text{He}$. f and ψ are set equal to one for all simulations in this study. Overall the energy production of the pp-chain is underestimated, but for the models in this study the CNO cycle produces $> 97\%$ of the energy input anyway.

The nuclear heating computed from 3.4 and 3.6 is formally included as an external heating source in the simulations. It therefore corresponds to the last term in 3.3.

The opacities necessary for the diffusive energy transport by radiation are taken from the analytic stellar opacities provided by Timmes (2000). This is a combination of the analytic expressions for hydrogen-free and hydrogen-containing compositions by Iben (1975) and Christy (1966) respectively. It also contains contributions from Compton-scattering based on Weaver et al. (1978).

3.1.2 Spatial Discretisation

The Euler equations are continuous functions in space and time. In order to solve the system of equations on a computer they need to be discretised. In this work we use the finite volume method, where equations 3.1 – 3.3 are discretised on a regular Cartesian grid. Each cell of the three dimensional grid can be associated with a coordinate of the form $x_{i,j,k}$. The conserved quantities of the system are saved for each cell. In the finite volume method the saved values represent integrated values over the whole cell, normalized by the cell volume. The quantity f_i can then be written as

$$f_i = \frac{1}{\Delta x \Delta y \Delta z} \int_{x_{i-1/2,j,k}}^{x_{i+1/2,j,k}} \int_{x_{i,j-1/2,k}}^{x_{i,j+1/2,k}} \int_{x_{i,j,k-1/2}}^{x_{i,j,k+1/2}} f(x, y, z) dx dy dz \quad (3.8)$$

where $\Delta x = x_{i+1/2,j,k} - x_{i-1/2,j,k}$, $\Delta y = x_{i,j+1/2,k} - x_{i,j-1/2,k}$, and $\Delta z = x_{i,j,k+1/2} - x_{i,j,k-1/2}$ are the width of the cell in each dimension.

To second order the averaged value is equivalent to an evaluation at the cell center.

The advantage of finite volume schemes is that they are conservative by construction, i.e., that the quantities conserved by the Euler equations (mass, momentum, energy) will be conserved down to machine precision level on the grid level. This is possible, because the value associated with each cell can only change due to fluxes through the cell surfaces.

Computing these fluxes at cell interfaces $x_{i+1/2,j,k}$ etc., however, is not trivial, because it requires knowledge about the value of the conserved quantities at these interfaces. The easiest way to get the interface values is to assume that $f(x_{i-1/2,j,k}) = f(x_{i,j,k}) = f(x_{i+1/2,j,k})$. This also means that $f(x_{i+1/2,j,k}) = f(x_{i+1,j,k}) = f(x_{i+3/2,j,k})$, which

is a problem because now there are two independent values for $f(x_{i+1/2,j,k})$. These values which will be called f_L and f_R in the following, as one is constructed approaching the cell interface from "the left" and one from "the right". In general, f_L and f_R do not agree with each other, which can be interpreted as a discontinuity in the function $f(x)$. This defines a Riemann problem at each interface, which needs to be solved in order to get a consistent scheme.

The Riemann problem is one of the few problems in hydrodynamics that has an analytic solution. However, such Riemann solvers require Newton-Raphson iterations (see, e.g., Toro, 2013). Most hydrodynamical codes therefore use simplified approximate solvers.

One possible approximate Riemann solver for the Euler equations can be constructed in a two step process. First the velocities on the interface $U_{i+1/2}^{\text{MAC}}$ are reconstructed, where the following approximate Riemann solver is used

$$U_{i+1/2}^{\text{MAC}} = \begin{cases} 0, & (U_L^{\text{MAC}} \leq 0 \text{ AND } U_R^{\text{MAC}} \geq 0) \text{ OR } |U_L^{\text{MAC}} + U_R^{\text{MAC}}| < \epsilon \\ U_L^{\text{MAC}}, & U_L^{\text{MAC}} + U_R^{\text{MAC}} > 0 \\ U_R^{\text{MAC}}, & U_L^{\text{MAC}} + U_R^{\text{MAC}} < 0. \end{cases} \quad (3.9)$$

All other quantities $f(x_{i+1/2,j,k})$ are obtained from the solution $U_{i+1/2}^{\text{MAC}}$

$$f(x_{i+1/2,j,k}) = \begin{cases} 0.5 \cdot (f_L + f_R), & |U_{i+1/2}^{\text{MAC}}| > \epsilon \\ f_L, & U_{i+1/2}^{\text{MAC}} > 0 \\ f_R, & U_{i+1/2}^{\text{MAC}} < 0 \end{cases} \quad (3.10)$$

The order of accuracy of a spatial discretisation depends on how accurately one can reconstruct the interface states f_L and f_R . A commonly used reconstruction is the so-called piecewise parabolic method (PPM) (Colella & Woodward, 1984), which fits the cell centred data with a parabolic profile and reconstructs the interface value based on that. Constructing a parabola requires the use of the two neighbouring cells in each direction, which makes it necessary to include some ghost cells at the edge of the computational domain. Reconstruction via PPM leads to a scheme that is second order accurate in space.

3.1.3 Temporal Discretisation

Hydrodynamical simulations require that equations 3.1 – 3.3 are integrated in time. Numerically this needs to be done in a discrete way, whereby the integration is split up into timesteps $t^{n+1} = t^n + \Delta t$. The time increment Δt has to be chosen such that all physical processes are resolved and that the system is stable.

Considering a differential equation of the form

$$\frac{df(t)}{dt} = F(t, f(t)), \quad (3.11)$$

one can easily approximate the left hand side as a difference quotient

$$\frac{df(t)}{dt} = \frac{f^{n+1} - f^n}{\Delta t}, \quad (3.12)$$

where $f^n = f(t)$ and $f^{n+1} = f(t + \Delta t)$.

Combining equations 3.11 and 3.12 it is trivial to solve for the updated f^{n+1}

$$f^{n+1} = f^n + \Delta t F(t^n, f^n), \quad (3.13)$$

This is the so-called explicit (or forward) Euler method. It approximates the integration solely based on data from the previous timestep and converges with second order accuracy.

A linear stability analysis shows that such a scheme is only stable if it resolves the fastest propagation of physical information on the grid associated with a propagation speed c_{signal} . Over a distance Δx , Δt is then restricted by the Courant-Friedrichs-Lewy (CFL) condition (Courant et al., 1928)

$$\Delta t \leq \text{CFL} \frac{\Delta x}{c_{\text{signal}}}, \quad (3.14)$$

where CFL is a scaling factor < 1 . which, depending on code and personal preference, is usually taken between 0.3 and 0.9.

In most hydrodynamical simulations the dominating signal speed is a combination of soundspeed c_s and flow velocity $u = |\mathbf{U}|$

$$\Delta t \leq \text{CFL} \frac{\Delta x}{c_s + u}. \quad (3.15)$$

Another way to obtain a second order time discretisation is to compute f^{n+1} based on f^n and f^{n+1} . The resulting discretisation is then called implicit (or backward) Euler method

$$f^{n+1} = f^n + \Delta t \cdot F(t^n, f^{n+1}). \quad (3.16)$$

It can be shown that such an implicit method is not limited in the size of the timestep any more. However, these methods are computationally expensive, since they require in every timestep an inversion of a matrix in order to solve the linear system. Depending on the problem size this is a very expensive computation, not

only in terms of computing time, but also in terms of memory consumption.

It is also possible to combine explicit and implicit methods. A predictor-corrector integrator (also known as Heun's method) increases the accuracy of the explicit Euler method, by combining it with the trapezoidal rule of integration. First one evaluates the function F and performs an explicit Euler step (predictor) to obtain an intermediate state $f^{n+1,*}$. Then $f^{n+1,*}$ is used to evaluate the function again. Combining the new evaluation of F with the initial one with the trapezoidal rule (corrector) then gives a second order accurate estimate of f^{n+1} . The scheme can be written as

$$f^{n+1,*} = f^n + \Delta t F(t^n, f^n) \quad (3.17)$$

$$f^{n+1} = f^n + \frac{\Delta t}{2} (F(t^n, f^n) + F(t^{n+1}, f^{n+1,*})) \quad (3.18)$$

Higher order methods using even more steps can improve the accuracy and order of the time integration. One family of multi step integrators are the Runge-Kutta integrators (Runge, 1895; Kutta, 1901). The most famous one is the RK4 method, which advances the simulation with 4 intermediate evaluations of F . Each evaluation is depending on the previous one. The final update is then constructed from the intermediate states as

$$f^{n+1} = f^n + \frac{1}{6}k_1 + \frac{1}{3}k_2 + \frac{1}{3}k_3 + \frac{1}{6}k_4 \quad (3.19)$$

$$k_1 = \Delta t F(t_n, f(t_n))$$

$$k_2 = \Delta t F\left(t_n + \frac{\Delta t}{2}, f(t_n) + \frac{k_1}{2}\right)$$

$$k_3 = \Delta t F\left(t_n + \frac{\Delta t}{2}, f(t_n) + \frac{k_2}{2}\right)$$

$$k_4 = \Delta t F(t_n + \Delta t, f(t_n) + k_3).$$

The RK4 method is a 4th order accurate method. While the timesteps of Runge-Kutta methods are still restricted by 3.15, the higher accuracy can help to smooth out numerical problems. This effect can be seen in 3.5.3 and will be discussed in more detail in 4.3.

3.2 Timescales

The problem of stellar evolution is a problem of timescales. The nuclear timescale dictates lifetime and evolutionary speed of a star and can be estimated from the amount of available nuclear fuel and the stars luminosity L as

$$\tau_{\text{nuc}} = \frac{E_{\text{nuc}}}{L} \quad (3.20)$$

For a $3.5M_{\odot}$ mass star this gives a main sequence lifetime of the order of 100 Myr. In 2.1 it was discussed that the energy transport in convectively unstable regions in stars is mainly due to convective motions. The convective turnover time τ_{conv} is therefore an estimate of the timescale on which energy transport occurs. It can be defined as the time a convective element with a typical velocity v_{rms} takes to cross a CZ of thickness r_{CZ} and to return to its original position

$$\tau_{\text{conv}} = \frac{2r_{\text{CZ}}}{v_{\text{rms}}}. \quad (3.21)$$

In a $3.5M_{\odot}$ mass star MLT predicts convective turnover times of a few months in its core.

The 8–9 orders of magnitude difference between τ_{conv} and τ_{nuc} shows that it is currently computationally impossible to follow the complete evolution of a star while also resolving convective motions.

The problem gets even worse, when one wants to do hydrodynamical simulations, where the timestep is restricted by the soundspeed c_s (see 3.15). This can also be associated to a soundcrossing timescale

$$\tau_{\text{sound}} = \frac{r_{\text{CZ}}}{c_s}. \quad (3.22)$$

According to MLT, the expected convective motions in stellar interiors have Mach numbers of the order of 10^{-4} in early burning stages and up to 10^{-2} in later burning stages. This means that a τ_{sound} resolving simulation of a convective hydrogen burning zone that is resolved by 100 grid cells needs $\approx 10^6$ timesteps to cover a convective turnover time. Therefore it is computationally not feasible to simulate stellar interiors over a large number of convective turnovers.

However, Arnett et al. (2009) showed that it is necessary to compute several convective turnover times while convection is fully developed in order to make reliable predictions about the mixing at a convective boundary. Even worse, establishing a convective state might already take a few turnover timescales. The long timescales of stellar evolution also result in the fact, that even very small effects in terms of mixing can have a huge impact on the stellar structure itself (Andrássy & Spruit, 2015). In order to study small effects long running simulations are needed.

Implicit methods can overcome this timestepping problem since they are not restricted by the CFL condition (see 3.1.3). It is, however, computationally more efficient to modify the Euler equations such that sound waves can be ignored. These soundproof methods are introduced in 3.3 and allow one to perform the desired simulations over several turnover timescales.

One can define many different timescales between τ_{sound} and τ_{nuc} . Two noticeable ones are the Kelvin–Helmholtz timescale τ_{KH} and the buoyancy timescale τ_{brunt} .

τ_{KH} is defined as the ratio of available potential energy to the luminosity of a star (see, e.g., Kippenhahn et al., 2012)

$$\tau_{\text{KH}} = \frac{E_{\text{grav}}}{L} \approx \frac{3GM^2}{RL}. \quad (3.23)$$

where M and R are the mass and the radius of the star, respectively. τ_{KH} describes the timescale on which a star evolves if nuclear burning suddenly stops. It can also be interpreted as the stars reaction time to changes in its internal energy budget. This becomes important when the effects of penetration (see 2.2) on the stellar structure are analysed. For the Sun one finds $\tau_{\text{KH}} \approx 10^7$ yr, i.e., $\tau_{\text{KH}} \gg \tau_{\text{conv}}$ which currently prevents thermally relaxed simulations in this regime.

One can also define a timescale for IGWs. A mass element that is displaced in a stable stratification will start to oscillate due to buoyancy with frequency N (see 2.3). One possible way to define τ_{brunt} is to use the period of this oscillation

$$\tau_{\text{brunt}} = \frac{1}{N}. \quad (3.24)$$

In stellar interiors one often finds $\tau_{\text{conv}} > \tau_{\text{brunt}} > \tau_{\text{sound}}$, which makes it difficult to properly resolve IGWs with soundproof methods (see 4.3).

3.3 Sound-proof Methods

Even though the implicit methods discussed in section 3.1.3 are not restricted in their timestep size, they are rarely used to avoid the problem of timescales, as they are very expensive and tend to have convergence problems if too large timesteps are used. It is also challenging to set up a scheme that provides the correct flows in a low Mach number regime (Miczek et al., 2015).

The so-called sound proof methods avoid the problem of resolving τ_{sound} by decoupling pressure and density in the Euler equations. This effectively prohibits sound waves from developing, i.e., they do not have to be considered in the timestep constraint of explicit methods any longer. The new CFL condition is then

$$\Delta t \leq CFL \frac{\Delta x}{u}, \quad (3.25)$$

which leads to a potential speed-up of 10^4 in the case of core hydrogen burning.

In order to remove sound waves from the Euler equations, one needs to decouple the pressure and density in the momentum equation 3.2. The simplest way to do this is the so-called Boussinesq approximation (Boussinesq, 1903), where one assumes that density is kept constant during the simulation. With a constant density

there obviously can be no coupling between pressure and density and sound waves disappear. In the Euler equations one can then ignore all time derivatives with respect to ρ . The mass conservation equation 3.1 is then reduced to

$$\nabla \mathbf{U} = 0 \quad (3.26)$$

Codes that uses the Boussinesq approximation always need to fulfil this constraint for their velocity fields. This is a good approximation for very low Mach number flows, but ignores all effects due to compression of matter. It is therefore also called incompressible hydrodynamics.

In order to gain some of the compressibility back, while still removing the sound waves, one can write 3.2 in a dimensionless form. Dimensionless quantities are defined as $\tilde{x} = \frac{x}{x_{\text{ref}}}$, where x_{ref} is a characteristic value of that quantity. 3.2 can then be written as

$$\frac{\partial \tilde{\rho} \tilde{\mathbf{U}}}{\partial t} + \nabla(\tilde{\rho} \tilde{\mathbf{U}} \cdot \tilde{\mathbf{U}}) + \frac{1}{\text{Ma}^2} \nabla(\tilde{p} - \tilde{p}_0) = \frac{1}{\text{Ma}^2} \frac{L_{\text{ref}}}{H_{\text{ref}}} (\tilde{\rho} - \tilde{\rho}_0) g \mathbf{e}_r \quad (3.27)$$

where a horizontally averaged background pressure $\tilde{p}_0 = \langle \tilde{p} \rangle$ and density $\tilde{\rho}_0 = \langle \tilde{\rho} \rangle$ are introduced. Ma , L_{ref} , and H_{ref} are a characteristic Mach number, length and scale height, respectively.

Assuming that $L_{\text{ref}} = H_{\text{ref}}$ implies that the density perturbations $(\tilde{\rho} - \tilde{\rho}_0)$ as well as pressure perturbations $(\tilde{p} - \tilde{p}_0)$ are of the order Ma^2 . In this so-called anelastic approximation it is therefore only possible to track small perturbations in density. In fact, it turns out that all thermodynamic quantities can be treated as small perturbations on top of a constant background state. Similar to the Boussinesq approximation a restriction on the divergence of the velocity field can be defined as

$$\nabla \rho \mathbf{U} = 0. \quad (3.28)$$

To allow for even more compressibility one needs to adjust the characteristic length scales according to the problem. Following the pseudo incompressible approximation by Durran (1989) one can relate the typical timescale of the flow t_{ref} to the buoyancy force $t_{\text{ref}} = \frac{L_{\text{ref}}}{U_{\text{ref}}} = \frac{U_{\text{ref}}}{g}$. This implies a typical lengthscale of $L_{\text{ref}} = \frac{U_{\text{ref}} \cdot U_{\text{ref}}}{g}$. In addition to that one can assume that in a low Mach number flow, the pressure is quickly equilibrated by sound waves. It is therefore possible to set the typical pressure as $p_{\text{ref}} = \rho_{\text{ref}} c_{s,\text{ref}}^2$. This gives a typical pressure scale height $H_{\text{ref}} = \frac{p_{\text{ref}}}{\rho_{\text{ref}} g} = \frac{c_{s,\text{ref}}^2}{g}$. On the right hand side of equation 3.27 one can then see that this choice of scales leads to $\frac{1}{\text{Ma}^2} \frac{L_{\text{ref}}}{H_{\text{ref}}} = 1$. Thus in order to fulfil equation 3.27, pressure fluctuations $\pi = p - p_0$ have to scale with $\pi \approx \text{Ma}^2$ in the low Mach number limit. It is therefore reasonable to ignore these small fluctuations in all equations except in the momentum

equation. This is the assumption that will decouple pressure and density in this set of equations.

In contrast to the anelastic approximation there now is no restriction on the density perturbations any longer, which in theory allows to also simulate expanding/contracting systems that build up density variations of finite amplitude over time as long as the pressure perturbations stay small.

In order to get a constraint on the velocities analogous to the one in the previous methods, one needs to linearise the EOS and incorporate it into the system of equations.

Following Almgren et al. (2006a) an EOS of the form $p = p(\rho, T, X_k)$ can be linearised as

$$\frac{D\rho}{Dt} = \frac{1}{p_\rho} \left(\frac{Dp}{Dt} - p_T \frac{DT}{Dt} - \sum_k p_{X_k} \dot{\omega}_k \right), \quad (3.29)$$

where $D/Dt = \partial_t + \mathbf{U} \cdot \nabla$ and $p_\rho = \partial p / \partial \rho|_{X_k, T}$, $p_T = \partial p / \partial T|_{X_k, \rho}$, and $p_{X_k} = \partial p / \partial X_k|_{T, \rho}$.

In order to obtain DT/Dt one can rewrite Eq. 3.3 in terms of the specific enthalpy $h = e + p/\rho$, where $e = E - \mathbf{U}\mathbf{U}/2$ is the specific internal energy of the fluid

$$\rho \frac{Dh}{Dt} - \frac{Dp}{Dt} = \nabla(\kappa \nabla T) - \sum_k \rho q_k \dot{\omega}_k + \rho H_{\text{ext}} := \rho H. \quad (3.30)$$

Similar to 3.29 one can now also differentiate Dh/Dt

$$\rho \frac{Dh}{Dt} = \rho \left(h_T \frac{DT}{Dt} + h_p \frac{Dp}{Dt} + \sum_k h_{X_k} \dot{\omega}_k \right) = \frac{Dp}{Dt} + \rho H, \quad (3.31)$$

where $h_T = \partial h / \partial T|_{p, X_k}$, $h_p = \partial h / \partial p|_{T, X_k}$, and $h_{X_k} = \partial h / \partial X_k|_{p, T}$. DT/Dt is then

$$\frac{DT}{Dt} = \frac{1}{\rho h_T} \left((1 - \rho h_p) \frac{Dp}{Dt} - \sum_k \rho h_{X_k} \dot{\omega}_k + \rho H \right). \quad (3.32)$$

$D\rho/Dt$ can be derived from 3.1 as

$$\frac{D\rho}{Dt} = -\rho \nabla \mathbf{U}. \quad (3.33)$$

According to the scaling assumption made before, it is possible to replace p with p_0 . Dp/Dt then simplifies to $\mathbf{U} \nabla p_0$. With this transformation one gets an initial version of the new constraint on the velocity field by combining equations 3.29, 3.32, 3.33

$$\nabla \mathbf{U} + \alpha \mathbf{U} \nabla p_0 = \frac{1}{\rho p_\rho} \left[\frac{p_T}{\rho h_p} \left(\rho H - \rho \sum_k h_p \dot{\omega}_k \right) + \sum_k p_{X_k} \dot{\omega}_k \right] := S \quad (3.34)$$

here α is defined as

$$\alpha(\rho, T) = \frac{-(1 - \rho h_p)p_T - \rho h_p}{\rho^2 h_p p_\rho} = \frac{1}{\Gamma_1 p_0}, \quad (3.35)$$

where Γ_1 is the first adiabatic index of a general EOS. The exact derivation of this last equality can be found in the appendix of Almgren et al. (2006a). Equation 3.34 can be simplified by introducing a function $\beta_0(r)$ that describes the stratification of the background state

$$\beta_0(r) = \beta(0) \exp \left(\int_0^r \frac{\nabla p_0(r')}{\Gamma_1(r') p_0(r')} dr' \right). \quad (3.36)$$

It should be noted that $\nabla p_0(r)$ can be replaced with $-\rho_0(r)g(r)$ if the state is in hydrostatic equilibrium. In that case the normalization $\beta(0)$ can be expressed as the density at the origin $\beta(0) = \rho_0(0)$. The derivation of $\beta_0(r)$ can be found in the appendix of Almgren et al. (2006a).

Using Eq. 3.36, 3.34 can be written as

$$\nabla \beta_0 \mathbf{U} = \beta_0 S \quad (3.37)$$

3.4 MAESTRO

MAESTRO is an open source hydrodynamics code and was introduced in a series of papers Almgren et al. (2006a,b, 2008); Nonaka et al. (2010). It uses a generalized version of the pseudo incompressible approximation (Durrant, 1989) to remove sound waves from the simulations. As discussed in 3.3 this has the advantage that it does support the evolution of large scale density and temperature perturbations and only pressure fluctuations need to be assumed to be small.

MAESTRO solves the following system of equations combining equations 3.27, 3.37, 3.3, and 3.1,

$$\frac{\partial \rho}{\partial t} + \nabla \rho \mathbf{U} = 0 \quad (3.38)$$

$$\rho \frac{\partial(\mathbf{U})}{\partial t} + \rho \mathbf{U} \nabla \mathbf{U} = \frac{\beta_0}{\rho} \nabla \frac{\pi}{\beta_0} - \frac{(\rho - \rho_0)}{\rho} g \mathbf{e}_r \quad (3.39)$$

$$\rho \frac{Dh}{Dt} - \frac{Dp}{Dt} = \nabla(\kappa \nabla T) - \sum_k \rho q_k \omega_k + \rho H_{ext} \quad (3.40)$$

$$\nabla \beta_0 \mathbf{U} = \beta_0 S, \quad (3.41)$$

where the scaling assumptions of the pseudo incompressible approximation as discussed in 3.3 have been included in 3.27 in order to obtain 3.39 in terms of the

velocity. From first principles the first term on the right hand side of 3.39 should look like $1/\rho \nabla \pi$, but Vasil et al. (2013) has shown that this kind of approach leads to a system that does not conserve the actual energy of the system. Instead a pseudo energy is conserved. To correct for that one needs to modify the equation like it is done in 3.39. This energy fix was proposed in Vasil et al. (2013) and has been included into the MAESTRO code in Jacobs et al. (2016).

MAESTRO computes a single timestep in a fractional step method, where first density, enthalpy, and velocity are advected without taking the velocity constraint 3.37 into account and then the velocity constraint is enforced in a separate step. The advection is using a second order PPM scheme where the Riemann problem is approximately solved according to Eq. 3.9 and Eq.3.10. In time it is discretised as a predictor corrector (PC) scheme as described in 3.17.

After the advection, the state is forced to fulfil equation 3.37, which also sets the updated pressure (see Bell et al., 2002). MAESTRO solves the Poisson equation of the velocity constraint 3.37 by a projection method using the AMRex (formerly boxlib) library (Zhang et al., 2019).

Numerically Eq. 3.37 can be solved exactly. However, in contrast to the Boussinesq and anelastic approximation, Eq. 3.37 is non-homogeneous. Solving Eq. 3.37 exactly therefore leads to a numerically unstable scheme due to decoupling of the stencil (see Lai et al., 1993; Rider et al., 1995).

Almgren et al. (1996) showed that this is not the case if an approximate projection method that only solves the constraint down to some given accuracy is used. The stability and accuracy of an approximate projection depend on the projection operator that is used. The specific form of the projection used in MAESTRO can be found in Almgren et al. (2000).

Overall the scheme is second order accurate in time and space. More details of the scheme, including a flow chart, can be found in Nonaka et al. (2010).

One downside of the fractional step approach is that it makes it impossible to conserve mass and energy while simultaneously fulfilling the EOS at all times. It is therefore one of the design choices of MAESTRO to conserve mass and energy, which means that over time the conserved quantities in combination with the pressure fluctuations π do not reproduce the EOS any longer. While this drift is rather slow and relative changes are negligible, it becomes important when temperature gradients are compared, since those are sensitive to absolute changes (see 4.6).

For this study it was found that the PC time integration scheme causes unrealistically large velocities in stably stratified regions. The velocities are caused by an insufficient time resolution of internal gravity waves and can be overcome by reducing the timesteps significantly (see discussion in 4.3). Doing so, however, prevents

us from doing the longterm simulations we are interested in due to the increased computational cost.

Another way to mitigate this problem is to use a higher-order, multi-step scheme for the time integration. Bell et al. (2002) showed that it is possible to exchange the time advancement before the final projection by any other method. We replaced the PC method with a 4th order Runge-Kutta (RK) integrator as described in 3.1.3. A flow chart of this new method is depicted in Fig. 3.1. In blue we give the updated quantity in each sub step.

During the RK loop we need to introduce two additional velocities in the scheme. U^* is the updated velocity in each RK step, computed using the reconstructed velocity at the cell interfaces U_{MAC} . U_{MAC} is forced to fulfil the velocity constraint of Eq. 3.37, while U^* in general does not do that. The advection of density, composition, and enthalpy uses U_{MAC} to compute the respective flows at the cell interfaces. Due to enforcing the velocity constraint on U_{MAC} in each RK iteration it is no longer guaranteed that U_{MAC} directly corresponds to U^* , i.e., there might be differences between the advection velocity and the velocity at the cell centres. However, the projection of U_{MAC} is necessary to maintain the pseudo incompressible approximation of the scheme.

In each step the temperature is updated using the EOS, i.e., the EOS needs to be called in an iterative way, as described in 3.1.1.

MAESTRO is a purely Cartesian code with an one dimensional background state. In order to compute spherical stars it is therefore necessary to adjust the scheme, such that the background state is evaluated consistently with the domain centred dataset. Nonaka et al. (2010) showed the necessary algorithm to do this in three dimensional simulations. We extended the scheme to analogously allow for 2D simulations of spherical datasets as well. The resulting 2D domain then corresponds to the equatorial plane of a star.

Computing a spherical star on a cubic (quadratic) grid requires special care at the outer boundary of the domain, which is prone to numerical problems and convergence errors. MAESTRO provides different options to reduce these effects. In cases where the radius of the star is smaller than the width of the computational box the corners of the domain are expected to be empty. Numerical fluctuations in the corners can then be reduced by reducing the complexity of the equations, e.g., by ignoring all buoyancy forces. One can also enforce the simpler anelastic velocity constraint from Eq. 3.28 in those areas or even fix the density at a small constant value. In order to reduce the influence of these simplifications on the rest of the computation one has to ensure that they are only applied in regions with very low densities.

In this study, we are dealing with a different situation, because due to the large density contrast in stars it is not possible to fit the entire star in our computational

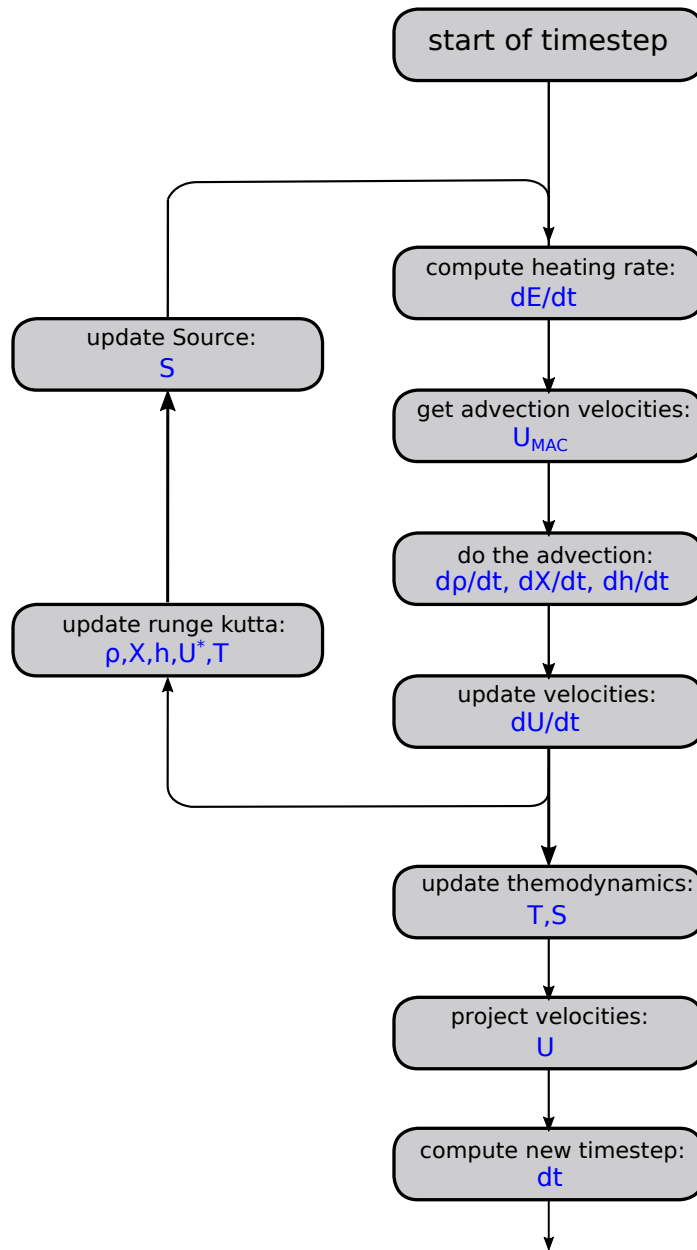


Figure 3.1: Flow chart of the modified time advancement algorithm using a Runge-Kutta integrator. The computed/updated quantities of each sub step are given in blue.

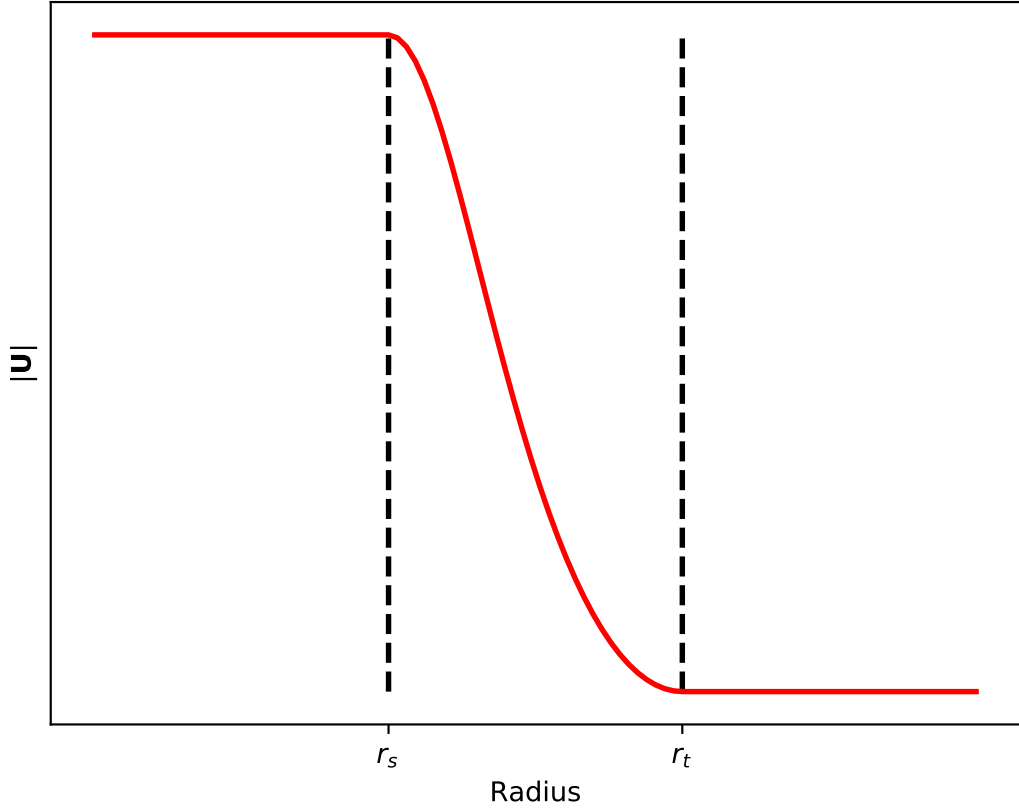


Figure 3.2: Functional form of the damping function $f_{\text{damp}}(r)$ applied on a constant velocity.

box at a reasonable resolution. The corners of the domain can therefore not be considered empty, i.e., we cannot use simplifications of the physics, without introducing new numerical artefacts. However, without special treatment the corners of the domain develop spurious velocities due to mapping and averaging errors (see Gilet, 2012). Almgren et al. (2008) therefore introduced a damping function $f_{\text{damp}}(r)$ into MAESTRO that is used to keep the spurious velocities as small as possible. The functional form depending on the radial distance to the centre of the domain r is

$$f_{\text{damp}}(r) = \begin{cases} 0, & r < r_s \\ \frac{1}{2} \left(1 - \cos \left[\pi \frac{r-r_s}{r_t-r_s} \right] \right), & r_s \leq r < r_t \\ 1, & r \geq r_t, \end{cases} \quad (3.42)$$

where r_s defines the minimum radius where damping is starting and $r_t - r_s$ gives the

distance over which the damping is slowly ramped up.

The strength of the damping is scaled with the size of the timestep and a scaling factor κ

$$\mathbf{U}_{\text{damp}} = \frac{\mathbf{U}}{1 + \Delta t \kappa f_{\text{damp}}}. \quad (3.43)$$

Fig. 3.2 illustrates how a constant velocity would be damped by $f_{\text{damp}}(r)$. The damping is applied before the final projection step. This ensures that the velocity constraint is fulfilled at the end of each timestep.

In MAESTRO gravity is usually computed based on the background state. This is similar to using a monopole solver for gravity, but ensures that gravity is computed in agreement with the spherical geometry.

Cargo & LeRoux (1994) proposed a well-balancing method to keep a stable stratification stable in a numerical setup. Their method computes the pressure that is needed to establish a hydrostatic equilibrium (HSE) and then subtracts it from the actual pressure such that only the perturbations are considered. This is similar to the treatment of pressure in MAESTRO, which makes MAESTRO simulations intrinsically well-balanced.

MAESTRO has a few additional features that are worth mentioning but are not used in this study, since they are either not suited for the performed simulations or computationally too expensive for the specific cases discussed here.

For setups that expand (or contract) significantly during the simulation time, a static background state is not a good approximation. Especially since the background is used to calculate the gravitational acceleration one would expect that an evolving background state gives more reliable results. Almgren et al. (2008) introduced such an evolving background state into MAESTRO, where the background is evolved according to spherically averaged radial velocities. However, it is still required that the background state is in HSE, which needs to be enforced at all times.

To allow simulations over a large range of scale heights, Nonaka et al. (2010) extended the algorithm with an adaptive mesh refinement. This allows to focus the computational resources on one or more specific regions, while the remaining parts of the domain are computed at coarser resolution.

MAESTRO also has a flexible interface for nuclear reaction networks, which makes it easier to switch to arbitrarily large reaction networks. It is also possible to change the type of network integrator easily.

3.5 Code Verification

In this section the low Mach number properties of MAESTRO are tested. The PC integrator has been established and has proven to give reliable results (Jacobs et al., 2016; Gilet et al., 2013). The RK integrator needs to be compared with the PC results in order to see under which circumstances the higher order time integration performs better. For that purpose four test cases of increasing complexity will be analysed.

The Gresho Vortex is a pressure stabilized vortex in 2D without gravity. The "test spherical" setup that comes with the MAESTRO package is a similar setup but in three dimensions. Including gravity one can look at a stable atmosphere, as well as a convective zone surrounded by stable layers. In a stable atmosphere the advantages of the RK scheme will be evident. The latter two tests were performed in 2D in order to reduce computational cost.

3.5.1 Gresho Vortex

Low Mach number flows require that the numerical scheme has as little numerical dissipation as possible (Miczek et al., 2015). It is necessary to follow slow flows for a long time without the numerics altering the flow's natural evolution. The Gresho vortex Gresho & Chan (1990) can be used to test such a situation. The Gresho vortex is a stable flow that should not change over time. It is set up as a 2D dimensionless circular flow with a tangential velocity \tilde{U}_ϕ that is first increasing with the distance r from the domain centre and is then linearly dropping of to zero further out

$$\tilde{U}_\phi = \tilde{U}_0 \cdot \begin{cases} 5r, & 0 \leq r < 0.2 \\ 2 - 5r, & 0.2 \leq r < 0.4 \\ 0, & 0.4 \leq r \end{cases} \quad (3.44)$$

\tilde{U}_0 is the reference velocity. For convenience \tilde{U}_0 is set to 1.

The dimensionless pressure \tilde{P}_r is chosen such that the flow is stabilized by a pressure gradient working in the opposite direction:

$$\tilde{P}_r = \tilde{P}_0 + \begin{cases} \frac{25}{2}r^2, & 0 \leq r < 0.2 \\ \frac{25}{2}r^2 + 4(1 - 5r - \ln 0.2 + \ln r), & 0.2 \leq r < 0.4 \\ 4 \ln 2 - 2, & 0.4 \leq r \end{cases} \quad (3.45)$$

where \tilde{P}_0 can be used to shift the pressure up and down. In an ideal gas where the ratio of specific heats γ is equal to 5/3 the soundspeed c_s follows a simple relation with the pressure

$$c_s = \sqrt{\frac{5p}{3\rho}}. \quad (3.46)$$

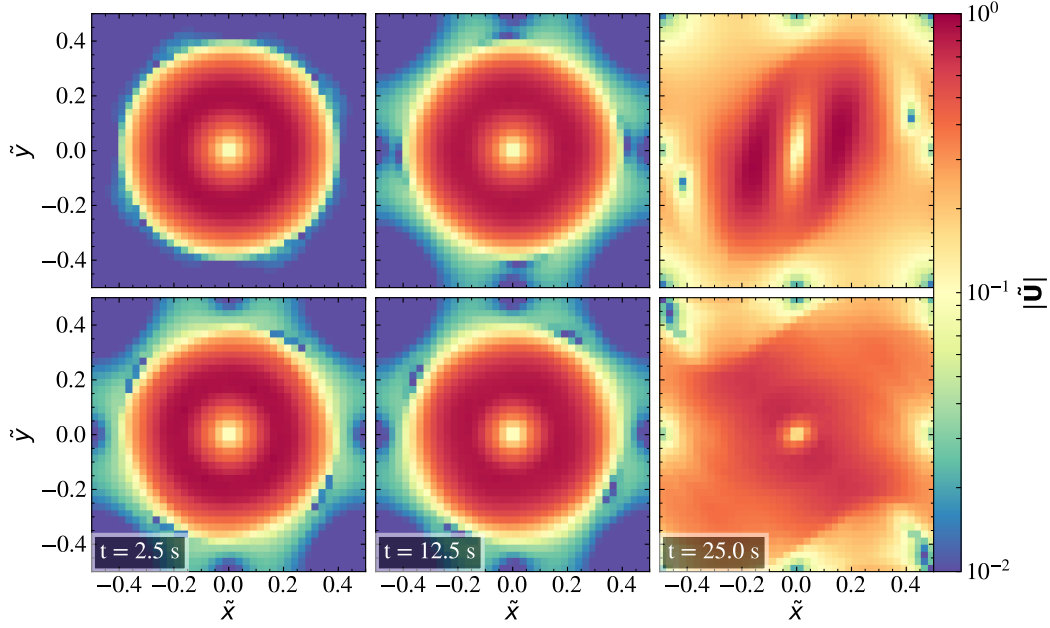


Figure 3.3: Snapshots of the velocity magnitude in the Gresho Vortex test for a Mach number of 10^{-4} after approximately 1, 5, and 10 rotation periods. Results obtained with the PC and RK method are shown in the upper and lower panels, respectively.

It is therefore possible to use P_0 to adjust the soundspeed and therefore the Mach number of the imposed flow.

We performed runs with four different Mach numbers ranging from 10^{-2} to 10^{-10} on a grid of 40×40 cells following Miczek et al. (2015). All runs were able to keep the vortex stable for several rotation periods (see Fig. 3.3), but also did disrupt the vortex after roughly 10 rotation periods. In fact we find that the results are completely independent of Mach number, indicating that the pseudo incompressible approximation holds down to arbitrary low Mach numbers without an increase in numerical dissipation. Guillard & Murrone (2004) showed that this is not the case for many fully compressible schemes.

The disruption of the vortex starts with a slight sloshing that quickly grows in size and elongates the vortex significantly (see top right panel in Fig. 3.3). It is unclear what causes this behaviour, especially since the vortex starts to reassemble itself if the simulation is continued further. The reassembling is clearly caused by the imposed time-independent background pressure gradient. Therefore, there always is a force that drives the vortex flow. This, however, does not explain why the vortex

disrupts in the first place.

It is also important to note that the two integration methods (RK, PC) behave initially almost identically. The top panels in Fig. 3.3 show the results obtained with the PC method, while the bottom panels show the RK method. After one rotation period one can see that the RK method is initially slightly more dissipative since the vortex already developed a velocity "shadow". The PC method develops the same feature but only at later times. When we compare the integrated kinetic energy to the initial kinetic energy in the system we find that after 5 rotation periods, with the PC method the flow has lost about 1% more energy than with the RK method due to dissipation. The overall losses, however are still small and comparable to the preconditioned results in Miczek et al. (2015).

The amount of kinetic energy lost per timestep is roughly constant, as it is expected for numerical dissipation on a static grid. The RK method, however, needs slightly less timesteps to reach a given point in time, which means that it is slightly less dissipative in the long run.

3.5.2 Test_spherical

We checked the numerical accuracy of the RK scheme, by comparing it with the PC scheme in the test_spherical setup provided by MAESTRO. This setup was used in Zingale et al. (2009) to demonstrate the exact mapping of initial models.

The setup represents a white dwarf with constant entropy, without perturbations and heating. The model is created by choosing a central density and temperature and integrating the hydrostatic equilibrium outwards. During the integration, the EOS is forced to maintain a constant entropy.

In this test $\beta_0 = \rho_0$ is fixed. This seems arbitrary but is actually equivalent to the analytic solution for an isentropic stratification. Without any perturbations and heating Eq. 3.37 then reduces to the anelastic constraint Eq. 3.28. A constant background state then implies that the density remains constant at all times irrespective of the velocity field.

In order to compare the two time integrators we therefore impose a random velocity field based on a combination of Fourier modes (Zingale et al., 2009).

On a 384^3 zone grid, the RK method as well as the PC scheme perfectly keep the density and enthalpy profiles constant over time. The maximum relative deviations after $3 \cdot 10^4$ s for both the density and entropy is 10^{-7} .

In Fig. 3.4 we show radial profiles of the velocity magnitude $\langle |\mathbf{U}| \rangle$, where $\langle \cdot \rangle$ denotes a spherically averaged quantity. An isentropic stratification is marginally stable and any small energy input will therefore trigger convective motions. This is true for

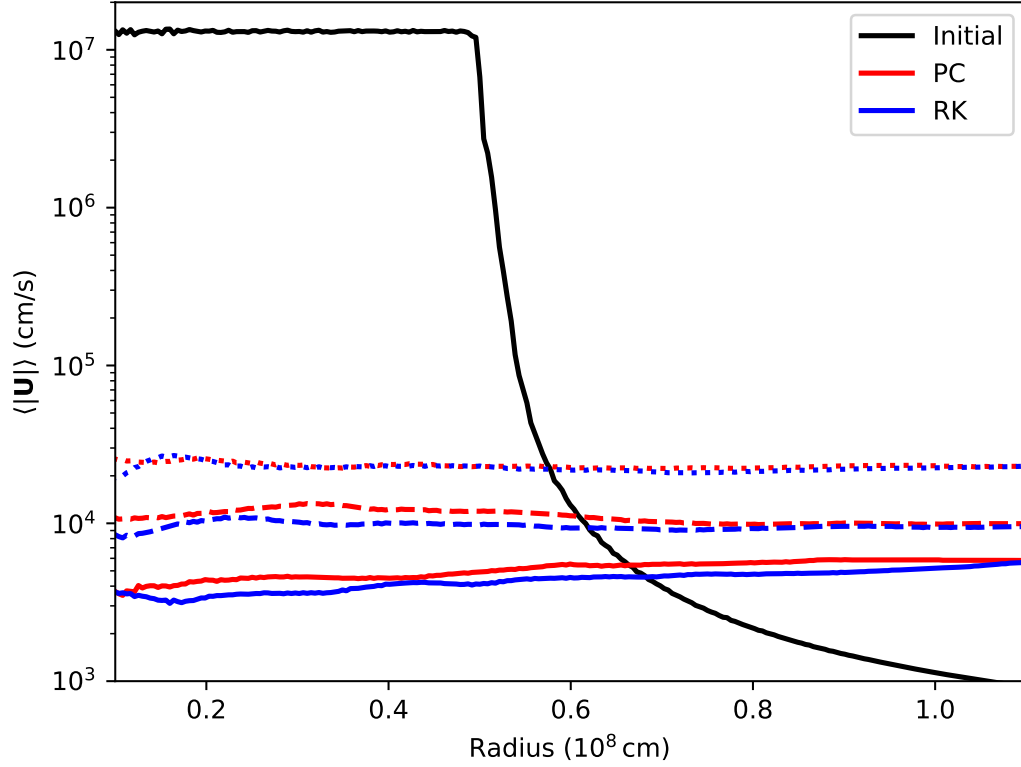


Figure 3.4: Horizontally averaged velocity magnitude profiles of the test_spherical test, after $5 \cdot 10^3$ (dotted), $15 \cdot 10^3$ (dashed) and $30 \cdot 10^3$ s (solid). The initial velocity profile is shown as a black solid line.

the whole star, but the velocity perturbations are limited to the central part (see black line in Fig. 3.4). Since there is no additional energy input into the system, the kinetic energy of the initial velocity field is all the energy available for convection. In the simulation it is quickly spread over the entire star and then slowly dissipates away over time.

Both time integrators give the same qualitative answers, but minor deviations arise at later times (see Fig. 3.4), because of the slightly different dissipation behaviour of the two schemes as described in 3.5.1.

This test shows that the RK method also is able to give qualitatively similar answers to the PC method in 3D simulations with turbulent flows.

3.5.3 Stable Atmosphere

In order to demonstrate the capability of the new time integration scheme, we set up a stable 2D atmosphere with several g-mode cavities. To create the atmosphere we impose a linearly declining density stratification that is modulated by a sine function. The sine function is chosen such, that no density inversion occurs. We discretise the density function of the initial 1D model over 1000 grid point N . The density at a grid point N is given by

$$\rho(N) = \rho_0 + 0.1 + A \cdot \sin\left(\frac{N}{1000}2\pi n\right) + \frac{N\rho_0}{1000} \quad ; N \in \mathbb{N}; N \leq 1000, \quad (3.47)$$

where A and n are the amplitude and the number of periods inside the stratification respectively. ρ_0 is the base density of the model and the additional $+0.1$ ensures that the density does not drop to zero.

Using a constant background gravity, we can now integrate the hydrostatic equilibrium and determine the pressure required for stability. Computing N^2 according to 2.14, we find that $N^2 > 0$ in the whole domain, indicating convective stability. We can also see that N^2 has several peaks, which act as g-mode cavities. (see black line in Fig. 3.5). This test used $n = 5$, $A = 2$, and $\rho_0 = 70 \text{ g/cm}^3$. The density slope was spread out over $1.2 \cdot 10^{10} \text{ cm}$. In the outermost region of the domain (beyond 10^{10} cm) we kept the density constant and damped all velocities analogous to Eq. 3.42. We do this to avoid potential problems with the upper boundary condition.

An atmosphere that is stable against convection should not develop significant velocities. Yet we see in Fig. 3.5 that the PC method shows velocities after a short simulation time of $3 \cdot 10^5 \text{ s}$. While the velocities with a Mach number of the order of 10^{-4} are still relatively small, it is noticeable that the horizontally averaged velocity magnitude profile $\langle |\mathbf{U}| \rangle(r)$ shows several peaks that coincide with the N^2 cavities. Furthermore the velocity increases in amplitude as N^2 increases. An increasing N^2 corresponds to a decreasing τ_{brunt} (see 3.24) which also means that resolving buoyancy effects requires smaller and smaller timesteps.

We therefore explain the velocity peaks with numerical artefacts due to high frequency and therefore unresolved gravity waves. Such numerically caused gravity waves can then be trapped in the g-mode cavities and pile up over time, until the waves finally break.

In general, breaking gravity waves will deposit their energy into the system which will create a mean flow as has been shown in experiments (e.g., Plumb & McEwan, 1978) and numerical simulations (e.g., Coustou et al., 2018). In Fig. 3.5 we also notice a large drop in velocity magnitude after the rightmost peak in N^2 . This is due to the velocity damping and has nothing to do with the phenomenon discussed here.

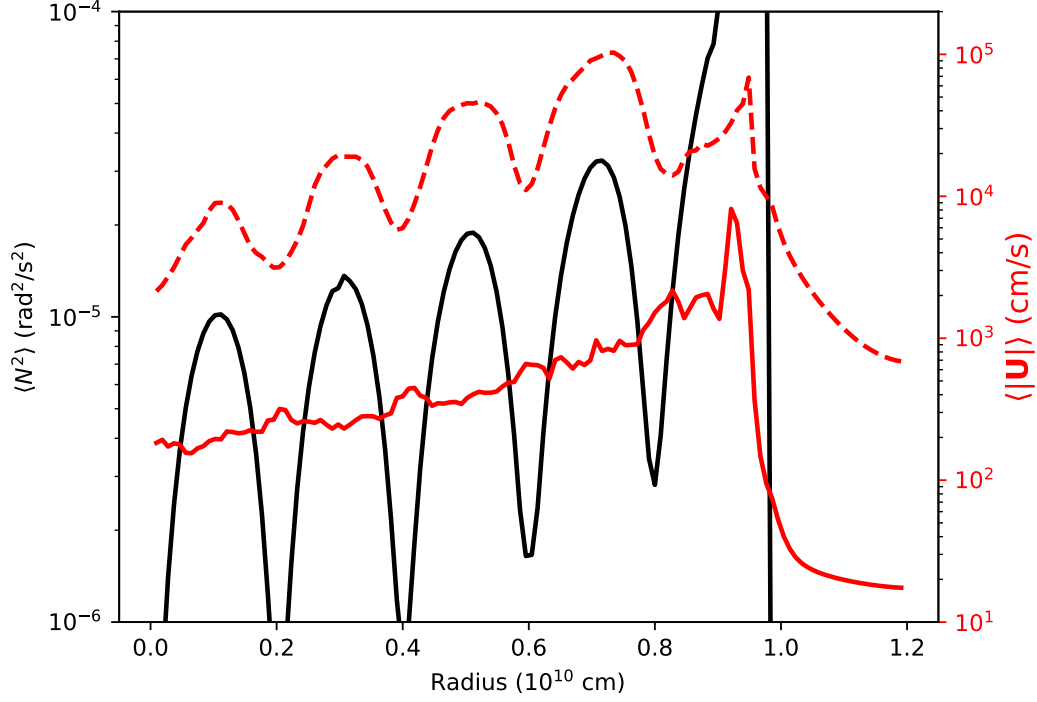


Figure 3.5: Horizontally averaged profiles of N^2 and $|U|$ for the stable atmosphere test. The profiles are shown at $t = 3 \cdot 10^5$ s, where dashed and solid lines correspond to the PC and RK time integration methods, respectively.

Mean flows created by artificial IGWs are problematic for the study we are interested in here. Not only are they unphysical, but the amplitude of the mean flows also tends to be comparable to or even larger than the velocities in adjacent convective zones (see 4.3). They therefore dominate our timestepping and make longterm simulations computationally more expensive.

There also is no guarantee that these flows will stay confined in the g-mode cavity. After some time they might spread out over the entire domain and influence the mixing at the convective boundary that we are interested in.

Using the Runge-Kutta integrator mitigates the problem of artificial IGWs significantly. The multi-step approach seems to smooth the numerical artefacts such that they cannot pile up any longer. This reduces the velocities in the stable zone by more than one order of magnitude to a maximal Mach number of 10^{-5} as can be seen from the solid red line in Fig. 3.5.

The velocities do not drop to zero as one might expect in a perfectly stable

atmosphere, but this is expected as the projection method needs some velocities on the grid in order to converge. These velocities, however, are significantly smaller than the expected convective velocities. In 4.3 we will see that reducing the size of the timestep with the PC method has a similar effect, but obviously increases the computational cost by the same factor as the timestep has to be decreased (usually ≈ 100). The RK method, on the other hand, only requires twice the computational costs of the PC method.

The stable atmosphere test therefore shows that the RK method makes it possible to use the soundproof timestepping criterion 3.25 without unrealistic numerical artefacts in the stable layer at minimal cost increase.

3.5.4 Convective Box

A fully convective simulation can potentially show additional behaviour. It is especially interesting to see how convection behaves in the low Mach number limit, where pressure and density are essentially fully decoupled. Similar to the stable atmosphere an artificial atmosphere with perfect hydrostatic equilibrium is created. In contrast to the stable atmosphere the convective box is defined by its temperature stratification instead of the density. The lower and upper end of the domain are stabilized at constant temperatures T_1 and T_2 , respectively, where $T_1 > T_2$. In the centre of the domain the temperature stratification is exactly adiabatic, i.e., the central layer is marginally stable against convection.

The interfaces between layers with constant temperature and adiabatic stratification are smoothly connected by a temperature gradient ∇_{trans} of the form

$$\nabla_{\text{trans}} = \nabla_0 + 0.5(1 + \tanh(K(y - y_I))) \cdot (\nabla_1 - \nabla_0) \quad (3.48)$$

where ∇_0 and ∇_1 are the temperature gradients below and above the interface at position y_I respectively. Fig. 3.6 shows the resulting initial profiles of ρ , T , and N^2 , where N^2 is a proxy for the stability of the region. A value close to but above zero indicates a marginally stable region.

A similar problem was discussed in Nonaka et al. (2010) but in a different density regime and with a slightly different construction of the background stratification. This setup has been used in Poala (2017) to study convective boundary mixing and has since been extended by L. Horst (priv. communication).

Similar to the test_spherical setup, any additional energy input H_{ext} should be able to trigger convective motions in the central marginally stable zone. Heating by a Gaussian heating function, centred at $y = 0$ (see orange line in Fig. 3.6) initiates convective motions independent of the maximum value of the Gaussian $H_{\text{ext,max}}$. Testing heating rates from $H_{\text{ext,max}} = 100 \text{ erg/g/s}$ to only 0.01 erg/g/s the PC

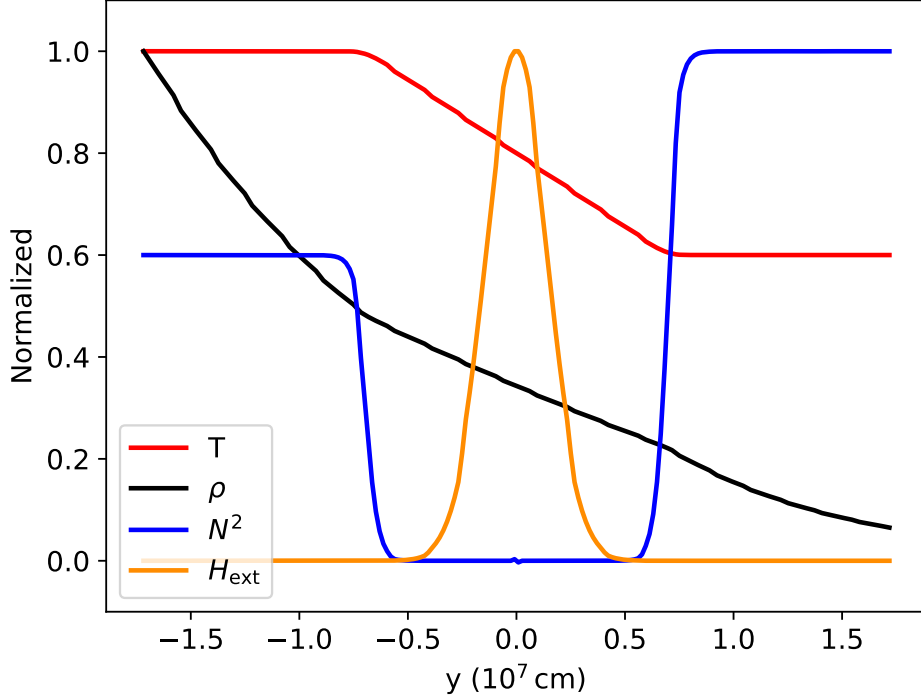


Figure 3.6: Horizontally averaged profiles of the initial model in the convective box test. The curves are normalized to their maximum values.

scheme and the RK integrator have been compared. Fig. 3.7 shows the maximum ($\max(\text{Ma})$) and averaged ($\overline{\text{Ma}}$) Mach numbers in the marginally stable region in the left and right panel, respectively, where \bar{x} denotes the density weighted volumetric average of quantity x . MLT predicts that the convective velocities scales as $\propto H_{\text{ext}}$ (see 2.1). In Fig. 3.7 we plot this scaling law as dashed lines, where we chose the time averaged values for $\max(\text{Ma})$ and $\overline{\text{Ma}}$ from the simulation with $H_{\text{ext},\text{max}} = 1 \text{ erg/g/s}$ as the reference value of the scaling.

The results show that the expected scaling relation is mostly fulfilled down to very low heating rates. The resulting Mach numbers range down to a few times 10^{-4} , comparable with expected Mach numbers of core convection during hydrogen burning. With a lower heating rate, convection needs a longer time to develop. With the lowest heating rate $H_{\text{ext},\text{max}} = 0.01 \text{ erg/g/s}$ convection actually does not fully develop during the simulation time (see leftmost panel in Fig. 3.8). Hence the lowest heating run does not match the scaling relation. The run with a heating of

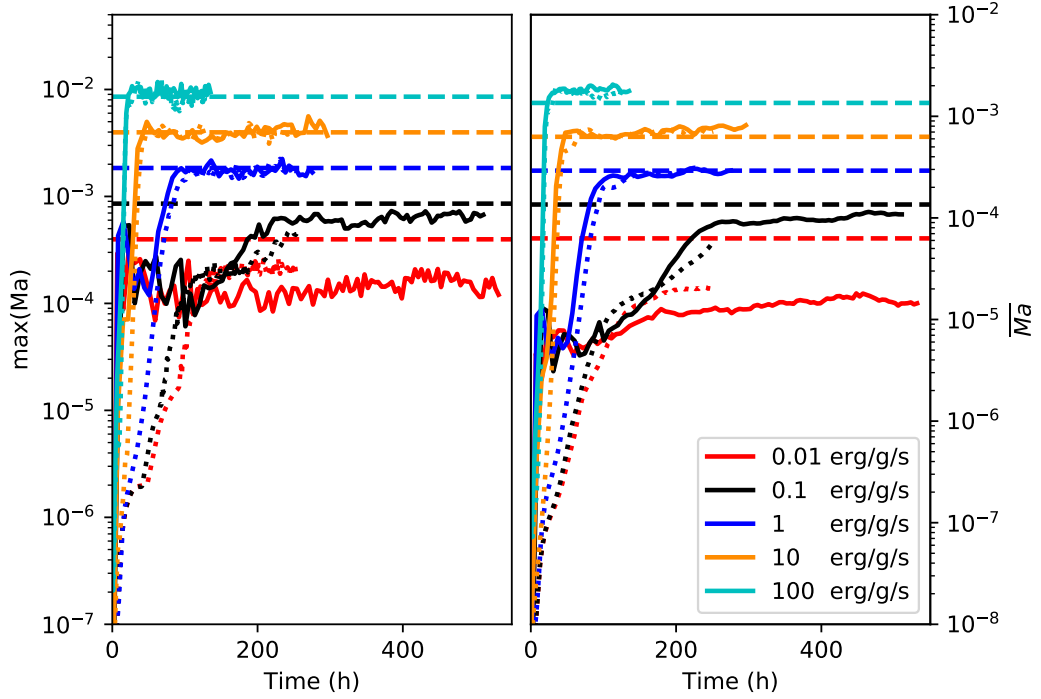


Figure 3.7: Maximal (left panel) and density averaged (right panel) Mach number inside the marginally stable region of the convective box test. Full and dotted lines show the RK and PC results, respectively. Different colors show different maximum heating rates $H_{\text{ext,max}}$, while the horizontal dashed lines indicate the scaling expected from MLT.

$H_{\text{ext,max}} = 0.1 \text{ erg/g/s}$ develops convection only in the upper half of the marginally stable zone. In the long run we would expect that convection spreads to the bottom half as well. Since only half the zone is convective, the average Mach number is lower than expected.

In simulations using the PC method we reduced the timesteps in order to avoid large spurious velocities from the outer boundaries. With the RK method this is unnecessary. As can be seen from Fig. 3.8 the runs with high heating rates do not show any peculiar velocities at the upper boundary, while the lower heating rates this is still the case. Nevertheless the velocities remain small. Since we do not need to reduce the timesteps in RK simulations, we can compute the same flow problem with less timesteps, increasing the computational efficiency. In this test the PC runs took 100000 timesteps each, while the RK runs reached similar simulation times after

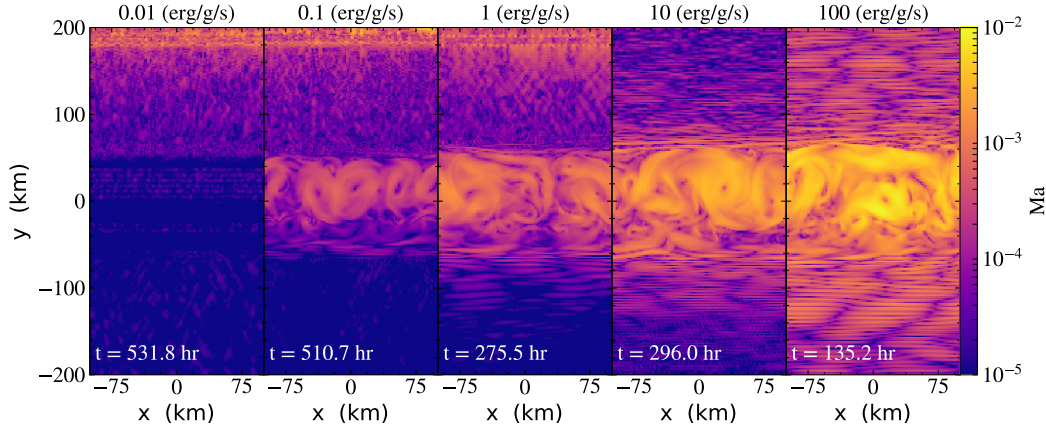


Figure 3.8: Snapshots of the Mach number in the convective box tests with different heating rates, where the maximum heating rate is given at the top of each panel.

only 5000 timesteps. Even after considering that the RK scheme is twice as expensive as the PC scheme, the RK scheme provides a speed-up of a factor of 10 for this test.

3.6 Initial Models

Multidimensional hydrodynamical simulations require initial data that represent the desired stratification as accurately as possible. We produce our initial data by using stellar evolution models produced by the Lagrangian 1D stellar evolution code GARSTEC (Weiss & Schlattl, 2008).

The models considered in this study use a solar calibrated mixing length $\alpha = 1.71$ and have a solar composition of 70.9% hydrogen, 27.5% helium and 1.6% heavier elements. The abundances of specific heavier elements are taken from the measurements of the relative solar abundances by Grevesse & Noels (1993), scaled to match the total metallicity. Garstec uses a tabulated EOS from the OPAL collaboration (Rogers & Nayfonov, 2002).

The 1D stellar evolution of our models is stopped once they reach the beginning of the main sequence, i.e. the point where hydrogen burning is fully established. The equilibrium energy production rate in pp chain and CNO cycle is set by the slowest reaction involved. Initially the composition in the burning region does not fulfil the equilibrium conditions, i.e., the faster reaction rates of helium-3 and carbon dominate the energy production until an equilibrium state is reached. Consequently our initial models already consumed $\approx 1\%$ of the available hydrogen before they

reach the main sequence.

This leads to a very shallow variation of the hydrogen profile at the boundary of the convective core, which is very sensitive to single mixing events. Therefore, changes in the hydrogen profile can be seen quickly without mixing massive amounts. The quick reaction time consequently also allows us to study the time evolution of the mixing.

This study focuses on the convective cores of intermediate mass stars. An intermediate mass star has a convective core during its main sequence evolution and a radiative envelope around it, i.e., the star is more massive than $\approx 1.2 M_{\odot}$. The star is, however, not massive enough to go all the way to core collapse and will end its life as a white dwarf. Stars between $\approx 1.2 M_{\odot}$ and $\approx 8 M_{\odot}$ fulfil both criteria and are hence considered intermediate mass stars (see e.g., Kippenhahn et al., 2012). Here we will show 2D simulations of the convective core of a $3.5 M_{\odot}$ star. We chose this mass, because it has a convective core large enough to avoid problems with the overshooting description (see 2.2). Intermediate mass stars are also preferred targets for observers to study IGWs. Using the observed frequencies of IGWs, originating at the boundary of the convective core it is then possible to estimate the size of the mixed cores (Deheuvels et al., 2016; Moravveji et al., 2016).

In order to calibrate the overshooting parameter introduced in 2.12 (see 4.4 for a description of the calibration method) we need models computed with and without a convective overshooting description.

Garstec implements overshooting in the diffusive description as in 2.12. In order to avoid the problems of small convective cores described in 2.2, a geometrical cutoff of the form 2.13 is usually applied.

In order to get results that are more comparable with other codes, we computed our overshooting models *without* the cutoff.

Our models with overshooting start from the same initial conditions as the non overshooting ones and are then self-consistently evolved until they reach a similar central hydrogen content as the models without overshooting. The variation in the central hydrogen content is less than 10^{-4} within a set of models.

As a consequence of the self-consistent computation and the fact that we assume a radiative temperature stratification in the overshooting region, we find that the overshooting models have a slightly larger convective core, according to the Schwarzschild criterion (see first column in Table 4.2).

Garstec provides us with thermally relaxed models on a Lagrangian grid. In order to use those in MAESTRO, we need to map the model onto an Eulerian grid. The interpolation introduces slight deviations from the hydrostatic equilibrium (HSE) into the models. However, MAESTRO expects its background state to be in perfect

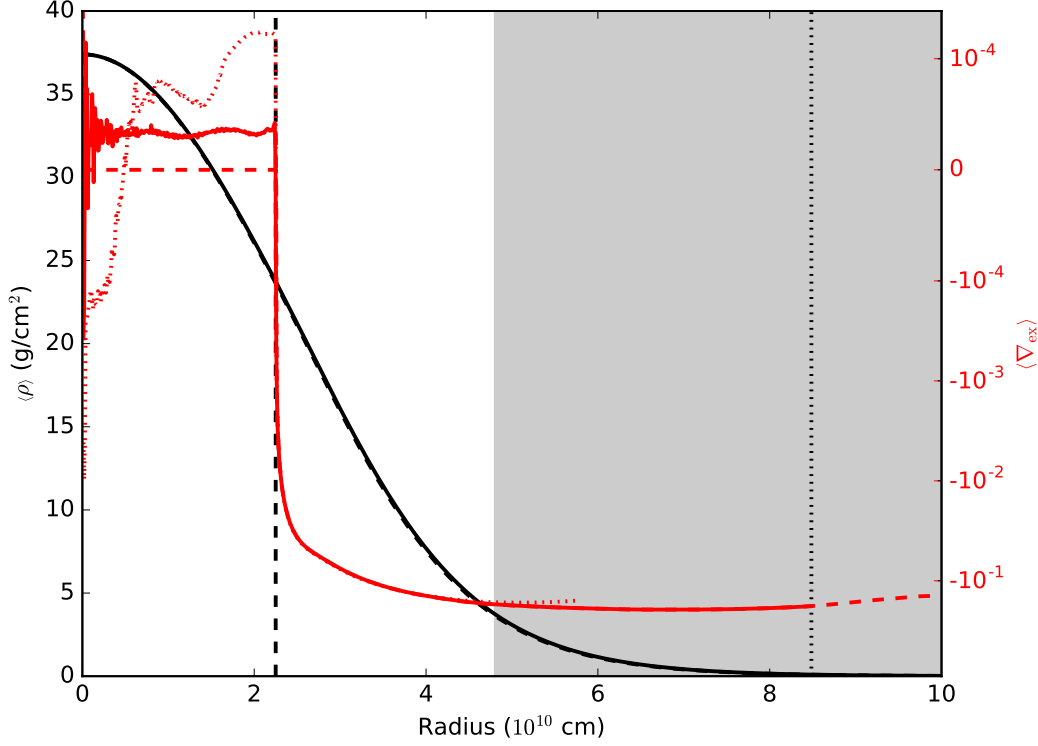


Figure 3.9: Initial spherically averaged density (black) and superadiabaticity (red) of the ImHrk (solid) and ImHpcT (dotted) simulations. Dashed lines give the stratification as predicted by Garstec. The vertical dashed and dotted lines indicate the boundary of the convective core and of the domain respectively. In the shaded region we damp the velocities.

HSE. Therefore it is necessary to reintegrate the HSE

$$\frac{\partial P}{\partial r} = -g\rho. \quad (3.49)$$

The integration is also used to slightly smooth out the composition profiles by a moving average. This is done in order to avoid large spikes in N^2 at the convective boundary, as this would lead to problems similar to the ones discussed in 3.5.3.

During the integration, we also switch from the OPAL EOS used by Garstec to the Helmholtz EOS in MAESTRO. With this change we modify the thermal structure of the models. We can therefore not guarantee thermal equilibrium any longer. MLT predicts that the temperature gradient in the convective zones of our models to be almost perfectly adiabatic but with a small superadiabaticity of the order of 10^{-8} . In a hydro simulation superadiabaticity acts as an energy reservoir for the convective

flow. A small change in the temperature stratification can increase the internally stored energy significantly or remove the convective core entirely. In order to keep the simulations energetically as close to the initial models as possible, we preserve the excess of the temperature gradient $\nabla_{\text{ex},1\text{D}} = \nabla_{\text{mlt}} - \nabla_{\text{ad,OPAL}}$ over the adiabatic gradient $\nabla_{\text{ad,OPAL}}$ obtained from the OPAL EOS of the 1D stellar model, where ∇_{mlt} is the temperature gradient predicted by MLT. In the integrated model the superadiabaticity $\nabla_{\text{ex}} = \nabla - \nabla_{\text{ad,Helm}}$ is set by the unknown temperature gradient ∇ and the adiabatic gradient obtained from the Helmholtz EOS $\nabla_{\text{ad,Helm}}$. By enforcing $\nabla_{\text{ex}} = \nabla_{\text{ex},1\text{D}}$ the unknown ∇ can then be computed as

$$\nabla = \nabla_{\text{mlt}} - \nabla_{\text{ad,OPAL}} + \nabla_{\text{ad,Helm}}. \quad (3.50)$$

By simultaneously solving equations 3.49 and 3.50 using a Runge-Kutta method to integrate outwards from the stellar center we minimize the energetic modifications to the 1D model during the integration.

It is also possible to preserve other quantities like the temperature itself during the integration, but that again can lead to models with inconsistent energy content. In Fig. 3.9 we demonstrate the effect by comparing initial models where the temperature, respectively the temperature gradient were kept constant. Keeping the temperature constant during reintegration (red dotted line) leads to a temperature stratification that is stable in the very centre of the convective core and largely superadiabatic towards the convective boundary. Keeping the superadiabaticity constant (red solid line), on the other hand, achieves a more realistic temperature stratification with a small but constant superadiabaticity.

Trying to fulfil Eq. 3.50 and Eq. 3.49 simultaneously in combination with the EOS leads to an overdefined system, since HSE already provides a temperature (and ∇) based on the pressure and density stratification derived from Eq. 3.49. The integration is therefore not exact. In practice we achieve a hydrostatic equilibrium with a relative accuracy of 10^{-5} and a temperature gradient that is only $5 \cdot 10^{-5}$ larger than the adiabatic temperature gradient in the convective zone. While ∇_{ex} is still three orders of magnitude larger than predicted by MLT (red dashed line in Fig. 3.9), it is sufficiently small for our simulations.

We set up our simulations with a rather large stable layer on top of the convective zone. The domain spans six pressure scale heights in total (see Fig. 3.9). We do this in order to keep the computationally complicated outer boundary as far away from the area we are interested in. This way the influence from the outer boundary on the mixing can be minimized.

Since MAESTRO uses a Cartesian grid we can include the centre of the star into our simulation. We therefore do not need to cut out the part with the highest heating rates in the domain. The equilibrium rates discussed in 3.1.1 reproduce the nuclear

energy generation of the 1D models, within a factor of two. We want to stress here, that we do *not* use an additional boosting factor in any of the simulations, which is common practice for fully compressible hydrodynamics in stellar interiors (see, e.g., Meakin & Arnett, 2007; Cristini et al., 2019).

On the other hand, the Cartesian geometry causes problems at the corners of the domain (Gilet, 2012). As discussed in 3.4 these problems can be mitigated with a velocity damping of the form 3.42. In our models of $3.5M_{\odot}$ stars the damping is smoothly turned on over a distance of $5 \cdot 10^9$ cm and is fully active beyond a radius of $5.3 \cdot 10^{10}$ cm (see shaded region in Fig. 3.9).

Robinson et al. (2003) found that velocities and temperatures are strongly influenced by domain boundaries up to a distance of at least two pressure scale heights. Our velocity damping sets in ≈ 2.5 pressure scale heights away from the convective boundary, minimizing boundary effects.

Even though the velocities are damped, it is done before the final projection. This means that there will always be some velocities in the outer zone, since the velocity constraint cannot be fulfilled otherwise. Consequently, there will be some flow across the domain boundary. These boundaries are treated as open outflow boundaries, which reduces reflections of waves but reduces the total mass in the system with time. Due to the velocity damping and the low densities in the outer area, the mass loss, however, is negligible during the simulation time.

The symmetry of the mapped model is broken by imposing a random velocity field based on a combination of Fourier modes (Zingale et al., 2009).

Chapter 4

2D Simulations

This chapter focuses on two dimensional simulations. First we will discuss an intermediate mass star of $3.5M_{\odot}$ and the effects of different time integration methods and initial model preparation, as well as resolution in time and space. In 4.4 and 4.6 we will then use these insights to draw conclusions on the extent of the mixed region and the temperature gradient within it. The mass dependence of our findings will be discussed in 4.7.

In total we performed 10 simulations, which were mostly computed on the MPA clusters `pascal`, and `laplace` using a total of $3.6 \cdot 10^5$ CPU hours (Table 4.1). Our longest simulation spans more than 6 years of physical time and covers roughly 340 convective turnover timescales.

The results in this chapter will be published in a forthcoming paper.

4.1 Transient

The initial phase of the simulations show some peculiar transient features that renders the initial phase unusable for the forthcoming analysis. In this section we will explain, where these features come from and how we can define the time beyond which their influence can be neglected.

Initially the stars are at rest, except for a small velocity perturbation in the inner part of the expected convective zone. This is enough to break the symmetry of the system and the simulations develop convective motions. Convection uses the energy source that is easiest to tap into. In the beginning this is the internal energy stored in the small superadiabaticity ∇_{ex} (see 3.6). Internal energy can be converted into kinetic energy very rapidly leading to a sharp rise of the velocity magnitude in the convective zone (CZ). This energy supply is exhausted once an adiabatic stratification is achieved. From that point on convection has to draw its energy from the comparably smaller, limited heating term. In combination with the dissipation of the kinetic energy present, this will lead to a decrease of convective velocities over

Name	Resolution	1D Model	f_{ov}	Int.	dt	t_{\max} (s)	$t_{\max}/\tau_{\text{conv}}$
ImHrk	1024^2	∇_{ex}	0	RK	\mathcal{U}	$2 \cdot 10^8$	340
ImMrk	512^2	∇_{ex}	0	RK	\mathcal{U}	$1 \cdot 10^8$	200
ImvHrk	2048^2	∇_{ex}	0	RK	\mathcal{U}	$1 \cdot 10^7$	20
ImHpc	1024^2	∇_{ex}	0	PC	\mathcal{U}	$6 \cdot 10^7$	100
ImHpcIGW	1024^2	∇_{ex}	0	PC	IGW	$1 \cdot 10^7$	20
ImHpcT	1024^2	T	0	PC	\mathcal{U}	$2 \cdot 10^8$	430
ImHrk-1	1024^2	∇_{ex}	0.01	RK	\mathcal{U}	$8 \cdot 10^7$	140
ImHrk-1.7	1024^2	∇_{ex}	0.017	RK	\mathcal{U}	$3 \cdot 10^7$	50
ImHrk-2	1024^2	∇_{ex}	0.02	RK	\mathcal{U}	$7 \cdot 10^7$	130
ImHrk-3	1024^2	∇_{ex}	0.03	RK	\mathcal{U}	$4 \cdot 10^7$	70

Table 4.1: Overview of our 2D simulations of $3.5M_{\odot}$ stars. The second column gives the grid resolution. While the third column gives the preserved quantity during integration of the initial model, the fourth column shows whether overshooting has been applied in the stellar evolution calculation. The fifth and sixth column give the time integration method and the decisive quantity for the timestep selection, respectively. The last two columns show the physical time at the end of each simulation and the number of convective turnovers covered.

time.

Fig. 4.1 illustrates this behaviour by showing the time evolution of the average velocity magnitude $|\overline{\mathcal{U}}|_{\text{CZ}}$ in the CZ, where \bar{x} denotes the spatial density weighted average of quantity x . In all simulations the initial perturbations quickly grow into a peak in the convective velocities after $\approx 10^5$ s. After that the velocities drop significantly over a few convective turnover times, until a quasi-steady velocity field is established.

This is a well known phenomenon that has been observed in many previous studies as well (see e.g. Meakin & Arnett, 2007; Jones et al., 2017; Gilet et al., 2013).

Quantifying when a quasi-steady phase is reached is ambiguous, as we are dealing with a dynamical system where even averaged velocities change constantly over time. It is also possible that a velocity field is quasi-steady over a few convective turnovers, but evolves over much longer timescales due to e.g., changes in the chemical composition and therefore different heating rates.

Boesler & Weber (2017) define tests based on the time averaged velocity $\langle |\overline{\mathcal{U}}| \rangle_t = \overline{\mathcal{U}}$ and its standard deviation σ to determine whether a steady state has been reached. $\overline{\mathcal{U}}$ and σ are determined over N consecutive timesteps as a moving average such that we can assign each timestep its own $\overline{\mathcal{U}}$ and σ . Looking at two consecutive timesteps (subscript 1 and 2) one can then compare the following quantities, which Boesler &

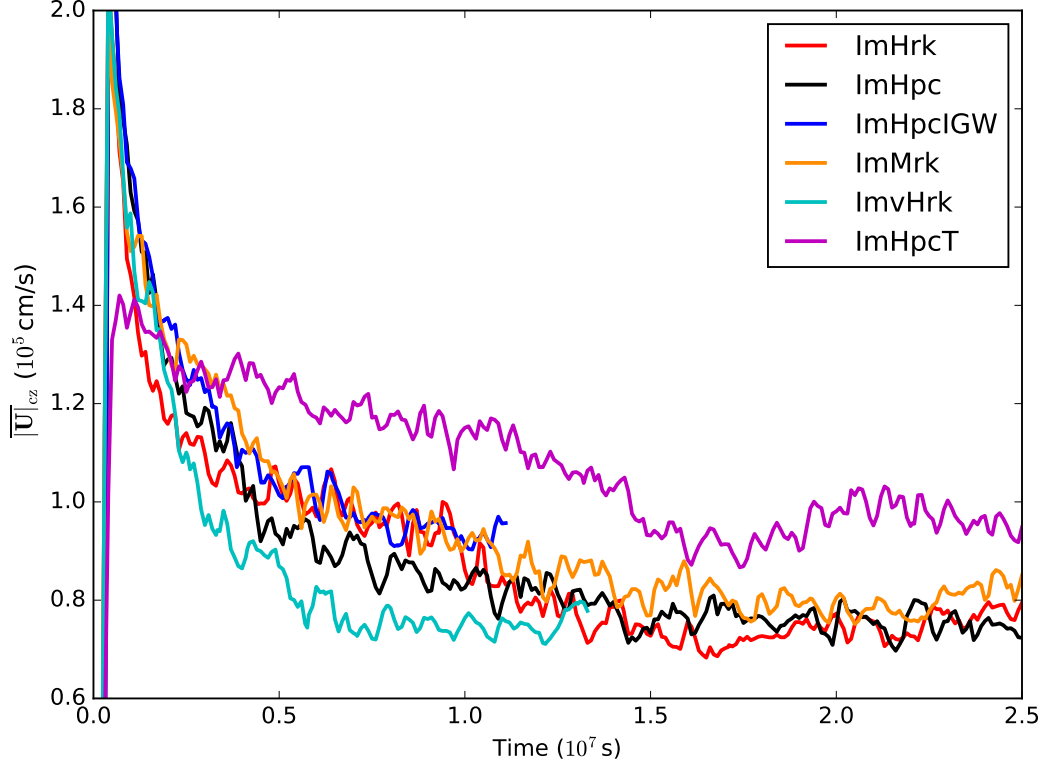


Figure 4.1: Evolution of the density averaged convective velocity magnitude for different simulations of a $3.5M_{\odot}$ mass star.

Weber (2017) labelled as T - and F -test

$$T = \frac{|\overline{U}_2 - \overline{U}_1|}{\sqrt{\sigma_1^2 + \sigma_2^2}} \quad (4.1)$$

$$F = \frac{\max(\sigma_1^2, \sigma_2^2)}{\min(\sigma_1^2, \sigma_2^2)}. \quad (4.2)$$

In a perfect steady state the velocity field will not change in time and the standard deviation will be constant. T therefore goes to 0, while F approaches 1.

We try to evaluate the presence of a quasi-steady state in post-processing. Since we do not output every timestep we cannot construct the time averages as proposed in Boesler & Weber (2017). We will therefore skip the time integration step and instead assume that each output file is representative for the timespan in between output files. This is a valid approach, because we expect that the velocity field does evolve on a timescale of τ_{conv} and we write output files every 10^5 s, i.e., 5–10 output

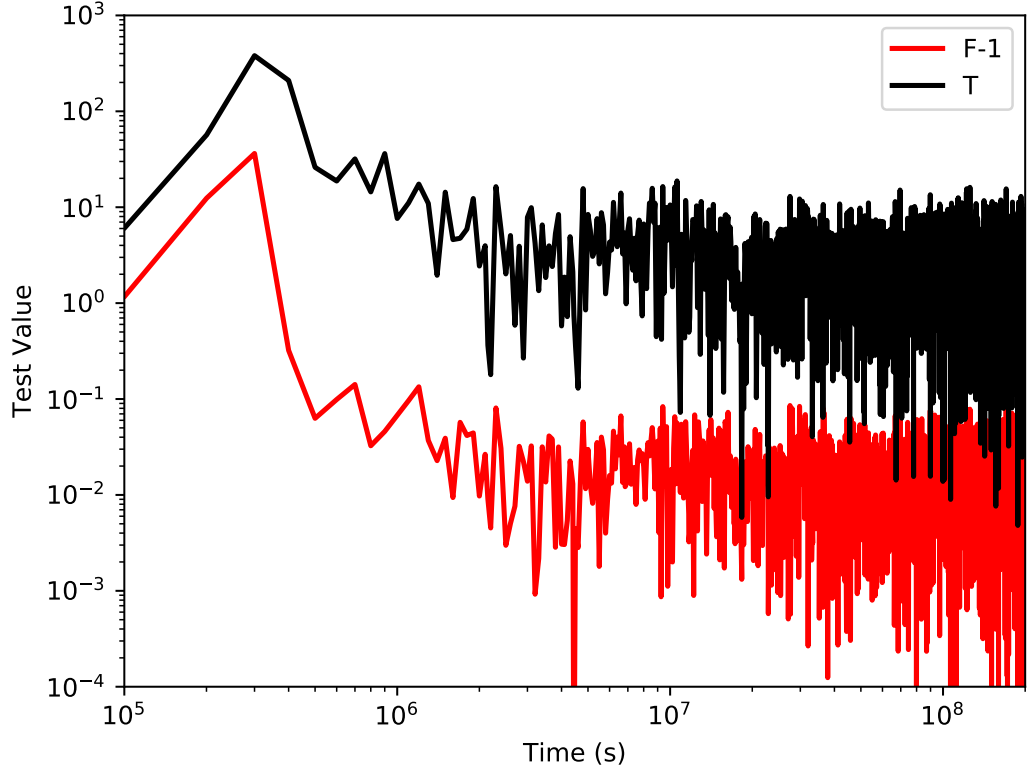


Figure 4.2: F and T test of the ImHrk simulation. We plot F-1 to separate the lines more clearly.

files per convective turnover. We can then use consecutive output files to compute the test values and analyse the evolution.

In Fig. 4.2 we display the results for the ImHrk simulation. We can see, that the F and T -test show a similar behaviour over time. During the initial transient the tests increase by two orders of magnitude and drop shortly thereafter. After a few 10^6 s both tests go to a constant value.

As expected, F goes to 1, indicating a constant σ . We plot $F - 1$ in Fig. 4.2 in order to show that our value of F is only a few percent larger than 1.

The T -test in Fig. 4.2, however, does not go to zero as predicted by Boesler & Weber (2017), but instead approaches a value of roughly 3. The reason for that are the missing time averages in our analysis. While dealing with single output files we cannot expect that \bar{U} stays constant over the time between two outputs. One would rather expect that \bar{U} varies on the order of the standard deviation if a quasi-steady state has been reached. The nominator of 4.1 will then not go to zero but will

approach a value of the order of 1σ . The T -test is therefore expected to give a value > 0 that is roughly constant over time in agreement with our results. The value of 3 as the converged value for F , indicates that within 10^5 s the field changes by roughly 3σ in agreement with a 99 % confidence interval. This is suggesting that the single standard deviations are indeed representative for the whole time evolution and the velocity field is in a quasi-steady state.

In the quasi-steady state, the velocity field in the convective zone is dominated by two counter-rotating vortices (see Fig. 4.3). Even though these vortices do move around and collide with each other, they never annihilate due to vorticity conservation in 2D turbulence. As expected from the inverse energy cascade in 2D simulations (Kraichnan, 1967; Batchelor, 1969; Kraichnan & Montgomery, 1980) the vortices fill as much space as is available in the CZ.

Throughout the simulations the source term S in Eq. 3.37 is of the order of 10^{-14} , which corresponds to an almost completely incompressible flow.

Fig. 4.4 shows time averages, denoted by $\langle \cdot \rangle_t$, of the spherically averaged velocity magnitude profiles $\langle |U| \rangle$. Our nomenclature gives the order in which averages are performed from the inside to the outside, e.g., the quantity $\langle \langle |U| \rangle \rangle_t$ is first spherically averaged and then time averaged over several output files. In Fig. 4.4 the time averaging was performed over all outputs between $5 \cdot 10^6$ s and 10^7 s. This is the time span covered by all the simulations where the F and T -test indicate a steady state. The average is using 50 output files and covers roughly 10 convective turnover timescales.

The averaged velocity profile has a maximum towards the centre of the star and a sharp drop in velocity magnitude at the convective boundary. For comparison we also plot the velocity predictions by MLT (black dashed line in Fig. 4.4). The most obvious difference between the MLT prediction and the simulations is the behaviour towards the centre. Since MLT takes the centre of the star, as a convective boundary, the velocity there is expected to drop to zero. In a multi-D simulation and in nature the star's centre, however, is not at the edge of the CZ. On the contrary, the centre of the star is also the centre of the CZ. The MLT prediction at that point is hence inconsistent for central convective zones.

On the outer edge of the CZ the MLT prediction, on the other hand, follows the observed profile nicely. The profiles in the simulations are, however, shifted upwards by more than one order of magnitude. This is due to the vortices, where their velocities increase towards the outer edges. Similar to a hurricane on earth, there exists a pressure gradient from the centre to the edge of the vortices. Even though this difference is only of the order of 10^{-4} it still creates a noticeable pressure gradient that drives large velocities. In 5.1 we will see that 3D simulations, which do not show these stable vortices, give velocity magnitudes much closer to the MLT prediction. The rather large mismatch between 2D simulations and MLT is hence

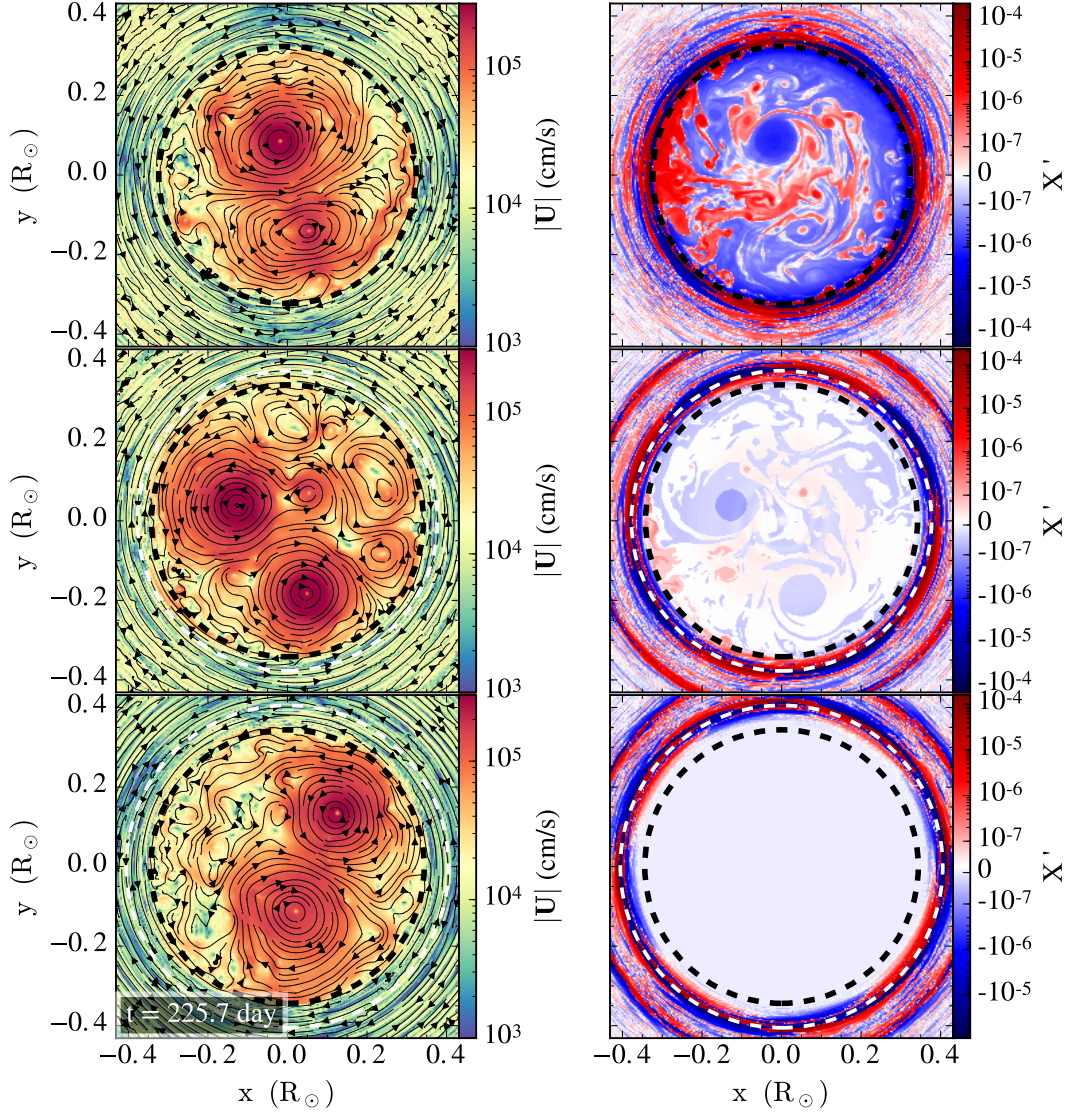


Figure 4.3: Velocity magnitude (left panels) and perturbations of the spherically averaged hydrogen profile (right panels) of the ImHrk, ImHrk1.7, ImHrk3 simulations after $2 \cdot 10^7$ s from top to bottom, respectively. The white dashed circles denote the initial size of the mixed core, while the black dashed circles show the size of the convective core according to the Schwarzschild criterion. The streamlines in the left panels indicate the direction of the flow.

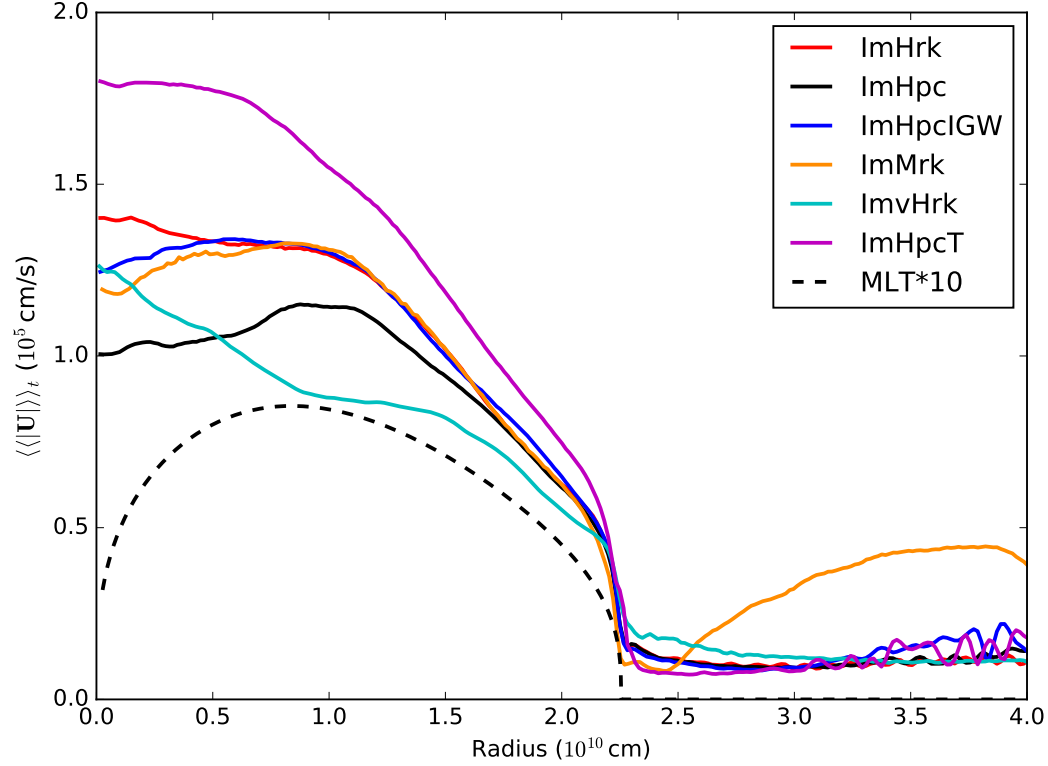


Figure 4.4: Time averaged velocity profiles for different simulations of a $3.5M_{\odot}$ star. We averaged the data from $5 \cdot 10^6$ s till 10^7 s using 50 output files. The black dashed line shows the velocity profile predicted by MLT scaled by a factor of 10.

the sole consequence of the reduced dimensionality.

In contrast to MLT predictions the velocity magnitude at the convective boundary does not drop to zero, but remains finite in the stable layer. Simulations of convective envelopes (see ,e.g., Freytag et al., 1996; Pratt et al., 2017) find that the velocity decreases with increasing distance to the convective boundary. In our case we find the opposite behaviour. The velocity magnitude starts to slowly increase the deeper we go into the stable layer, the reason being IGWs. As described in 2.3, the amplitude of IGWs scales as $\rho^{-1/2}$. IGWs created by envelope convection will travel into denser matter and will hence be damped. Centrally created IGWs, on the other hand, propagate outwards, where the amplitude will increase due to the reduced density of the surrounding fluid. In a wave dominated regime it is therefore natural to see opposite behaviour in the velocity magnitude between envelope and central convective regions. This effect can also be seen in core convection studies by Rogers

(2015) and Edelmann et al. (2019).

The simulations ImHrk, ImHpc and ImHpcIGW differ by the time integration method used. ImHrk uses the Runge-Kutta time integrator, while ImHpc and ImHpcIGW use the predictor-corrector scheme. In addition to the PC scheme, ImHpcIGW also uses reduced timesteps in order to resolve IGWs better. This will be discussed in more detail in 4.3. Using smaller timesteps ImHpcIGW should be more accurate than ImHpc. We see that in the CZ ImHpcIGW and ImHrk agree almost perfectly, except for a small difference in the very centre of the simulation. This difference can be explained by the reduced number of cells per radial bin (Cartesian grid), which leads to increased statistical fluctuations on the average.

ImHpc, on the other hand, has about 30% smaller velocities. This confirms two points. First, in order to achieve the same level of accuracy in the PC and the higher order RK method, the PC method has to use smaller timesteps. Moreover it also shows that at the same level of accuracy the PC and RK integrator produce the same convective pattern.

In Fig. 4.1 ImHrk and ImHpc also reach the same final velocity, indicating that reproducing the average velocity in the CZ does not require the highest time accuracy in the long run. The ImHpcIGW simulation was not run long enough to reach a constant velocity, but it is perfectly following the behaviour of ImHrk up until the end of the simulation. It is safe to assume that this simulation will also reach a similar final velocity state.

From Fig. 4.1 and 4.4 we can also see the influence of resolution on the setup. The simulations ImMrk, ImHrk, and ImvHrk have the same initial state and integration method, but use different resolution levels.

ImMrk and ImHrk agree perfectly inside the CZ except near the very centre. There less cells are available for the average, i.e., the fluctuations are expected to be larger. On the other hand, ImvHrk has $\approx 10\%$ lower velocities there. Looking at Fig. 4.1 the difference is easily explained by the fact, that ImvHrk reaches the quasi-steady state at an earlier time than ImHrk. The velocities in the averaging window are therefore already slightly smaller.

In Fig. 4.1 we can see that the runs with different resolution end up with the same average velocity in the CZ, indicating convergence. From these results one could argue that a resolution of 512^2 is already converged. For the CZ this might actually be true. In the stable layer, however, the ImMrk simulation shows velocities that are ≈ 1 order of magnitude larger than in ImHrk and ImvHrk. This is due to unresolved IGWs, similar as in the stable atmosphere test problem in 3.5.3 (see also 4.3). The onset of this discrepancy can also be seen in the profiles of ImHpcIGW and ImHpcT at large radii, but at a much lower level. Nevertheless it becomes clear that we

need at least a spatial resolution of 1024^2 in order to resolve the stable layers properly.

The ImHpcT simulation uses an initial model which reproduces the temperature of the 1D model, instead of its temperature gradient excess ∇_{ex} . As shown in Fig. 3.9 (red dotted line), this leads to an increased superadiabaticity in most parts of the CZ. The additional energy stored in the temperature gradient is then used to power the convective motions for an extended period of time. The transient is longer because the additional energy cannot be quickly dissipated. In fact, ImHpcT reaches a steady state with an average velocity that is $\approx 30\%$ larger than in models that reproduce ∇_{ex} (see Fig. 4.1). This is also obvious from the ImHpcT velocity profile in Fig. 4.4 which has a similarly increased maximum velocity compared with the ImHrk simulation.

4.2 Convective Boundary

Before we can analyse the mixing behaviour around the convective boundary, we first need to define its position. In MLT the position of the convective boundary is well described by the Schwarzschild criterion, but already the consideration of overshooting makes it necessary to differentiate two convective boundaries. While the driving region is again set by the stability criterion, the star sees a larger convective region in terms of available fuel. The limit is set by the homogeneously mixed region of the overshooting layer. In a dynamical system the complexity increases even further, since now the actual motion needs to be considered as well.

As we can see there are many ways to define the location of the convective boundary, but we can categorize them into three different classes.

Structural boundaries are defined by classical stability considerations. The Schwarzschild criterion uses the temperature stratification to define stable and unstable regions. As such it can also be interpreted as the driving region of convection. The convective boundary is then set by the structure of the star, which remains constant over dynamical timescales. Local variations therefore tend to be negligible and the position of the boundary only changes on thermal timescales.

Dynamical boundaries use the convective velocities to define the extent of a CZ. The difference to the structural boundaries lies in the fact that here the extent of a CZ can be determined by a single localized event, while the structural boundaries largely rely on the background stratification. The mixing mechanisms at convective

boundaries discussed in 2.2 and their respective mixing depths are examples of dynamical boundaries. Dynamical boundaries therefore capture the driving as well as the breaking region of convection.

Chemical boundaries show the extent of the mixed region around a CZ. They can therefore be interpreted as the result of the mixing due to the dynamical events. This is the boundary that usually defines the overshooting region in 1D models as discussed in 2.2.

For each category one can define a set of boundary conditions. One can even define criteria that combine two categories. An example for that would be the Ledoux criterion, which includes the structural temperature gradient as well as a contribution from the chemical gradient. A criterion based on composition fluxes, on the other hand, combines dynamical and chemical effects.

It is clear that the precise location of the convective boundary is ambiguous and depends on which quantity we look at. By focusing on the three basic boundary types, however, we can define a simple model that describes the mixing around CZs. Assuming that we have a stellar evolution model, computed without overshooting one would naively expect that a multi-D simulation shows the following behaviour on a dynamical timescale:

- initially structural and chemical boundaries agree and there is no dynamical boundary since the initial velocities are close to 0
- convection starts to develop in the region that is convectively unstable defined by the structural boundary
- convection reaches a steady state with a well defined dynamical boundary beyond the unaffected structural boundary.
- the chemical boundary slowly moves from the structural boundary to the dynamical boundary
- a steady state is reached when dynamical and chemical boundary point coincide

This simple picture is the motivation for the overshooting descriptions based on numerical simulations by Freytag et al. (1996) and Pratt et al. (2017) (see 2.2). Both studies define the speed and extent of the mixing around the Schwarzschild boundary based on the observed velocity profile.

We can now check whether this also holds in our simulations, by defining a series of different boundaries in the ImHrk simulation and following their temporal evolution.

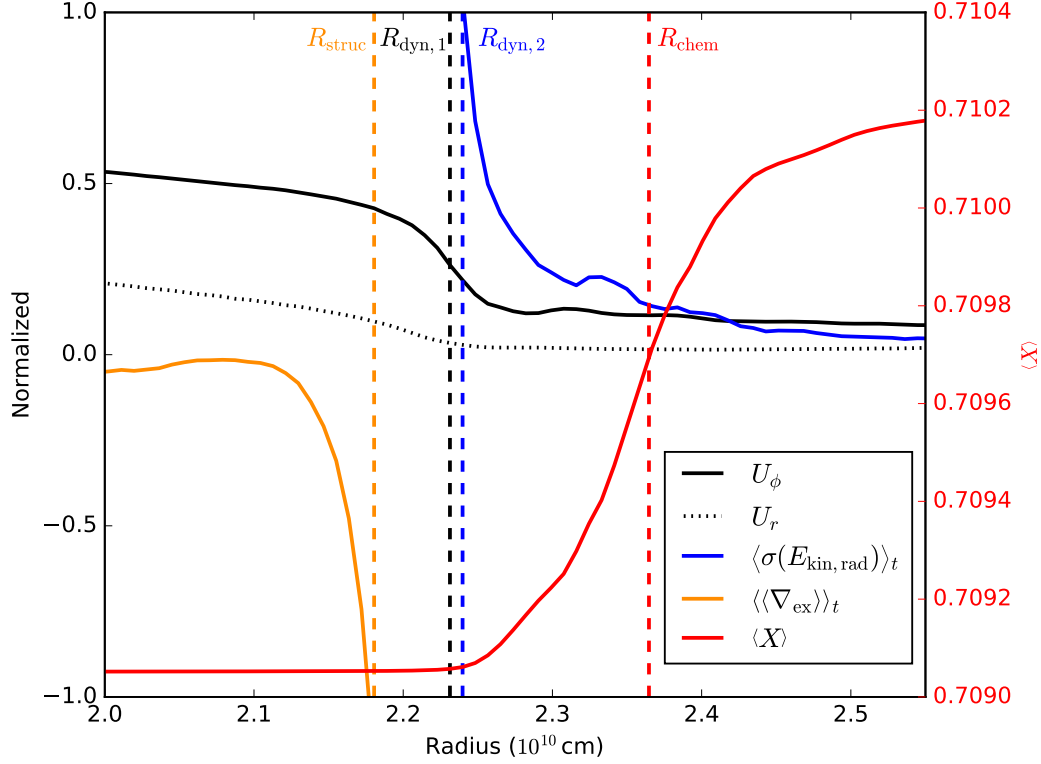


Figure 4.5: Typical spherically averaged profiles around the convective boundary. The quantities U_r , U_ϕ , $\langle \sigma(E_{\text{kin},U_r}) \rangle_t$, and $\langle \langle \nabla_{\text{ex}} \rangle \rangle_t$ are normalized and time averaged between 1.82 and $2.06 \cdot 10^8$ s using 100 plotfiles. Details on the normalization of each curve can be found in the text. The spherically averaged hydrogen mass fraction profile $\langle X \rangle$ is taken from the output file at $2.06 \cdot 10^8$ s. Dashed vertical lines mark the respective convective boundary as defined in 4.2.

The initial chemical boundary can easily be defined as the mid point of the composition discontinuity. Since the discontinuity is slightly smoothed out over time, we define the mid point over an extended radial zone around the initial discontinuity. Taking the minimal (X_{min}) and maximum (X_{max}) hydrogen mass fraction inside the (initial) convective region and around it, the chemical boundary R_{chem} can be defined as

$$R_{\text{chem}} = R \left(X = \frac{X_{\text{min}} + X_{\text{max}}}{2} \right) \quad (4.3)$$

where X_{min} and X_{max} are determined between 0.5 and $3.5 \cdot 10^{10}$ cm.

Due to the low time variability of the spherically averaged hydrogen mass fractions $\langle X \rangle$ we compute this quantity for each individual output file, which increases the

time resolution of the time evolution shown in Fig. 4.6. Meakin & Arnett (2007) and Cristini et al. (2017, 2019) used as similar definition of the boundary to determine the growth rate of a convective zone.

One can think of many ways to define a boundary based on the velocity field. One could use the time averaged radial velocity profiles $U_r = \langle \langle U_r \rangle \rangle_t$, as these are responsible for transporting matter into the convective zone, or transversal velocities $U_\phi = \langle \langle U_\phi \rangle \rangle_t$ as they tend to increase towards the boundary. One can also look at the kinetic energy and the (radial) flux of kinetic energy.

In order to reduce the influence of statistical fluctuations, we computed time averaged profiles with a moving average over 100 output files, which corresponds to ≈ 0.5 yr or 30 convective turnovers.

As it turns out, the radial velocities are not the ideal quantity to look at, because the radially outward flow is already starting to turn around long before the convective boundary is reached. In Fig. 4.5 the curves for U_ϕ as well as for U_r are normalized by the maximum value of U_ϕ . From this we can see that U_r is smaller than U_ϕ at the convective boundary and the convective boundary does not show any particularly strong feature in the U_r profile. The U_ϕ profile, on the other hand, shows a rather steep decline near the boundary, which can be used to define a boundary location. Following Jones et al. (2017) we use the location of the steepest gradient in the U_ϕ profile to set the boundary location $R_{\text{dyn},1}$ (dashed vertical lines in Fig. 4.5).

Pratt et al. (2017); Edelmann et al. (2019) define the dynamical boundary based on single plumes under the assumption that the farthest mixing events will also reflect the maximal extent of the overshooting region. Because averaged profiles are not sensitive to short term changes, rare deep mixing events are not fully captured by $R_{\text{dyn},1}$. To overcome this problem we use another measure for the dynamical boundary based on the time averaged standard deviation of radial kinetic energy flux $\langle \sigma(E_{\text{kin},U_r}) \rangle_t$. The combined variability of a quantity x in a set of N output files is defined as

$$\langle \sigma(x) \rangle_t = \left[\frac{\sum_{i=0}^N \sigma_i(x) \left[\langle x_i \rangle - \overline{\langle x \rangle} \right]^2}{N} \right]^{1/2}, \quad (4.4)$$

where $\langle x_i \rangle$ represents the horizontally averaged profile of quantity x in each individual output file i , and $\sigma_i(x)$ is the standard deviation of that average. $\overline{\langle x \rangle} = \frac{1}{N} \sum_{i=0}^N \langle x_i \rangle$ is the mean of all $\langle x_i \rangle$ included in the averaging window. $\langle \sigma(E_{\text{kin},U_r}) \rangle_t$ has larger contributions from rare events than the averaged values themselves.

$\langle \sigma(E_{\text{kin},U_r}) \rangle_t$ drops by several orders of magnitude as the convective boundary is approached. We use this to define our second dynamical boundary $R_{\text{dyn},2}$ as the point where $\langle \sigma(E_{\text{kin},U_r}) \rangle_t$ has dropped to 0.1% of its maximum value. In Fig. 4.5 we increase the visibility by normalizing $\langle \sigma(E_{\text{kin},U_r}) \rangle_t$ to a value of 10^{30} , which

corresponds to $\approx 0.1\%$ of its maximum value.

This is a similar approach as in Brummell et al. (2002); Rogers et al. (2006), who defined the convective boundary as the point where the kinetic energy drops to 1%, respectively 5% of its peak value.

The structural boundary R_{struc} is taken from the Schwarzschild criterion as the point beyond which the temperature gradient excess $\nabla_{\text{ex}} = \nabla - \nabla_{\text{ad}}$ is smaller than a certain value for all $R > R_{\text{struc}}$. The stability criterion obviously would suggest that the point with $\nabla_{\text{ex}} < 0$ should be used as the boundary, but as it turns out a large fraction inside the obviously convective zone constantly has $\nabla_{\text{ex}} < 0$. This subadiabaticity is very small, being of the order of 10^{-5} and is within the uncertainty limit of our ∇_{ex} (see 4.6 for a discussion of the uncertainty). We therefore chose $\nabla_{\text{ex}} < -2 \cdot 10^{-4}$ to reduce the influence on the uncertainty. Additionally we use the time average $\langle \cdot \rangle_t$ of the spherically averaged $\langle \nabla_{\text{ex}} \rangle$ to suppress temporal fluctuations as well.

Fig. 4.6 shows how the different boundaries evolve during the ImHrk simulation. The width of the radial bins in our analysis is typically $2 \cdot 10^8$ cm, in agreement with our grid resolution. In Fig. 4.6 the effect of the binning causes the step like evolution of the boundaries. Most of the boundaries stay at a constant radius for most of the simulation time. $R_{\text{dyn},1}$ and $R_{\text{dyn},2}$ show a small excess in the beginning of the simulation. This is the point where the averaging window is still capturing the initial transient discussed in 4.1.

R_{chem} is changing the most, showing that there is a lot of mixing going on.

R_{struc} is retreating during the initial transient from its original position at $2.25 \cdot 10^{10}$ cm, due to the adjustment of ∇ to the changes in the composition gradient. The sudden outward shift of R_{struc} at $0.2 \cdot 10^8$ s is an artefact of the mixing, where the temperature gradient in the initial stable layer approaches the adiabatic temperature gradient. This effect reduces over time as the chemical boundary moves outwards. 4.6 will discuss the influence of the composition on the temperature gradients in more detail. After that R_{struc} stays constant for the rest of the simulation as it is expected from the naive picture above.

The order of R_{struc} and R_{dyn} is as expected from the naive picture. The driving of convection is happening within R_{struc} . R_{dyn} on the other hand also captures the penetration into the stable layer. As expected from energy arguments (see 2.2) the penetration region in our simulations is rather small. R_{dyn} is only $6 \cdot 10^8$ cm further out than R_{struc} corresponding to $0.04H_p$. R_{chem} is located much further out than the other boundaries and even keeps moving further away. This does not fit the mixing picture described above, where we would expect that mixing stops at the dynamical boundary. There is obviously a process that leads to mixing into much

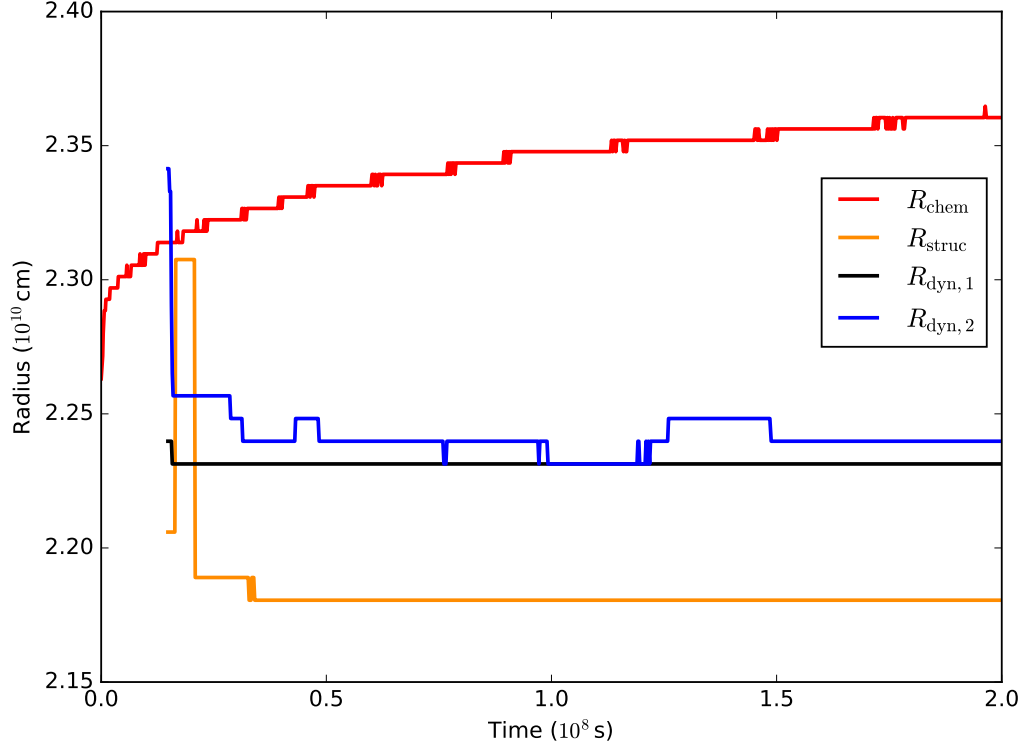


Figure 4.6: Temporal evolution of the different convective boundaries as defined in 4.2.

farther layers. $R_{\text{dyn},2}$ is giving a hint towards that. $R_{\text{dyn},2}$ is in general larger than $R_{\text{dyn},1}$ confirming our suspicion that there are mixing events reaching beyond $R_{\text{dyn},1}$ that are not captured by the average. Nevertheless $R_{\text{dyn},2}$ is still much smaller than R_{chem} . In 4.4 we will see that diffusive mixing is the key factor to explain this discrepancy.

4.3 Internal Gravity Waves

Similar to the stable atmosphere problem in 3.5.3, stellar models also have an IGW cavity (see Fig. 2.2). Our simulations therefore suffer from the same problem, where numerical IGWs pile up inside the cavity and create an unphysical convective region. We can clearly see the effect in the velocity profile of the ImMrk simulation in Fig. 4.4, where the velocity in the stable region between ≈ 3 and $4 \cdot 10^{10}$ cm is almost as

large as in the convective region. In 3.5.3 we showed that the RK time integrator can reduce these velocities significantly and in fact, when we repeat ImMrk with the same resolution but using the PC integrator, we find that the velocity in the stable region is actually larger than in the CZ.

The higher resolution case ImHrk does not show exceptionally large velocities in the stable layer, indicating that higher spatial resolution is able to reduce the artificial velocities as well. Nevertheless the velocity field in the stable region of ImHrk is dominated by IGWs. We can see this from Fig. 4.5 where $U_\phi > U_r$ outside of R_{dyn} , a clear sign for IGWs.

While the RK time integration in combination with a sufficiently high spatial resolution does successfully prevent the creation of unrealistically large velocities in the stable region, it is unclear what actually causes the problem. Here we want to analyse the cause in more detail.

In 3.2 we defined τ_{brunt} as the typical timescale of IGWs. From 2.2 we can determine that this would suggest that IGWs change on a timescale of ≈ 500 s. The timesteps in ImMrk are half of that. If τ_{brunt} is the numerically important timescale we would expect that IGWs in ImMrk are not well resolved. On the other hand, we would also expect that no numerical instability occurs. The quick growth of the velocities in the stable layer, however, suggests that we are dealing with an unstable situation here. One can also argue that τ_{brunt} is not the relevant timescale for numerical simulations, because we also determined in 3.2 that the CFL criterion is based on the speed of signal propagation. The signal propagation of IGWs, however, is not determined by their frequency but by their group velocity $v_{\text{group}} = \partial\omega/\partial k$. From Eq. 2.15 we can see that IGWs have $v_{\text{group}} \leq v_{\text{ph}}$. This allows us to use the phase velocity $v_{\text{ph}} = \omega/k$ instead of v_{group} as an even tighter limit to the speed of signal propagation. The maximum phase velocity $v_{\text{ph,max}}$ can then be computed easily as $v_{\text{ph,max}} = \lambda N/2\pi$. The signal speed is hence limited by N and the wavelength λ of an IGW. Analogous to sound waves, we can then write a new timestep criterion based on the generalized CFL criterion 3.14 that needs to be fulfilled in order to resolve IGWs properly.

$$\Delta t < \frac{\Delta x 2\pi}{\lambda N}, \quad (4.5)$$

Assuming that IGWs have wavelengths up to 1 pressure scale height one ends up with timesteps that are only a factor $\approx 5 - 10$ larger than the explicit timesteps based on 3.15.

Fully resolving IGWs in time is therefore computationally too expensive for the long term simulations we need in order to estimate the extent of the mixed region.

The maximum frequency of IGWs allowed by N is of the order of several mHz,

while observations show that the dominant component of IGWs is in the low frequency regime up to several tens of μHz (Bowman et al., 2019). Aerts et al. (2018) also argue that angular momentum transport by IGWs is dominated by low frequency waves as well. Aerts et al. (2010) also observed g-mode periods between 0.5 - 3 days, corresponding to $4 - 20\mu\text{Hz}$

Theoretical wave spectra of IGWs (Lecoanet et al., 2014) also predict IGW frequencies predominantly below the convective turnover frequency (which is well resolved in our simulations). While this last statement is challenged by the simulations of Edelmann et al. (2019) who found a non negligible contribution from frequencies above the turnover frequency, their wave frequencies still remain far below the mHz limit.

We therefore decided to not resolve high frequency waves in time and use the velocity based timestep criterion 3.25 instead. In our simulations with high resolution this corresponds to timesteps of 100 s. We therefore expect to properly resolve IGWs with a frequency of up to $20\mu\text{Hz}$.

According to linear theory IGWs are exponentially damped inside convective zones, which means that we do not expect any influence of the unresolved IGWs on the convective flow itself. The influence at the convective boundary, especially on the mixing, on the other hand, has to be tested. We therefore performed the simulation ImHpcIGW, that uses timesteps based on Eq. 4.5 with a wavelength of 1 pressure scale height. For efficiency reasons we did not use the RK integrator in this run, but we already showed that this has no influence on the results.

As expected the average velocity in the CZ does not depend on the timestep criterion (see Fig. 4.1). As already described in 4.1 the profiles of ImHrk and ImHpcIGW in Fig. 4.4 also match perfectly. In 4.4 we will see that this also true for the mixing behaviour at the convective boundary, indicating that the high frequency IGWs do not significantly contribute to the mixing.

Nevertheless we do see IGWs in our simulations. In Fig. 4.7 we show the temperature perturbations $T' = T - \langle T \rangle$, where $\langle T \rangle$ is the spherically averaged temperature. To increase the visibility of the IGW pattern we interpolated the data on the Cartesian grid onto a polar grid (r, ϕ) . T' shows a regular flat pattern in the stable region. Rogers et al. (2013) showed that an eddy dominated flow, will produce such a flat structure of IGWs, which is consistent with our results where the convective flow is dominated by large vortices (= eddies). This is a pure effect of the reduced dimensionality of our simulations. We therefore do not expect this wave pattern to be a good representation of nature and therefore will not analyse the IGW frequency spectrum in detail.

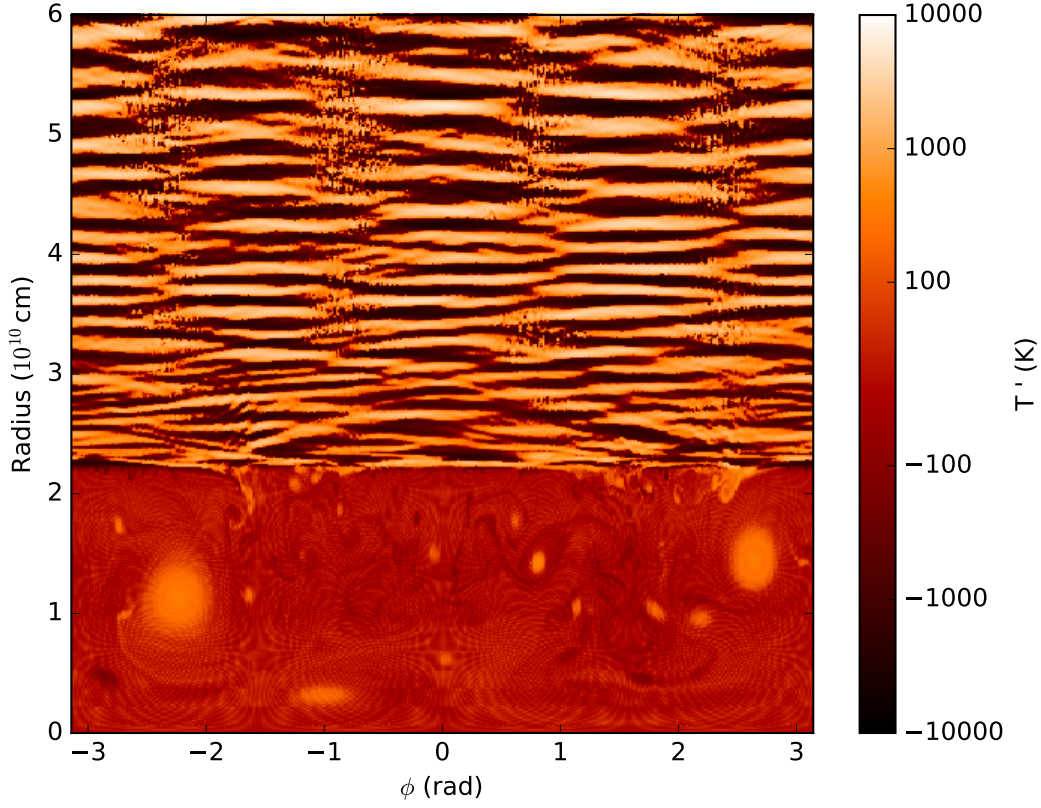


Figure 4.7: Fluctuations of the temperature from its spherically averaged value in the ImHrk simulation mapped on a polar grid (r, ϕ) , after $8 \cdot 10^7$ s.

4.4 Overshooting Calibration

We are mainly interested in the mixing around the convective boundary. In 2.2 we described the different processes that lead to chemical mixing at the convective boundary. Here we will analyse which process dominates and which size we expect for the homogeneously mixed overshooting layer in 1D models. We will do this by calibrating a 1D overshooting parameter.

Before we analyse the long term mixing, we first have to look at the influence of the initial transient and the different numerical setups. In order to quantify the mixing of matter with higher hydrogen abundance than in the CZ across the convective boundary we show in the top panel of Fig. 4.8 the change in hydrogen mass $M_X - M_{X_0}$ inside the convective core as a function of time, defined by the mass coordinate of the initial Schwarzschild boundary, where M_{X_0} is the value at $t = 0$.

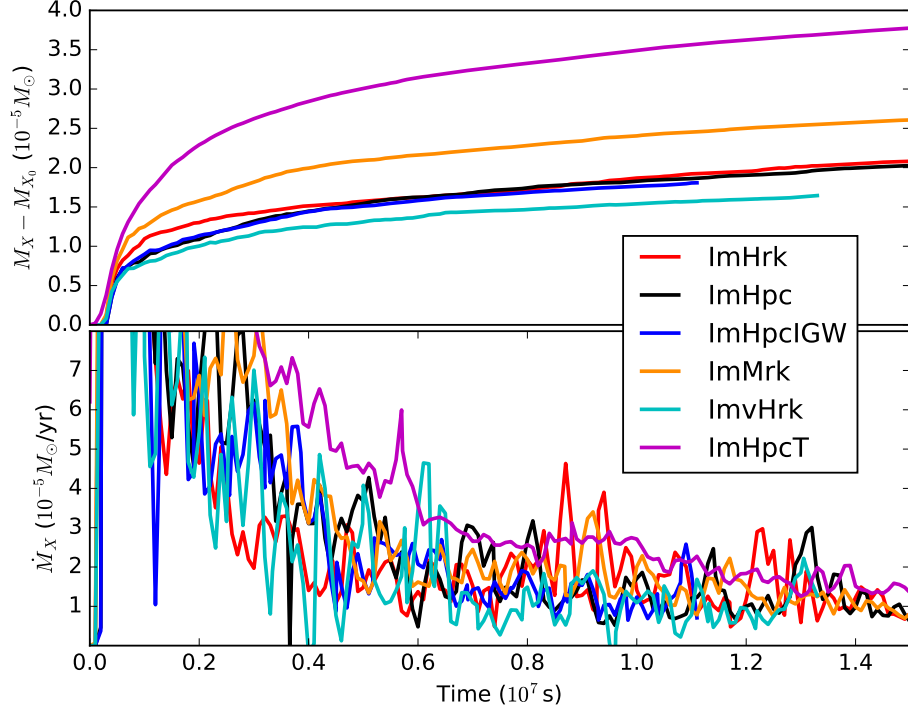


Figure 4.8: Top panel shows the change in hydrogen mass inside of the initial convective core for the $3.5M_{\odot}$ star simulations. The bottom panel shows the time derivative of this quantity.

We see that in all simulations there occurs rapid mixing in the very beginning of the simulation, which then slows down with time. This is due to the initial transient as described in 4.1. The varying strength and length of the transient as seen in Fig. 4.1 is also the reason for the varying amount of mixing at the beginning of the different simulations (see Fig. 4.8). The simulations ImMrk and ImHpcT have extended transients (see velocity evolution in Fig. 4.1) and therefore mix more matter initially. The very high resolution run ImvHrk, on the other hand, has the shortest transient and consequently also shows the least mixing at the beginning of the simulation. Once the initial transient is decayed, all simulations evolve roughly in a similar way. This becomes evident when we look at the time derivative of the hydrogen mass evolution in the bottom panel of Fig. 4.8, where all simulations show the same mixing speed at later times. We therefore should only look at the mixing after the initial transient and a steady state has been reached.

This again confirms that the RK and PC integrator produce similar results and that our high resolution runs with 1024^2 cells are numerically converged. In addition to that we can also see that there is essentially no difference between the ImHrk and the ImHpcIGW simulation, suggesting that the high frequency IGWs that are only properly resolved in ImHpcIGW do not have a significant influence on the mixing. Surprisingly we also see convergence with the ImHpcT run, where one would expect a higher mixing speed due to the overall larger velocities. This is an indication that the velocity magnitude is not the limiting factor for the mixing speed. 4.5 will address this point again.

In 5.1 we will see that the initial mixing behaviour is a problem in 3D simulations, because there the initial structure is altered significantly and the farther evolution is influenced.

The mixing in the steady state is dominated by the interaction of the vortices with the convective boundary. In the top panels of Fig. 4.3 we display a snapshot of the ImHrk simulation showing its velocity magnitude and the radial perturbation $X' = X - \langle X \rangle$ of the hydrogen abundance in the left and right panel, respectively. From the perturbation in the hydrogen abundance we can see that the main cause for mixing is shear created by the vortices as they move along the convective boundary. The shear mixing can be separated into two main effects. A single vortex that moves along the boundary creates Kelvin-Helmholtz instabilities in its wake. We can see this in the top right panel of Fig. 4.3 in the bottom right and the upper left corner at the convective boundary (black dashed line) as blobs that detach from the convective boundary. The large inflow on the left side is a combined effect of two counter rotating vortices. When the two vortices interact with the boundary at roughly the same time, they launch surface waves running in opposite direction. These waves then collide and break, creating a significant amount of mixing. This suggests that mixing is not a strictly continuous process, but rather a combination of single mixing events. Each event will only mix until a certain distance to the convective boundary, depending on how strong the event was and where it occurred. Another form of single mixing events are plumes that penetrate the convective boundary and turn around due to buoyancy. Pratt et al. (2017) analysed these plume events for mixing around a convective envelope and found that only a small number of events are responsible for the deepest mixing. On the basis of this Extreme Value approach we develop here a calibration method for the 1D overshooting parameter.

We can calibrate an overshooting parameter by using several starting models, computed with different overshooting parameters and prepared as described in 3.6. We depict the procedure in Fig. 4.9, where we show the mixing in the form of penetrating plumes, but the idea is the same for all other mixing events with a fixed mixing depth.

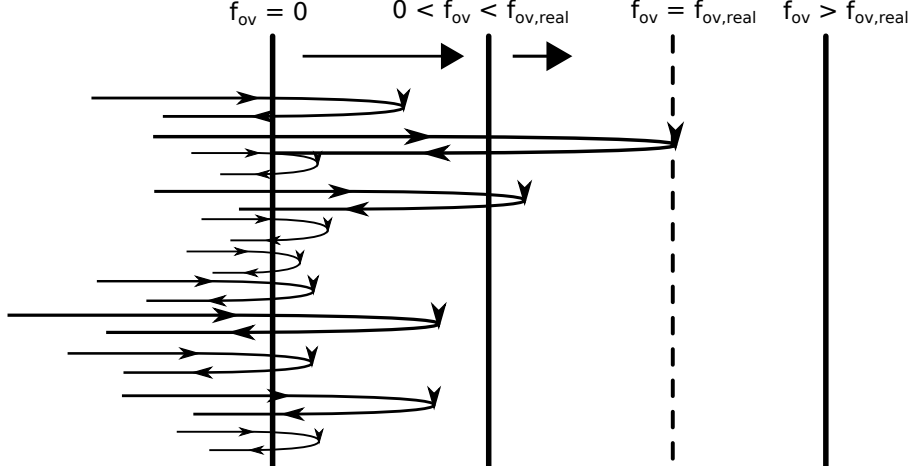


Figure 4.9: Schematics of the overshooting calibration, where vertical lines indicate the position of composition interfaces corresponding to the overshooting parameter given at the top.

Initial models without any overshooting will experience many mixing events that are able to transport hydrogen from the stable layer into the CZ, since R_{chem} and R_{struc} coincide in those models. As hydrogen is mixed into the CZ, the distance between R_{chem} and R_{struc} will increase and thus the hydrogen content in the CZ. Models with $f_{\text{ov}} > 0$ have a mixed core that is larger than the formal Schwarzschild boundary. Mixing events need to penetrate further into the radiative layer in order to reach hydrogen rich matter. Therefore less events will be able to mix matter into the core and R_{chem} moves slower.

A setup where the initial model was computed with a too large value of f_{ov} would result in a simulation, where no form of chemical mixing into the CZ would be noticeable. The ideal overshooting parameter $f_{\text{ov},\text{ideal}}$ is reached, when no mixing is noticeable any more, but for a model with $f_{\text{ov}} = f_{\text{ov},\text{ideal}} - \epsilon$, rare single events would still occur.

We performed simulations with $f_{\text{ov}} = 0$ (ImHrk), 0.01 (ImHrk-1), 0.02 (ImHrk-2) and 0.03 (ImHrk-3) to follow the evolution in f_{ov} space from low to large overshooting parameters. We also computed a model with the canonical value of $f_{\text{ov}} = 0.017$ (ImHrk-1.7) to have a higher sensitivity in the region where we expect the actual overshooting parameter.

The snapshots of the simulations ImHrk, ImHrk-1.7 and ImHrk-3 in Fig. 4.3 show that the velocity magnitude in the left panels looks qualitatively the same in all

simulations. Inside the formal Schwarzschild boundary (black dashed line) the velocity field is turbulent and dominated by two vortices. The absolute magnitude of the velocity is the same in these simulations, which is expected since they all have very similar heating terms. The dashed white circles in Fig. 4.3 denote the position of the composition interface in the initial model. In the ImHrk simulation this overlaps with the Schwarzschild boundary and is hence not shown. In the models with larger overshooting parameters, on the other hand, there is a noticeable gap. The ImHrk-3 panels in 4.3 show that between the Schwarzschild boundary and the mixed boundary no convective motion occurs. This is an indication that single plumes rarely penetrate the convective boundary and that looking at the composition is not enough to claim a growing CZ in our case.

The right panels in Fig. 4.3 give an indication of the mixing intensity of these models. In ImHrk (top panel) we see large perturbations throughout the CZ, showing that a substantial amount of hydrogen is mixed around in the core. Here plumes are not a largely contributing factor since the shear mixing events are much more frequent. In ImHrk-1.7 the mixing events have to bridge a gap to reach hydrogen rich matter hence we see that the CZ is predominantly homogeneous (white color in Fig. 4.3) and only small perturbations are visible. The gap between the turbulent flow and the composition discontinuity is even larger in the ImHrk-3 simulation (lower panels in Fig. 4.3). Consequently, no mixing event reaches regions with higher hydrogen content and the CZ remains completely homogeneous.

However, ImHrk-3 also exhibits large hydrogen perturbations around the chemical boundary. This shows that the composition boundary is smoothed out during the simulation. At the time of the snapshot shown in Fig. 4.3 the smoothing has already bridged half of the gap towards the Schwarzschild boundary. We will later see that this a diffusive process.

The second ring with increased perturbation is a feature of the starting models, which have an additional small discontinuity at the maximum extent of the convective core during the pre-main sequence evolution.

Due to our shallow hydrogen profiles we can directly see the influence of chemical mixing on the composition profiles. In the left panel of Fig. 4.10 we can clearly see that the spherically averaged hydrogen profile $\langle X \rangle$ in the ImHrk simulation moves significantly into the stable layer. Consequently the hydrogen content in the CZ increases.

With increasing f_{ov} the hydrogen profile changes less and less over the same simulation time. In the ImHrk-2 and ImHrk-3 simulations we almost perfectly retain the initial profile even after 130 and 70 convective turnover timescales, respectively. In the ImHrk-1.7 run small deviations are visible, where the profile got smeared out. The switch from an almost stable profiles in ImHrk-1.7 to a stable profile in ImHrk-2 in combination with the overall small (but non-zero) mixing rates are a clear

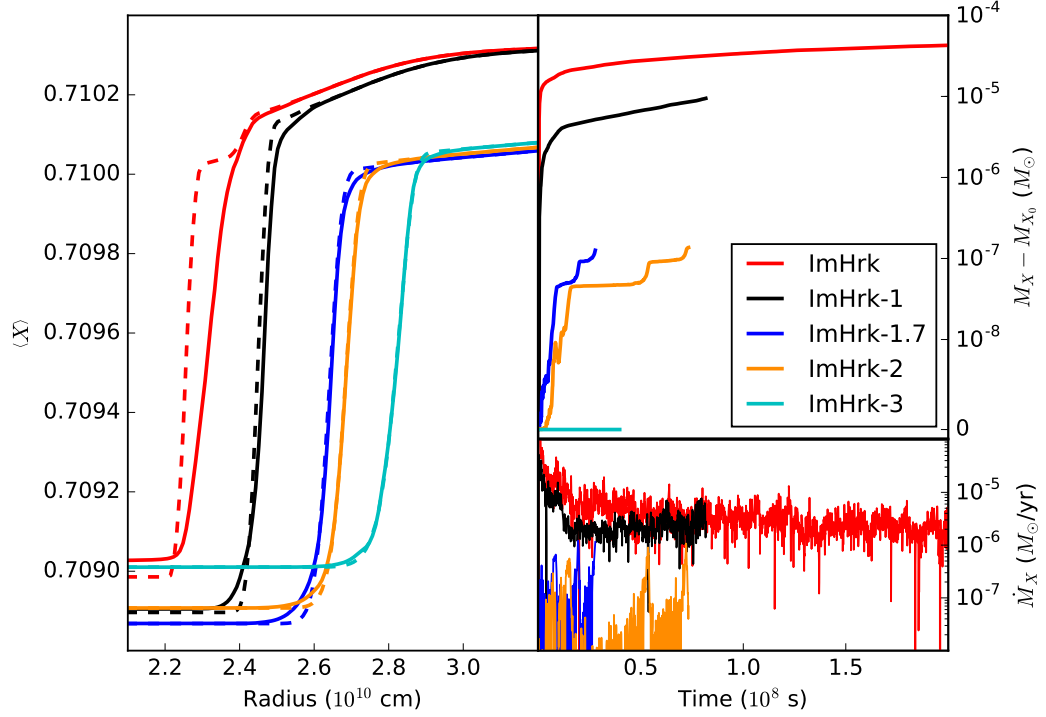


Figure 4.10: Left panel shows spherically averaged hydrogen mass fraction profiles of the $3.5M_{\odot}$ mass simulations, where dashed lines give initial profiles and solid lines show the profiles after $4 \cdot 10^7$ s. The right panels show the change in hydrogen mass in the CZ, with time analogous to 4.8.

indication that these simulations are close to give the real extent of the mixed region. Based on this we would expect that the overshooting parameter lies in the range $0.017 \lesssim f_{ov} \lesssim 0.02$.

Snapshots and single profiles, however, are not sufficient to follow the time evolution of mixing. In the right panels of Fig. 4.10 we therefore again follow $M_X - M_{X_0}$. From the top right panel of Fig. 4.10 it becomes clear that there are significant differences between the runs with different f_{ov} . Over the whole simulation ImHrk mixes a few $10^{-5}M_{\odot}$ of hydrogen into the convective core, while the ImHrk-2, only mixes about $10^{-7}M_{\odot}$, and ImHrk-3 does not mix any hydrogen at all during the simulation time. In the right bottom panel of Fig. 4.10 we show the derivative of the change in

Name	$M_{\text{CZ},i} (M_{\odot})$	$M_{\text{mixed},i} (M_{\odot})$	Mixing Rate (M_{\odot}/yr)	Ri_b
ImHrk	0.69	0.69	$4.0 \cdot 10^{-6}$	627
ImHrk-1	0.72	0.83	$2.5 \cdot 10^{-6}$	936
ImHrk-1.7	0.78	1.00	$1.5 \cdot 10^{-7}$	1193
ImHrk-2	0.78	1.02	$6.4 \cdot 10^{-8}$	1580
ImHrk-3	0.78	1.14	$2.5 \cdot 10^{-16}$	2236

Table 4.2: Results of our analysis of the mixing processes in the $3.5M_{\odot}$ models with different overshooting parameters. The second and third two columns give the initial mass of the CZ and the homogeneously mixed region, respectively. The fourth column gives the mixing rates time averaged for $t > 10^7$ s. The last column shows the bulk Richardson number Ri_b , i.e., the stiffness of the boundary.

hydrogen mass \dot{M}_X as an indication for the mixing speed, and in Table 4.2 we give time averaged mixing rates for each simulation based on this time derivative. In order to avoid influences from the initial transient we decided to only include datapoints with $t > 10^7$ s into the average. The ImHrk run produces an almost constant, but slowly declining, mixing speed. The mixing rate is on average $4 \cdot 10^{-6} M_{\odot}/\text{yr}$, i.e., entraining all the mass in the stable layer ($\approx 2.8 M_{\odot}$) would take $7 \cdot 10^5$ yr. This corresponds to a few thermal timescales and is obviously an unrealistically large value. The ImHrk-2 run gives on average a growth rate of $6 \cdot 10^{-8} M_{\odot}/\text{yr}$, almost two orders of magnitude smaller. While this is still fast enough to homogenise the whole star during the main sequence lifetime of the order of 10^8 yr, it also is slow enough that the stellar structure can react to these changes before the whole star is mixed. One can speculate that the possibility of structural changes might stop the growth eventually.

From the mixing curves of ImHrk-1.7 and ImHrk-2 in Fig. 4.10 we can also see that our picture of single mixing events is a valid approach. Single bursts of mixing are followed by a prolonged quiescent time, indicating that rare deep penetrating plumes are responsible for most of the mixing in these models. We can also notice that the time between mixing events in ImHrk-2 is significantly longer than in ImHrk-1.7, because the plumes have to penetrate even farther to reach hydrogen rich matter in the latter run.

In 4.2 we raised the question which kind of event can bridge the gap between the dynamical boundary and the chemical boundary. The sudden mixing events in ImHrk-2 give us the opportunity to look at one isolated event. We therefore increased the number of plotfiles in ImHrk-2 between 4.9 and $5.7 \cdot 10^7$ s by a factor of 100. With this high number of output file, we indeed can identify single plumes

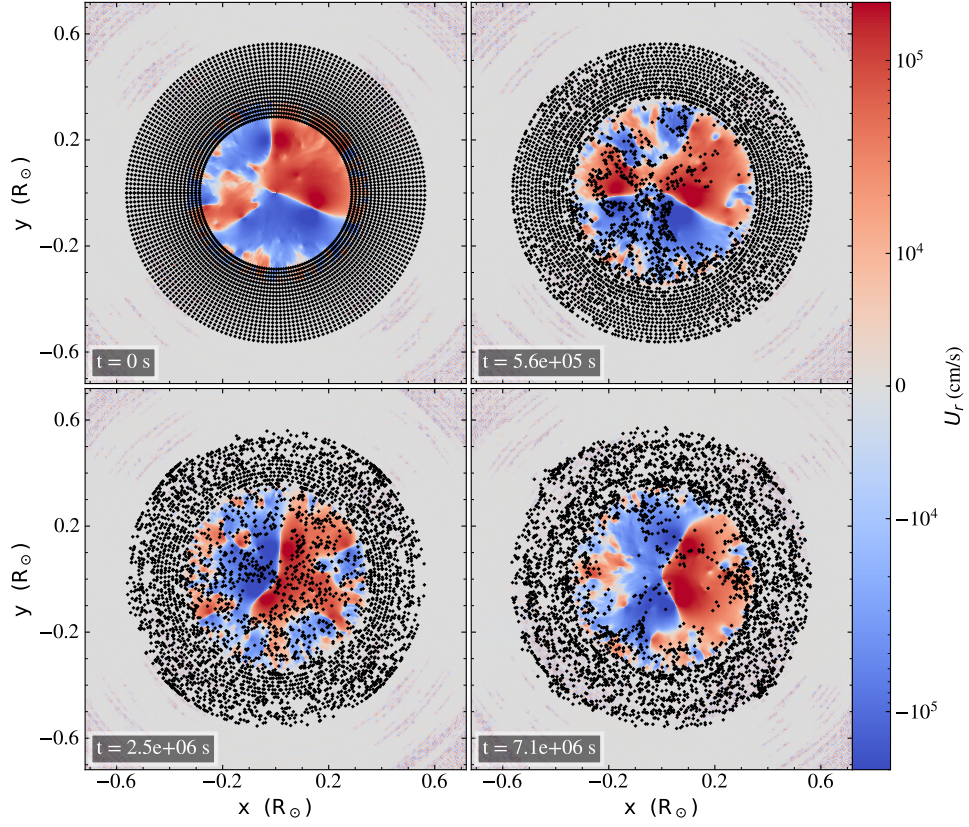


Figure 4.11: Snapshots of radial velocity of the ImHrk-2 simulation, over-plotted are the positions of tracer particles (black dots). The elapsed time since the initialisation of the tracer particles at 1.55 yr is given in the lower left corner of each panel.

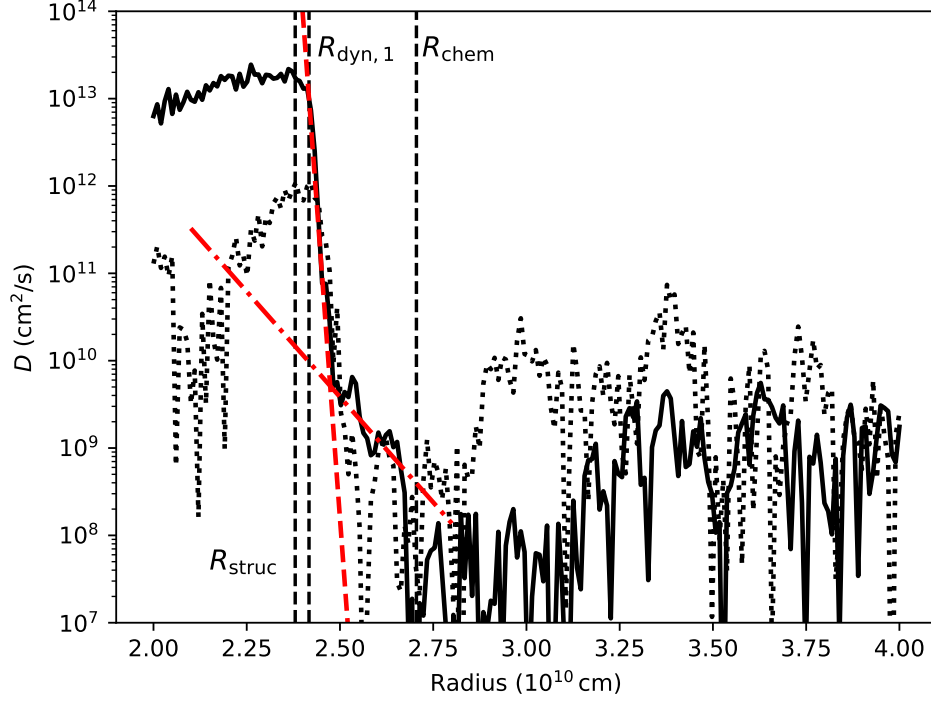


Figure 4.12: Diffusion coefficients around the convective boundary determined from the ImHrk-2 simulation. The solid line uses a time interval of $2.5 \cdot 10^6$ s and the dotted line $7 \cdot 10^6$ s. The red dashed lines shows an overshooting law with $f_{ov} = 0.01$, while the red dash dotted line uses $f_{ov} = 0.06$

penetrating unusually deep into the stable layer right around the time where we see the spike in the mixing at $5.2 \cdot 10^7$ s (see Fig. 4.10). However, none of these events penetrates nearly far enough to reach the steep composition interface that is located $0.1H_p$ outside of the R_{chem} . At most we see mixing events that extend $0.05H_p$ into the stable layer.

The missing link to cover that gap are diffusive processes, which are not captured by the picture of single mixing events. As discussed in Rogers & McElwaine (2017) mixing by IGWs can be interpreted as a diffusive process, but also numerical diffusion can contribute in regions with sharp gradients.

From first principles we would expect that diffusive processes result in a slow continuous mixing across the convective boundary. This is contradicting the bottom right panel of 4.10 which clearly shows a very peaked mixing history for the ImHrk-1.7

and ImHrk-2 simulations. However, the timescales for diffusive processes are usually much larger than the ones for convective motions. Under this assumption we can interpret the data in the following way:

Diffusion will slowly smooth out the composition profile and will bring matter, with an increased hydrogen mass fraction, closer to the convective boundary. Before diffusion has time to move the matter across the boundary deep penetrating mixing events suck the low end tail of the smeared out profile into the CZ, altering the composition profile locally in the process. Diffusion and horizontal motion will then try to restore the low end tail before it is again mixed into the CZ by another plume. In the end we reach a balance between the diffusion, providing hydrogen rich matter, and the actual mixing over the boundary by plumes.

Due to the dense output in the ImHrk-2 run we can analyse the diffusive mixing by adding tracer particles in post-processing. We tracked the position of 40000 particles over a time of $7.1 \cdot 10^6$ s around the mixing event at $5.2 \cdot 10^7$ s. We use the velocity information of each output file to follow the motion of the particles, where we assume that particles travel at a constant speed in the time interval between two consecutive output files. The tracer particles were placed on a regular polar grid around the convective boundary between 2.0 and $4.0 \cdot 10^{10}$ cm. The innermost tracer particles are part of the CZ, while most of the particles are placed in the stable layer. The initial positions can be seen in the upper left panel of Fig. 4.11.

We can then calculate diffusion coefficients D from the radial displacement Δr of the particles after some time Δt as $D = (\Delta r)^2 / \Delta t$.

The resulting diffusion coefficients are shown in Fig. 4.12. We show two values for D , using the same particles but following them over different time intervals Δt . The solid line shows D calculated after $2.5 \cdot 10^6$ s, while the dotted line uses $\Delta t = 7.1 \cdot 10^6$ s. The vertical dashed lines indicate the convective boundaries as defined in 4.2.

Rogers & McElwaine (2017) did the same exercise for their 2D simulation of a $3.0 M_{\odot}$ mass star using data of $2.5 \cdot 10^6$ s of simulation time to determine D . Comparing Fig. 4.12 with their Fig. 2 we find a perfect agreement in D when we use the same Δt . Inside the CZ D is orders of magnitude larger than outside the CZ, indicating a very efficient mixing. This is also true for the small layer between $R_{\text{dyn},1}$ and R_{struc} .

In Fig. 4.11 we display the positions of the tracer particles (only 4000 are shown) during the mixing event. We can see that the particles inside the CZ get quickly distributed across the whole CZ. After placing the particles on the grid at 1.55 yr it only takes $5 \cdot 10^5$ s for some particles to reach the centre of the star (upper right panel). After $2.5 \cdot 10^6$ s (lower left panel) the particles are perfectly mixed throughout the whole CZ. This corresponds to a diffusion coefficient of the order of $10^{13} \text{ cm}^2/\text{s}$ throughout the CZ in perfect agreement with estimates based on MLT.

Outside of $R_{\text{dyn},1}$ the diffusion coefficients quickly drop by 4 orders of magnitude over a distance of less than 10^9 cm. This drop can be fitted by a diffusive overshooting model according to Eq. 2.12 with $f_{ov} = 0.01$ (red dashed line in Fig. 4.12), indicating that the empirical estimate $f_{ov} = 0.017$ is overestimating the actual amount of diffusion. However, further out D is still dropping but at a smaller rate. This part of the curve can be approximated by a diffusive overshooting with $f_{ov} = 0.06$ (red dash dotted line in Fig. 4.12), which is much larger than the empirical estimate. Approximating the diffusion coefficient as two connected exponentially decaying functions corresponds to a diffusive overshooting model proposed by Herwig et al. (2007) based on 2D and 3D simulations of convection in a He shell during a flash event on the asymptotic giant branch. On the main sequence we expect that a single exponential function still provides an appropriate estimate for the extent of the mixed region, because the diffusion timescales are so much smaller than the evolutionary timescales. Thus, the mixing can be assumed to be almost instantaneous. The overshooting parameter of the single exponential then has to be a specific value in the range $0.01 < f_{ov} < 0.06$, which provides the same size of the mixed region as the second shallower exponential. However, when the evolutionary timescale becomes comparable to the diffusion timescale, it is necessary to include both exponentials into the model to get the right amount of mixing.

The minimum D is reached at the location of R_{chem} . At this point D is roughly 5 – 6 orders of magnitude lower than inside the CZ.

Outside of R_{chem} the diffusion coefficients start to increase again due to the increase in amplitude of the IGWs. Deep in the stable layer, shortly before we start damping our velocities, we find $D \approx 10^9 \text{ cm}^2/\text{s}$.

From Fig. 4.11 we see that throughout the stable layer the initial symmetric angular distribution of the tracer particles remains initially intact (see upper right panel). At later times, however, the particle order gets noticeably distorted due to the considerably larger lateral velocities in the stable layer. This noticeable motion does not show up in our diffusion coefficients since we are only analysing the radial displacement. Yet it is the key features to provide an angularly homogenized hydrogen profile after a mixing event has removed hydrogen locally. Without lateral motion different deep penetrating mixing events might reach regions with different hydrogen contents depending on the number of events that previously have happened at the same location. Hence, the large lateral motion is necessary in order to establish a balance between the diffusive mixing and the single mixing events.

Including the mixing event of ImHrk-2 at $5.2 \cdot 10^7$ s into the tracer particle analysis, changes the results slightly (dotted line in 4.12).

Most noticeably the diffusion coefficient inside the CZ is now ≈ 2 orders of magnitude smaller than before.

This is partially due to the limited size of the CZ, which restricts the maximal radial

displacement of tracer particles within the CZ. Once the particles are randomly distributed inside the CZ the mean radial displacement will no longer grow. Hence, D is expected to decline as $1/t$. However, we see a bigger drop than that. The remaining difference can be explained by overshooting of particles at the convective boundary:

During the time interval of the tracer particle analysis the output files in ImHrk-2 are written every 1000s, i.e., there are ≈ 10 computational timesteps between each output file. If the direction of a fluid element in the simulation changes very quickly within a few timesteps we therefore cannot capture that in post-processing. The particle will overshoot its actual path and might end up in a different region that follows another flow structure. Such situations are especially common at the convective boundary. Here, the direction of the flow changes very quickly as plumes approach the boundary. Moreover, particles that overshoot can end up in the stable layer. In the worst case one grid cell makes the difference between CZ and stable layer. A particle with a velocity of 10^5 cm/s will move across one cell width between two snapshots. This velocity is not a uncommon one, since the standard deviation in the velocity is on a similar level as the velocity magnitude.

A similar process where particles move from the stable layer into the CZ is much less likely as the velocities there tend to be smaller and also the flow direction is predominantly tangential to the boundary. We can also see this in 4.11 where the colors indicate radial velocities U_r . Outside of the CZ U_r is orders of magnitude smaller than inside the CZ. The motion in radial direction in the stable layer is then well resolved by our post-processing tracer particles.

As time progresses more and more particles in the CZ will get into such a situation. Counter intuitively the CZ will, therefore, actually loose particles over time even though hydrogen is mixed into the CZ. This is very noticeable when we look at the bottom right panel of Fig. 4.11, where we see much less particles inside the CZ than in the other panels.

Since we initially only place particles in the outer regions of the CZ, the particles that are now stuck at the outside of the boundary remain relatively close to their original position. The diffusion coefficient, hence, is underestimated by this selection effect.

Further out, the influence of the longer timespan of the analysis is less drastic. In the intermediate region between $R_{\text{dyn},1}$ and R_{chem} the two different curves in Fig. 4.12 agree perfectly well. The resulting values of D seem to be converged in that region. Outside of R_{chem} the diffusion coefficients increase during the mixing event. A mixing event that penetrates deep enough to reach hydrogen rich matter needs to have a large velocity. It will therefore also launch IGWs with an increased amplitude. Shortly after the mixing event we would therefore expect D to rise in the stable layer. Beyond $3.5 \cdot 10^{10}$ cm the dotted and solid line in Fig. 4.12 again agree fairly well,

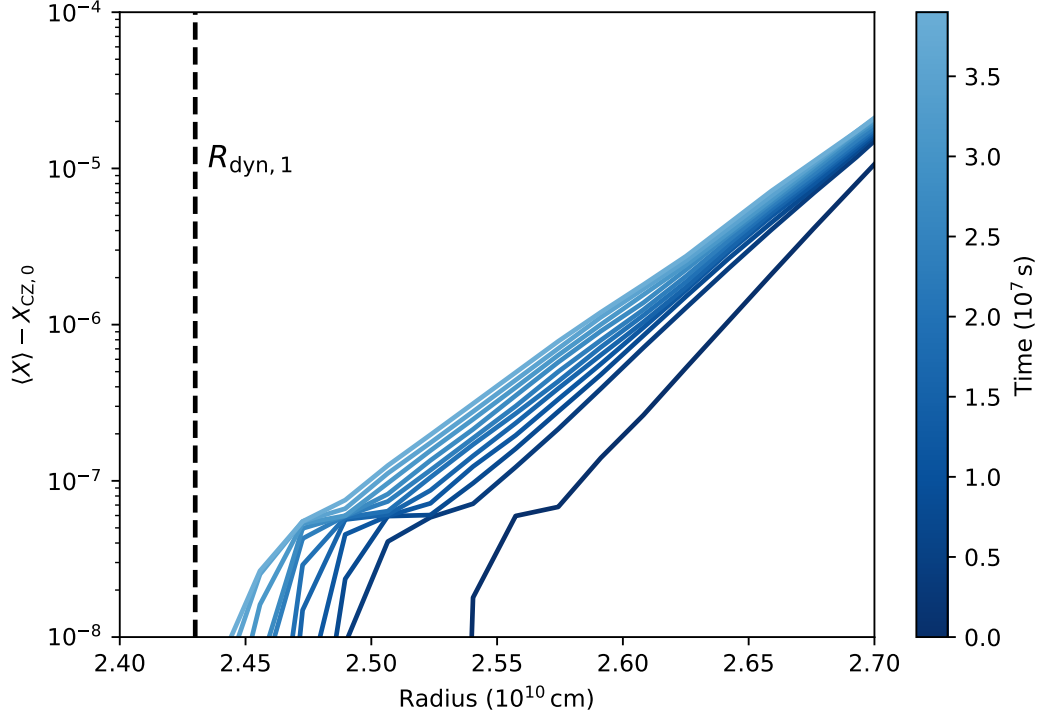


Figure 4.13: Spherically averaged hydrogen mass fraction profiles of several snapshots of the ImHrk-3 simulation. The hydrogen mass fraction in the CZ $X_{CZ,0}$ of the initial model is subtracted in order to visually enhance the mixing effects at the composition interface. The profiles shown are equally spaced in time and coloured, respectively. We also marked $R_{\text{dyn},1}$ as a vertical dashed line.

indicating that the strong IGW from the mixing event has not reached this area yet.

The rather robust results for D in the stable layer allow us to look at the timescales of diffusive mixing by IGWs.

At the composition interface we find that typically $D = 10^8 \text{ cm}^2/\text{s}$. Over the whole simulation time of ImHrk-2 this corresponds to a typical mixing distance of $\lesssim 10^8 \text{ cm}$. However, the distance between the hydrogen interface and the dynamical boundary is more than one order of magnitude larger than that. Yet mixing already sets in after $3 \cdot 10^5 \text{ s}$, i.e., the mixing process that brings the composition interface in contact with R_{dyn} cannot be IGW dominated diffusive mixing.

Another way to estimate the diffusion at the composition interface is to look at the time evolution of the composition profiles while they are not influenced by convective motions. The best simulation for that purpose is ImHrk-3 where we do not see any

dynamical mixing over the simulated time. Looking at the hydrogen profile of different snapshots, Fig. 4.13 shows that a tiny amount of hydrogen diffuses very quickly inwards. In Fig. 4.13 we subtract the initial hydrogen content $X_{\text{CZ},0}$ of the CZ from the spherically averaged hydrogen profiles $\langle X \rangle$ in order to enhance the low end tail of the hydrogen interface. In addition to that, the profiles of ImHrk-3 have also been shifted to the right to increase visibility.

Initially the motion of the hydrogen profile is enhanced by the transient evolution, but soon after that the hydrogen profile moves at a constant speed, which implies a diffusion coefficient of the order of $10^{10} - 10^{11} \text{ cm}^2/\text{s}$.

In the ImHrk-2 simulation the behaviour is similar, but dominated by the initial transient until mixing sets in. In ImHrk-2 it is therefore not possible to determine D from the long term evolution based on the hydrogen profiles. The value found from the ImHrk-3 simulation is the same as in simulations of a $1.5M_{\odot}$ mass star (see 4.7) as well as in 3D simulations (see 5.4). We therefore think it is an universal property of all of our simulations. We attribute the process to numerical diffusion of the composition. One possible source for this diffusion is the handling of velocities in MAESTRO. As described in 3.4 the velocity at the end of each timestep is not necessarily the advection velocity, because we enforce the velocity constraint from Eq. 3.37 at the end of each timestep. The velocity of the tracer particles therefore is slightly different from the velocity used for the advection of composition, which might explain the difference in the diffusion coefficients determined from tracer particles and hydrogen profiles.

The simulations where mixing is dominated by this effect (ImHrk-1.7, ImHrk-2, and ImHrk-3) can be identified by the step like mixing behaviour. Subtracting the effect of numerical diffusion we conclude that there is actually no mixing going on in these simulations.

Going back to the D values as determined from the tracer particles we can also compare these values with the evolutionary time of the star. Assuming that the diffusion coefficient throughout the stable layer is represented by the minimal diffusion coefficient of the order of $10^7 \text{ cm}^2/\text{s}$, the star would become mixed within 1 Myr over a distance of $\approx 10^{10} \text{ cm}$, which is of the same order as the pressure scale height at the convective boundary. Hence, during the main sequence lifetime such a diffusion coefficient would mix the whole star.

While this amount of mixing is clearly too much, one also has to consider that the velocities in the 2D simulations are about 20 times larger than predicted by MLT (see Fig. 4.4) and larger velocities in the CZ also lead to IGWs with larger amplitudes. Rogers & McElwaine (2017) found that the diffusion coefficient is tightly correlated with the mean velocity in the CZ. In Rogers & McElwaine (2017) the velocity in the CZ over time dropped by a factor of three compared with the initial velocity in the simulation. They found that this drop in velocity corresponds to a

reduction of the diffusion coefficient by 2 orders of magnitude. Extrapolating the results of our simulations down to the MLT predictions leads then to a reduction of D by six orders of magnitude.

Moravveji et al. (2016) found that stellar models of the $3.25M_{\odot}$ mass star KIC 7760680 require an additional diffusion parameter $D \approx 10 \text{ cm}^2/\text{s}$ in the stable layer in order to fit their asteroseismic observations. This is in perfect agreement with our extrapolated value for D based on MLT velocities. With such a low diffusion coefficient, diffusive mixing over the whole lifetime of the main sequence would extend only over a region of size 10^8 cm .

We can therefore argue that diffusive mixing is actually not as important for the mixing at convective boundaries as our simulations indicate. Furthermore, we can then claim that all simulations that are dominated by diffusive mixing do overestimate the overshooting parameter. The overshooting calibration then gives us an upper limit of $f_{ov} < 0.017$, corresponds to an overshooting distance of less than $4 \cdot 10^9 \text{ cm}$ or 25% of the local pressure scale height at the convective boundary $H_p \approx 1.5 \cdot 10^{10} \text{ cm}$.

In addition to the diffusion constant in the stable layer Moravveji et al. (2016) also give the overshooting parameter that is required in their 1D models to match their observations. They find $f_{ov} = 0.024$, a value larger than what we predict from our simulations. Overshooting parameters between different codes are, however, not directly comparable due to different assumptions on the initial diffusion constant D_0 in 2.12 and different implementations of cutoff functions. The mass in the overshooting region can be more directly compared. Moravveji et al. (2016) found a value of $0.2642 M_{\odot}$, which is in good agreement with our ImHrk-1.7 and ImHrk-2 simulations that contain 0.22 and $0.24 M_{\odot}$ in the overshooting region, respectively.

4.5 Entrainment

In 2.4 we introduced the entrainment law 2.18 and discussed that it is necessary to limit the entrainment process at long timescales in order to get realistic stellar models. Some of our simulations also show an almost constant mixing rate, indicating that some entrainment process is operative. Here we want to check whether these simulations can be described by an entrainment law and which conclusions we can draw from that law.

In order to check the applicability of an entrainment law of the form Eq. 2.18 it is necessary to determine the bulk Richardson number Ri_b at the convective boundary according to Eq. 2.16. While computing the rms velocity inside of the composition interface R_{chem} , required by Eq. 2.16 is straightforward, the length scale L and the

interface width d_i are in principle free parameters. The only restriction is that L needs to reflect the typical size of motions around the composition interface and d_i should cover the full width of the interface.

Cristini et al. (2019) used the stratification of the initial model to determine L and d_i as fractions of the pressure scale height H_p . In 2.2 we showed that a parametrization in terms of H_p is problematic for small central convective zones since H_p can be much larger there than the size of the CZ itself. We want to avoid this problem for our Ri_b analysis and therefore set d_i independently of H_p .

d_i we set depending on the width of the hydrogen interface. While we can estimate the width of the hydrogen interface from Fig. 4.10 to be $\approx 1 \cdot 10^9$ cm, we also know from Fig. 4.13 that the low end tail can be spread out considerably more than that. Once the low end tail gets in contact with the convective motions in the CZ, it is quickly spread out across the whole CZ. This limits the width of the interface to the distance between R_{chem} and R_{dyn} . d_i also has to take into account the shift of R_{chem} during the simulation (see, e.g., ImHrk in Fig. 4.10). We therefore set $d_i = 5.6 \cdot 10^9$ cm, which is the maximum difference between R_{chem} and R_{dyn} for all the simulations used for the overshooting estimate, to safely cover the whole interface throughout the simulations.

L can also be determined independently of H_p by using an auto-correlation function A of the fluid velocity between radius r and $r + dr$ (Mocák et al., 2009). We focus here on the radial part of the velocity U_r since this is the relevant component for the mixing across interfaces. $A(r)$ can then be defined as

$$A(r) = \frac{\langle U_r(r) U_r(r + dr) \rangle}{\langle U_r(r) \rangle^{0.5} \langle U_r(r + dr) \rangle^{0.5}}, \quad (4.6)$$

where $\langle x \rangle$ denotes the spherical average of x .

Evaluating A at the composition interfaces R_{chem} we find a narrowly peaked distribution around R_{chem} (Fig. 4.14). This indicates that only small scale flows are relevant for the transport across the composition boundary, as expected for a diffusive process. At the position of R_{struc} the correlation is much broader as shown by the black dashed line in Fig. 4.14 for the ImHrk-2 simulation, reflecting the large scale flows of convection.

In 4.4 we identified diffusion to be the dominating process in transporting matter across the composition interface, while the larger scale motion of convection is used to distribute the matter homogeneously. We reflect this in our Ri_B estimate and adopt $L = 1 \cdot 10^9$ cm corresponding to the width of the peaks in Fig. 4.14.

The computed Ri_b values are given in the last column of Table 4.2. We find that Ri_b increases with increasing f_{ov} , which suggests that the stiffening of the boundary due to overshooting might be able to stop the mixing eventually. However,

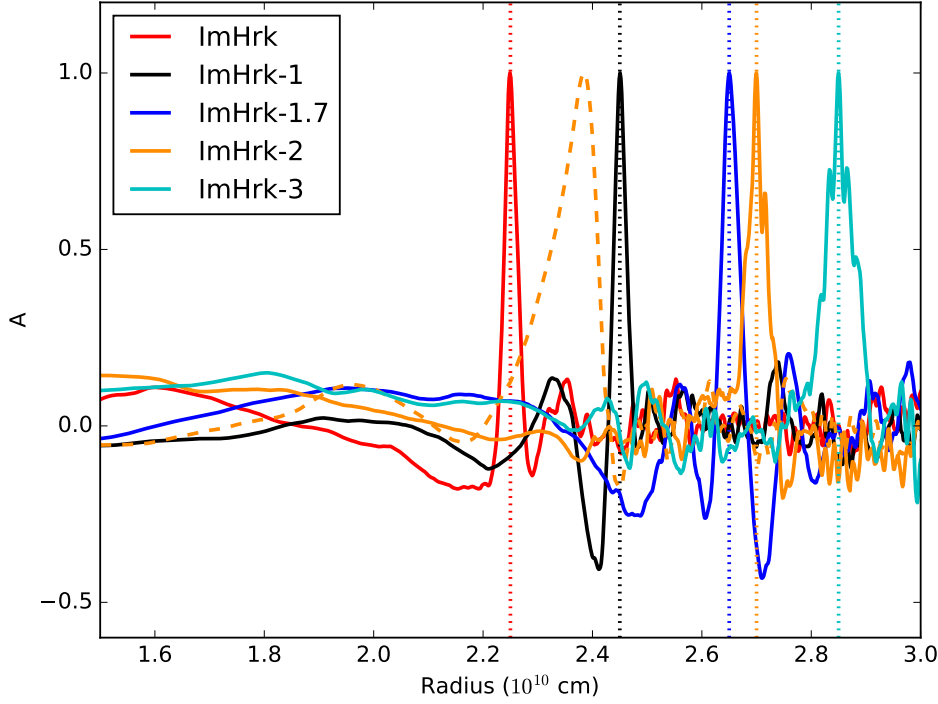


Figure 4.14: Auto-correlation function (see Eq. 4.6) of the radial velocities at the radius of the composition interfaces (dotted vertical lines) at the end of the simulations. The black dashed line shows the auto-correlation function at the Schwarzschild boundary of ImHrk-2.

when we plot the mixing rate of the ImHrk, ImHrk-1, ImHrk-1.7, ImHrk-2, and ImHrk-3 simulations against Ri_b , we find that the simulations do not follow an entrainment law as given in Eq. 2.18 (see Fig. 4.15), but the ImHrk and ImHrk-1 simulations can be fitted quite well with an entrainment law with an exponent $n = 1$. In the models with higher f_{ov} values the mixing rate is much lower than predicted by the entrainment law, i. e., the increasing stiffness of the boundary is not the mechanism that limits entrainment. In 4.6 we will find indications that the mechanism suppressing chemical mixing is rather the entrainment of entropy into the CZ.

Linden (1975) argued that the entrainment rate is limited by the amount of available kinetic energy at the convective boundary and the amount of energy that

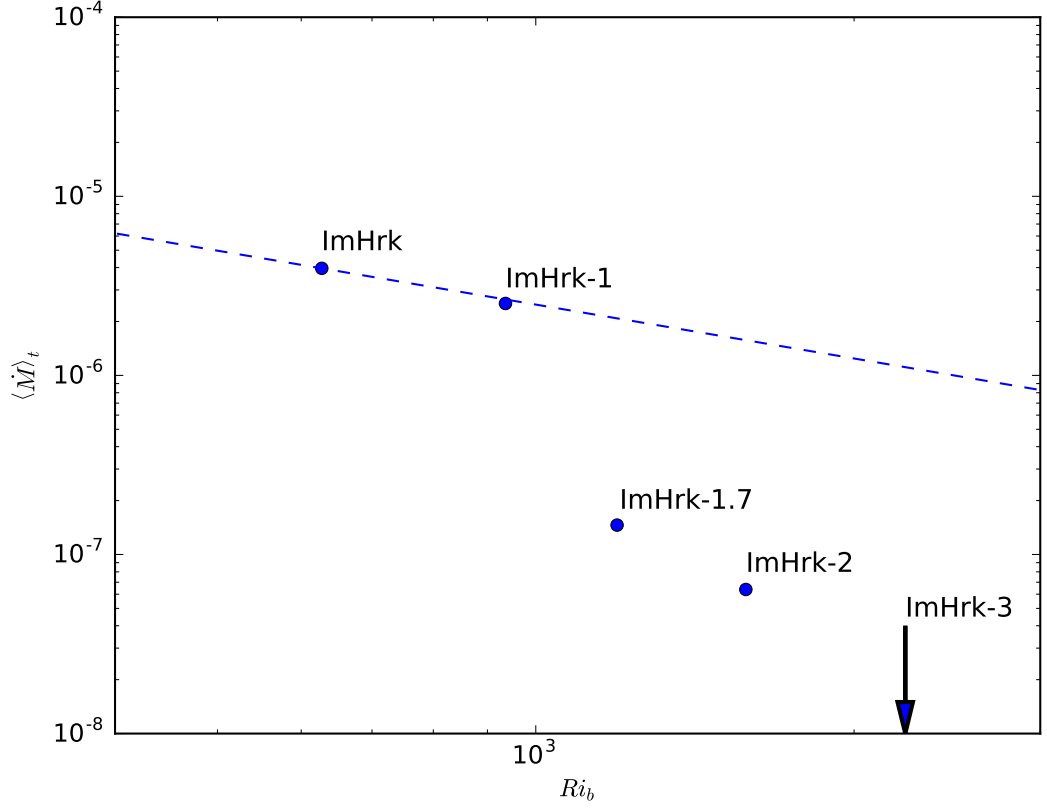


Figure 4.15: Time averaged mass entrainment rate as a function of the bulk Richardson number for the $3.5M_{\odot}$ star simulations. Each dot corresponds to a different overshooting model. The dashed line represents an entrainment law according to Eq. 2.18 with $n = 1$. The arrow labelled ImHrk-3 is pointing towards the data point of ImHrk-3 far outside the shown frame.

is needed to move a mass element across the composition interface, i.e. the stiffness of the boundary. The simulations ImHrk-1 and ImHrk have roughly the same energy input and turbulent velocities in the CZ, but the ImHrk simulation has a slightly less stiff boundary. In agreement with the picture of Linden (1975) we find that the mixing rate in ImHrk is always larger than the one in ImHrk-1. In fact, all simulations discussed in 4.4 have very similar amounts of kinetic energy and none of the mixing rates surpasses the mixing rate of ImHrk, indicating that the mixing rate of ImHrk might be an upper limit for the entrainment rate.

In 4.7 we will find that also for simulations with smaller stellar masses, the simulation without any overshooting in the initial model, sets an upper limit to the mixing rate. Hence, we can conclude that an entrainment law can only provide an upper limit to the mixing rate. Considering the long evolutionary timescales on the main sequence we then expect that the entrainment rate provides little information about the extent of the actually mixed region, because it fails when the distance between the Schwarzschild boundary and the composition interface increases. In phases of stellar evolution with shorter evolutionary timescales, however, the mixing limit set by an entrainment law might also limit the maximum extent of the mixed region.

4.6 Temperature Gradients

Besides the size of the mixed region around CZs the biggest uncertainty of 1D models is that the actual temperature stratification in that region is unknown. In 2.2 we introduced the model of Zahn (1991) that predicts an intermediate layer between the adiabatic stratification in the CZ and the radiative one in the stable layer. Even though our simulations suffer from the same problem as other hydrodynamical simulations of mixing around CZs, namely that the covered timescale is much too short to reach thermal equilibrium by radiative diffusion, we want to analyse the behaviour of the temperature gradients in our simulations.

First we need to compute the gradient $\nabla = \frac{d \log T}{d \log P}$. As discussed in 3.4, MAESTRO does not fulfil the EOS at all times. Calculating ∇ is therefore not as straight forward as in other codes. In addition, we also have to differentiate between the background pressure p_0 that is used in most of the hydrodynamical equations and the pressure perturbations π that are only included in the momentum equation 3.39. Therefore we have three different ways to compute the pressure that is needed for ∇ . We can use the background pressure p_0 , as it is the pressure that is used in most equations, or we could use the total pressure based either on the EOS p_{EOS} or the background pressure plus the perturbations $p_0 + \pi$.

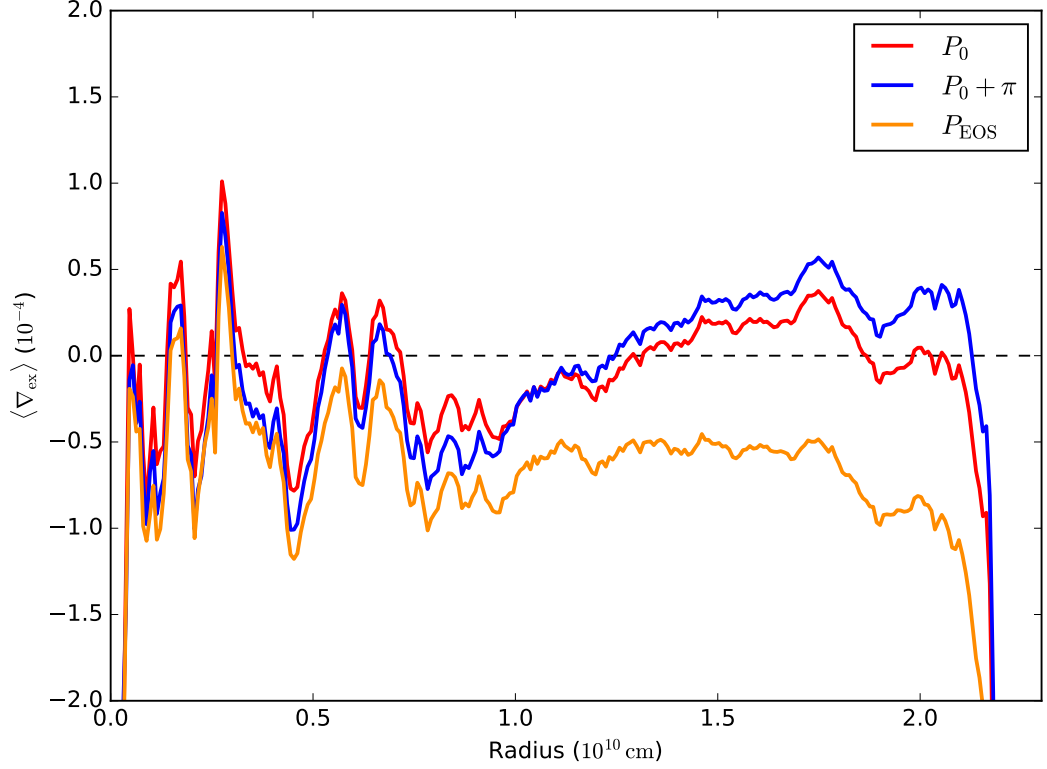


Figure 4.16: Comparison of the different ways to compute temperature gradients in MAESTRO simulations. Shown are spherically averaged profiles in the ImHrk simulation at $1 \cdot 10^8$ s

The relative drift of p_{eos} away from p_0 is of the order of 10^{-4} , the difference being largest at the convective boundary, where mixing occurs, changing the thermodynamic state. While this fact is negligible for the hydrodynamics, it causes a significant difference for the temperature gradient in the CZ. In the CZ this difference can easily change the apparent stratification from stable to unstable and vice versa. In Fig. 4.16 we show the resulting temperature gradient profiles in the CZ for the different pressures. We use the form $\nabla_{\text{ex}} = \nabla - \nabla_{\text{ad}}$, where ∇_{ad} is the adiabatic gradient provided by the EOS. This quantity appears in the Schwarzschild criterion where $\nabla_{\text{ex}} > 0$ identifies an unstable stratification. Fig. 4.16 clearly shows that the values of ∇ computed with p_{EOS} result in a mostly stable stratification at the border of the CZ, while p_0 and $p_0 + \pi$ imply larger unstable areas. Nevertheless we see convective motions throughout the CZ up until the boundary and even a bit beyond it (see 4.2), i.e., the subadiabatic regions do not seem to slow down

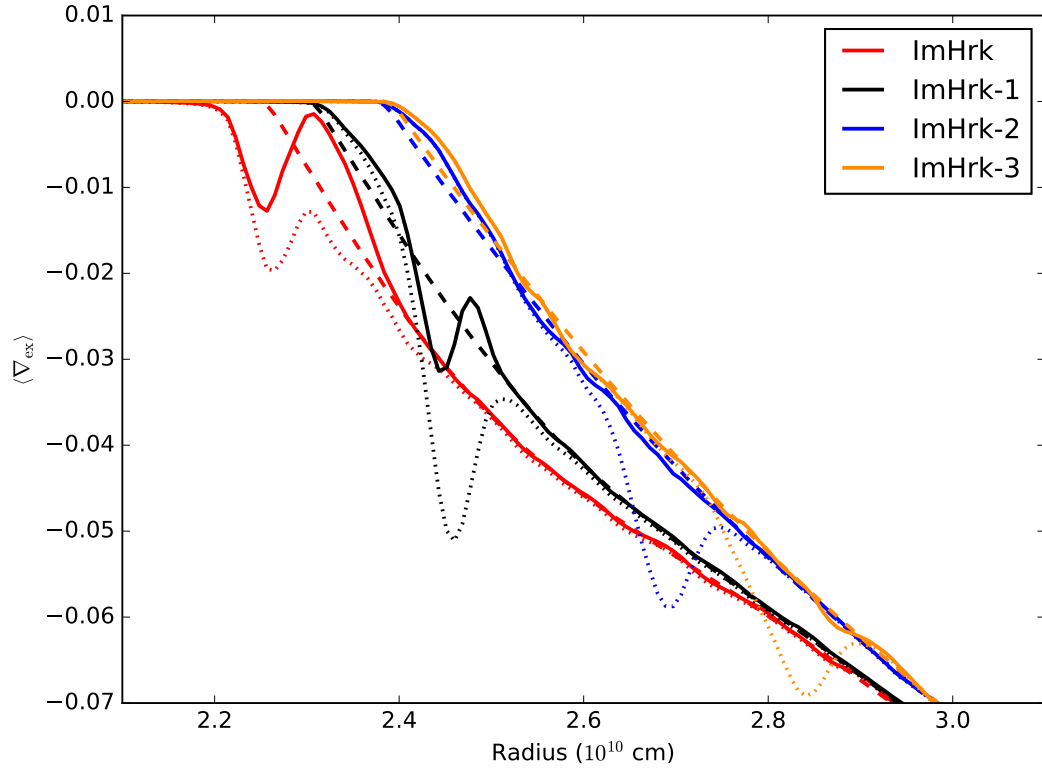


Figure 4.17: Spherically averaged temperature gradient profiles of the $3.5M_{\odot}$ star simulations. Dashed and solid lines show profiles according to the Schwarzschild criterion at $t = 0$ and after $4 \cdot 10^7$ s, respectively. The dotted lines give the initial profiles according to the Ledoux criterion.

the flow. Therefore, we consider all layers with $|\nabla_{\text{ex}}| < 10^{-4}$ as marginally stable, i.e. equivalent to $\nabla_{\text{ex}} = 0$. In practice this is only necessary in the CZ and at its boundary. In the stable layer the subadiabaticity is much larger than the uncertainty of 10^{-4} .

For the rest of this section we will use p_0 to compute ∇ , but the results are not depending on that choice.

In Fig. 4.17 we show temperature gradient profiles at the start of the simulation (dashed lines) and after $4 \cdot 10^7$ s (solid lines). Again we use the Schwarzschild criterion to differentiate between stable and unstable (marginally stable) regions.

The stability against convection is also influenced by the molecular gradient $\nabla_{\mu} = \frac{d \log \mu}{d \log P}$, where μ is the molecular weight of the fluid. Including the effects of

∇_μ in the stability analysis results in the so-called Ledoux criterion (Ledoux, 1947), where $\nabla_{\text{ex}}^* = \nabla - \nabla_{\text{ad}} + \frac{\chi_\mu}{\chi_t} \nabla_\mu > 0$ indicates an unstable stratification. χ_μ and χ_t are the thermodynamic derivatives $\frac{d \log P}{d \log \mu}$ and $\frac{d \log P}{d \log T}$ provided by the EOS. In our models ∇_μ always gives a stabilizing contribution to the stratification. We also show the profile according to the Ledoux criterion of the initial models in Fig. 4.17 as dotted lines.

The first point we notice in Fig. 4.17 is that the Schwarzschild criteria in the ImHrk and ImHrk-1 simulations follow the general shape of the Ledoux criterion after some time. This is due to the simultaneous mixing of hydrogen and entropy at the same location, which allows ∇ to adopt the influence of the composition gradient right at the composition interface. Consequently this leads to a retraction of the formal Schwarzschild boundary in ImHrk. On the other hand, the temperature gradient approaches the adiabatic one just outside of the core, indicating an efficient outward mixing of thermal energy. Initially the bump in ∇ is so close to the adiabatic one that it interferes with the computation of our structural boundary condition R_{struc} (see jump in Fig. 4.6). Over time this feature moves outwards together with the hydrogen profile, but remains constant in height. The deeper the hydrogen profile moves into the stable layer, the larger is the subadiabaticity of the background state. This means that the stability of the bump in ∇ increases over time. An influence on the driving in the CZ in the long term evolution can therefore be excluded.

In the simulations ImHrk-1.7, ImHrk-2, and ImHrk-3 that have little to no chemical mixing this feature is completely absent. Without entropy mixing ∇ cannot change and hence ∇ preserves the initially imposed stratification at R_{chem} . Nevertheless, the overshooting models do still mix entropy, but in the region of R_{struc} far away from R_{chem} . This leads to an additional feature just outside of the formal Schwarzschild boundary where the temperature gradients are pushed from the radiative gradient closer to the adiabatic one, i.e., the entropy profile is flattened in that region. In 2.2 we introduced this feature as a penetration layer.

While it seems surprising that the temperature gradient is altered, even though we are far away from simulating a thermal timescale, it can be understood with the penetration picture of van Ballegooijen (1982), who describes penetration as a competing process between convection, trying to establish an adiabatic temperature gradient, and radiative diffusion, trying to restore the radiative gradient. Convection operates on a much shorter timescale than radiative diffusion and hence a penetration region is established before ∇ can be pushed back to ∇_{rad} . In the overshooting models we clearly see the growth of the penetration layer. On the other hand, during the whole simulation of ImHrk the estimated lengthscale for radiative diffusion

corresponds to only half the width of a computational cell. This is clearly not enough to see any noticeable restoring effect from radiative diffusion. The final depth and shape of the penetration layer therefore cannot be determined from our simulations. Simply the presence of a penetration layer, however, is a clear indication that the usual 1D assumption of using the radiative temperature gradient in the overshooting layer is insufficient to describe all relevant processes.

The balance between radiative diffusion and energy transport by convection is also directly connected to the entrainment process. In 2.4 we described how a balance between the entrainment of entropy, i.e. the transport of energy, and the restoring of the entropy gradient by radiative diffusion can stop chemical entrainment. Since we do not reach an equilibrium state in the energy transport we also do not see an effect on the entrainment. However, the fact that the entropy entrainment seems to increase as the chemical mixing is reduced is a strong indication that both processes are connected and should not be considered individually.

4.7 Mass Dependence

Since overshooting in 1D models is parametrized in terms of the pressure scale height (see Eq. 2.12), the procedure fails for very small central convective zones where H_p diverges (see 2.2). In order to prevent unrealistically large mixing regions, it is necessary to investigate the behaviour and size of mixed regions in the mass range between 1.2 and $2M_\odot$. We therefore test this range by repeating the procedure of the $3.5M_\odot$ mass star with models of 1.3 , 1.5 , and $2.0M_\odot$ mass stars. In total we performed 11 additional simulations, using $3.3 \cdot 10^5$ CPU hours. An overview of the different models is given in Table 4.3.

In this section we will first discuss the models individually and then summarize the mass dependence of the results.

4.7.1 $2.0M_\odot$

$2.0M_\odot$ is the upper end of the linear scaling of f_{ov} as proposed by Claret & Torres (2016). We performed 3 simulations with $f_{ov} = 0, 0.005$, and 0.01 , where each simulation covers 80 to 90 convective turnover timescales.

Qualitatively we find similar results as for the $3.5M_\odot$ star. The low overshooting parameters in the models Im2Hrk and Im2Hrk-05 lead to a continuous mixing evolution analogous to ImHrk and ImHrk-1. Comparing the absolute values of mixing we find that curiously the $2.0M_\odot$ simulations tend to mix faster, even though the convective velocities are smaller and the boundary stiffer. Assuming that an universal entrainment law exists, we would expect the opposite behaviour.

Name	f_{ov}	t_{\max}	$\frac{t_{\max}}{\tau_{\text{conv}}}$	$M_{\text{CZ},i}$	$M_{\text{mixed},i}$	Mixing Rate	Ri_b
Im2Hrk	0	$6 \cdot 10^7$	90	0.27	0.27	$2.0 \cdot 10^{-5}$	662
Im2Hrk-05	0.005	$5 \cdot 10^7$	80	0.29	0.32	$1.2 \cdot 10^{-5}$	1970
Im2Hrk-1	0.01	$7 \cdot 10^7$	80	0.30	0.37	$2.9 \cdot 10^{-8}$	5936
Lm5Hrk	0	$1.8 \cdot 10^8$	180	0.09	0.09	$3.0 \cdot 10^{-6}$	1325
Lm5Hrk-025	0.0025	$1 \cdot 10^8$	130	0.10	0.12	$1.9 \cdot 10^{-6}$	7407
Lm5Hrk-05	0.005	$1.4 \cdot 10^8$	130	0.12	0.14	$3.0 \cdot 10^{-7}$	6421
Lm5Hrk-1	0.01	$1 \cdot 10^8$	110	0.14	0.19	$1.4 \cdot 10^{-8}$	38470
Lm5Hrk-2	0.02	$1.8 \cdot 10^8$	143	0.16	0.27	$1.7 \cdot 10^{-8}$	55122
Lm3Hrk	0	$1.3 \cdot 10^8$	30	0.02	0.02	$3.8 \cdot 10^{-7}$	1015
Lm3Hrk-025	0.0025	$1.1 \cdot 10^8$	130	0.04	0.05	$3.9 \cdot 10^{-7}$	2141
Lm3Hrk-05	0.005	$1.5 \cdot 10^8$	150	0.06	0.08	$6.0 \cdot 10^{-8}$	3775

Table 4.3: Overview of our simulations with lower stellar masses. The first column gives the name of the simulation, where the first three characters describe the total stellar mass of the model. Im2, Lm5, and Lm3 corresponds to 2.0 , 1.5 , and $1.3 M_{\odot}$, respectively. The second column shows the overshooting parameter used in the 1D model. The 3rd and 4th columns show the physical time at the end of the simulation in seconds and the number of convective turnovers, respectively. The 5th and 6th columns give the initial mass of the CZ and of the homogeneously mixed region in units of M_{\odot} , respectively. The mixing rates averaged for $t > 10^7$ s in units of M_{\odot}/yr are shown in the second to last column, while the bulk Richardson number is given in the last column.

Nevertheless we see in Fig. 4.18 that the mixing in the Im2Hrk-05 simulation approaches the Im2Hrk simulation in terms of mixing speed and then follows the evolution of Im2Hrk, indicating again that there is an upper limit for the mixing rate.

The mixing rate of the Im2Hrk-1 simulation is almost three orders of magnitude smaller than in the Im2Hrk simulation. From the bottom right panel of Fig. 4.18 we can see that this model shows episodic mixing behaviour analogous to ImHrk-1.7 and ImHrk-2. ImHrk-1, the $3.5 M_{\odot}$ model with the same overshooting parameter as Im2Hrk-1, however, shows a continuous mixing, i.e., the $2.0 M_{\odot}$ models need a smaller overshooting parameter than the corresponding $3.5 M_{\odot}$ models to develop a similar mixing behaviour. With the same argument as in 4.4 we can then infer that $f_{ov} < 0.01$.

The $2.0 M_{\odot}$ mass model is also interesting because Higl et al. (2018) found that the geometrical cutoff description (2.13) for overshooting is too restrictive in this mass range. They tested the eclipsing binary system TZ For, which is prone to undergo

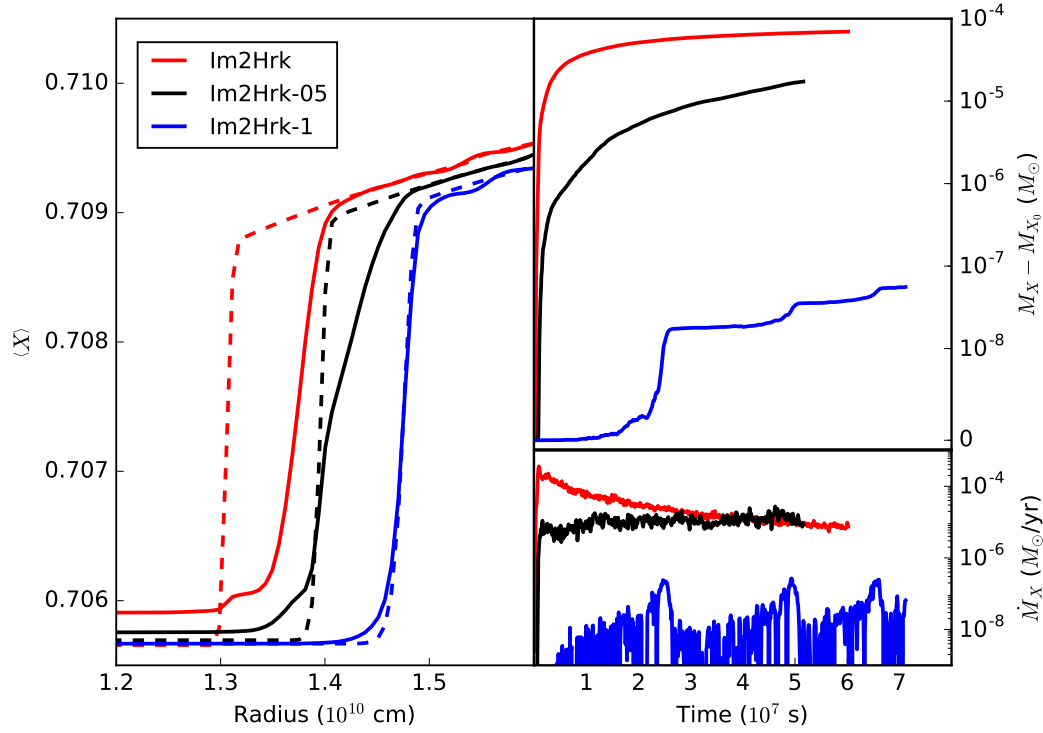


Figure 4.18: Analogous to Fig. 4.10 but for the $2.0M_{\odot}$ star and where the solid lines in the left panel show hydrogen mass fraction profiles after $5 \cdot 10^7$ s.

mass transfer during the red giant phase of the primary star. Based on observations, however, no transfer is possible in the previous evolution. To prevent mass transfer in the evolution, the star needs to develop a sufficiently large helium core at the end of the main sequence. From Table 2 in Higl et al. (2018) one can then conclude that the helium core of a $2.0M_{\odot}$ star has to have a mass of at least $0.335M_{\odot}$. The initial model of Im2Hrk-05 would result in a He-core with $0.32M_{\odot}$ (see Table 4.3). This is too low for the TZ For limit. In Im2Hrk-05 we still see significant mixing going on, so the real size of the mixed region should be larger than the initial model of Im2Hrk-05 implies. In Im2Hrk-1 we find diffusion dominated mixing and the initial model corresponds to a He-core of $0.365M_{\odot}$, above the lower limit of TZ For limit. Due to the mixing dominated by numerical diffusion we argued that Im2Hrk-1 gives an upper limit for the mixed core mass. Combining the lower limit of TZ For and the upper limit from the simulations, we can narrow down the acceptable range for the mass of the mixed core significantly.

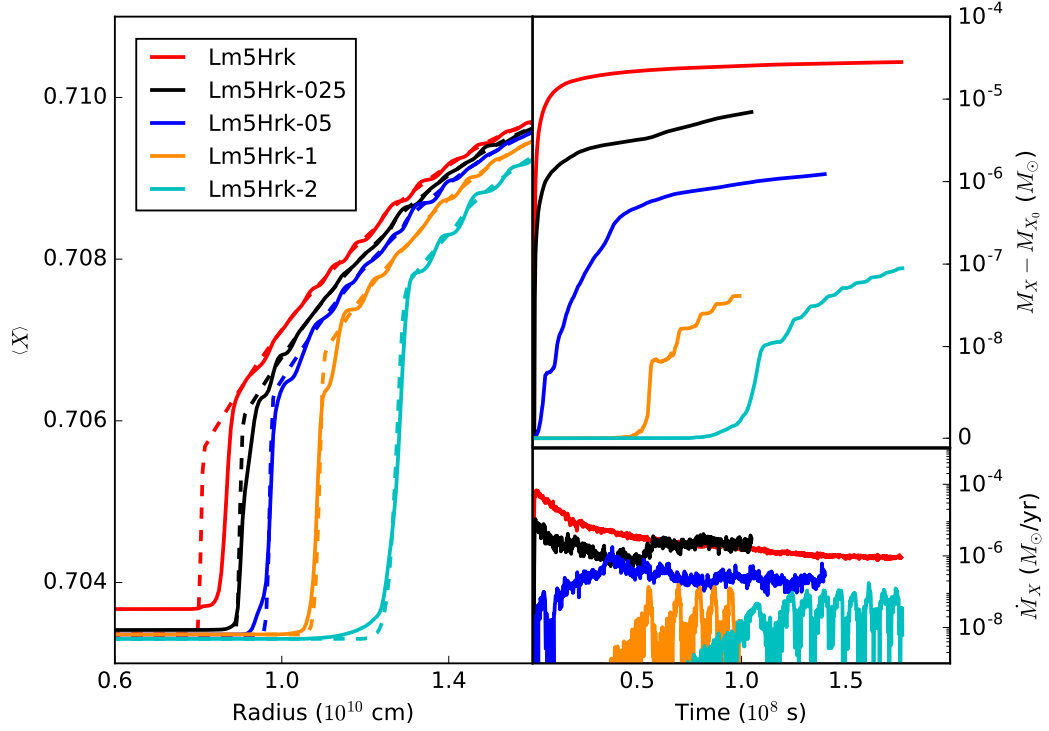


Figure 4.19: Analogous to Fig. 4.10 but for the $1.5M_{\odot}$ star and where the solid lines in the left panel show hydrogen mass fraction profiles after $1 \cdot 10^8$ s.

4.7.2 $1.5M_{\odot}$

The radial extent of the CZ in a $1.5M_{\odot}$ star is only half the size of that in a $3.5M_{\odot}$ star. H_p of the Lm5Hrk model without overshooting at the convective boundary is 60% larger than the CZ itself. With an unrestricted overshooting, $f_{ov} = 0.02$, this results in a mixed core that contains three times the mass of the model without overshooting (see Table 4.3). In this low mass model we expect to see the effect of a scaled f_{ov} much stronger than in the previous models. We performed five simulations with $f_{ov} = 0, 0.0025, 0.005, 0.01, \text{ and } 0.02$.

The $1.5M_{\odot}$ mass models again agree with the entrainment picture, as the Lm5Hrk-025 model shows continuous mixing which increases until a rate similar to that of the Lm5Hrk model has been reached. Then both curves follow the same trend (see bottom right panel in Fig. 4.19). Overall the mixing rates are now about one order of magnitude smaller than in the previous models. The computed Ri_b values also indicate a much stiffer boundary. Curiously, the Ri_b value of Lm5Hrk-05 is lower than that of the one for Lm5Hrk-025. In the left panel of Fig. 4.19 we can identify a

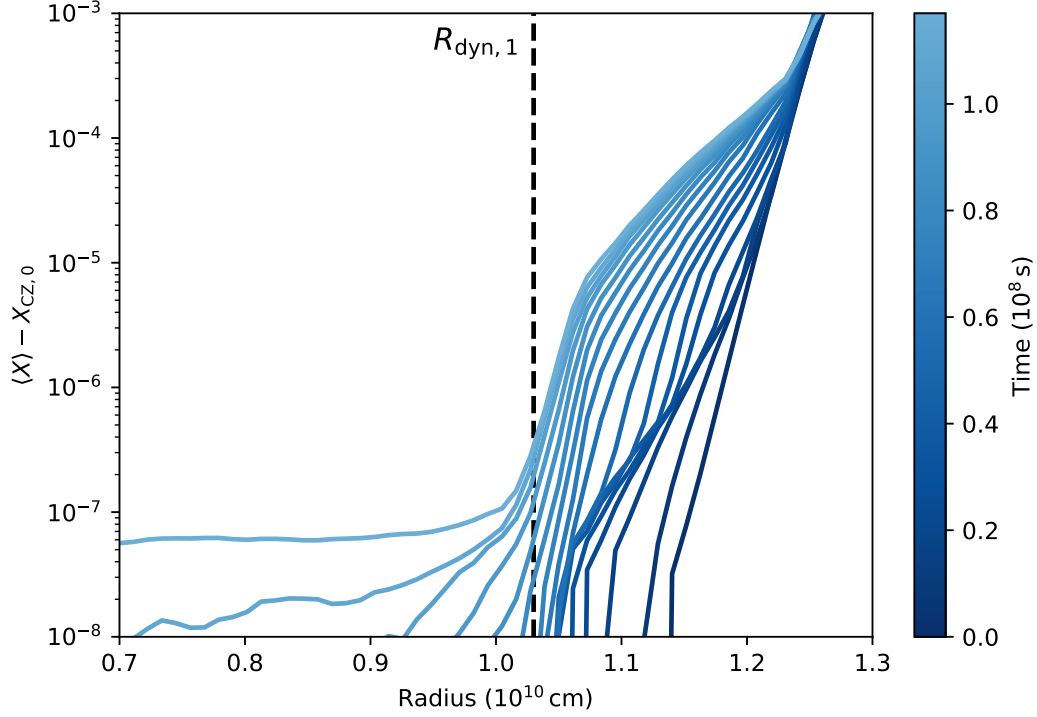


Figure 4.20: Analogous to Fig. 4.13 but for the LmHrk-2 simulation.

small knee in the hydrogen profile of the Lm5Hrk-05 simulation at the bottom of the hydrogen interface. This smooths out the N^2 profile as well, consequentially leading to a lower Ri_b value.

Again we find episodic mixing behaviour as we increase f_{ov} . The first clear appearance is as in the $2.0M_{\odot}$ models at $f_{ov} = 0.01$ in the Lm5Hrk-1 simulation. We therefore find $f_{ov} < 0.01$, resulting in a mixed region of $0.19M_{\odot}$. Yang (2016) found that the $\approx 1.4M_{\odot}$ Kepler star KIC 9812850 has a mixed core with a size of $0.140 \pm 0.028R_{\odot}$ in excellent agreement with the position of the composition interface of Lm5Hrk-1 at $0.139R_{\odot}$.

The Lm5Hrk-2 model also shows episodic mixing, which however only sets in after $\approx 7 \cdot 10^7$ s, while in Lm5Hrk-1 we already see mixing after $\approx 4 \cdot 10^7$ s. The distance between the Schwarzschild boundary and the composition interface in Lm5Hrk-2 is $1.1 \cdot 10^9$ cm larger than in the Lm5Hrk-1 simulation.

From the time difference in the onset of mixing and the increased distance between R_{struc} and R_{chem} , we can estimate a diffusion coefficient of $D = 4 \cdot 10^{10} \text{ cm}^2/\text{s}$, which is of the same order of magnitude as the estimate based on the hydrogen profiles in

LmHrk-3. The velocities in the CZ in Lm5Hrk-2 are much lower than in LmHrk-3. We would therefore expect that the diffusion coefficient is also considerably smaller. The high value of D therefore suggests that the diffusion of the hydrogen profile is *not* due to IGWs, but that it is dominated by numerical diffusion.

In Fig. 4.20 we plot the hydrogen profiles of snapshots at equidistant times in order to show the evolution during the initial 10^8 s of the Lm5Hrk-2 simulation. The differences between the profiles in the initially homogeneously mixed area are enlarged by subtracting the initial hydrogen mass fraction of the CZ. We see that the hydrogen profile initially moves inwards rather quickly, before it slows down to an almost constant speed between 3 and $7 \cdot 10^7$ s. Once the profile gets in contact with the convective flow inside of R_{dyn} (dashed line in Fig 4.20), the mixing speed increases and the tail of the profile is quickly spread out across the whole CZ. This is in agreement with the picture of diffusion supplying the hydrogen rich matter that is then mixed into the CZ by convective overshooting as described in 4.4.

4.7.3 $1.3M_{\odot}$

We also performed three simulations with $f_{ov} = 0, 0.0025$, and 0.005 for a $1.3M_{\odot}$ star. These models have a tiny convective core that contains less than 2% of the star's total mass if no overshooting is used. Due to the self consistent 1D evolution of the initial models with overshooting the mass inside the CZ triples if we use $f_{ov} = 0.005$ in Lm3Hrk-05. This already shows that changing the f_{ov} value has a sizeable impact on the stellar evolution models in that mass range. Using an unrestricted overshooting with $f_{ov} = 0.02$ we find that the mixed cores now contains roughly seven times the mass of the model Lm3Hrk without any overshooting.

The results of the mixing analysis in Fig. 4.21 follows the general trend. The mixing rate is smaller and we see episodic mixing at an even lower f_{ov} value in Lm3Hrk-05, suggesting that $f_{ov} < 0.005$. There are, however, some peculiarities in these models.

In contrast to the models with higher masses, the model without overshooting is not providing the upper limit for the mixing rate. In the bottom right panel of Fig. 4.21 we can see that the Lm3Hrk-025 and even the Lm3Hrk-05 simulation surpass the mixing rate of Lm3Hrk after $\approx 9 \cdot 10^7$ s. The main reason for this behaviour is an anomaly in the Lm3Hrk model, where the convective velocities suddenly drop by $\approx 80\%$ and remain low for several 10^7 s. We can see this in Fig. 4.22 where we plotted a time evolution of the velocity magnitude throughout the simulation Lm3Hrk. During the first $2 \cdot 10^7$ s only the CZ (white dashed line in Fig. 4.22) shows noticeably flow velocities, which are decaying slowly. Then velocities rapidly increase inside the stable layer between ≈ 0.5 and $3.2 \cdot 10^{10}$ cm, where the upper boundary is set by our damping function. The velocities are created by unresolved

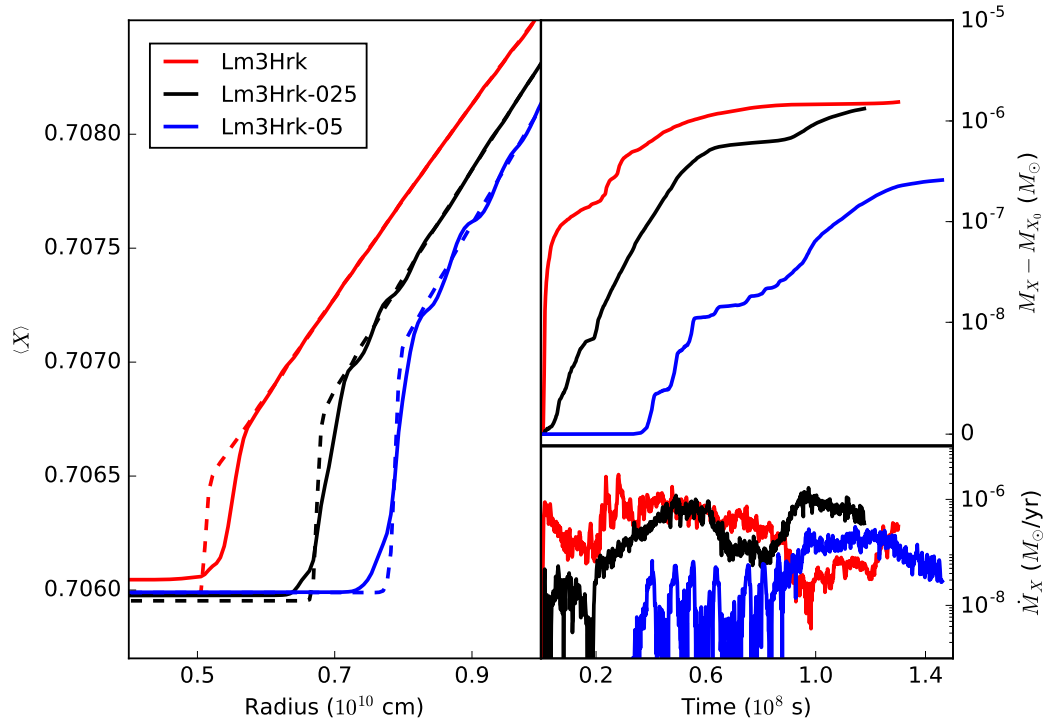


Figure 4.21: Analogous to Fig. 4.10 but for the $1.3M_{\odot}$ star and where the solid lines in the left panel show hydrogen mass fraction profiles after $1 \cdot 10^8$ s.

IGWs as described in 4.3. In contrast to the simulations with more massive stars, the stable layer has now velocities that are larger than the ones in the convective layer. This leads to a resonant wave inside the stable layer which can also be seen in the hydrogen profiles (left panel 4.21). In fact, a similar wave in the hydrogen profile can already be seen in the $1.5M_{\odot}$ mass models. This has an interesting effect on the energetics of the system:

The IGWs created by convection are now suppressed by the artificial IGWs created in the N^2 cavity at $2.5 \cdot 10^{10}$ cm and the outer boundary, and are now travelling inwards. In Fig. 4.22 we indicate the slope of the wave crests by a white dotted line, which is tilted towards the CZ. This is not the case for the $1.5M_{\odot}$ models as the internal heating there is still strong enough to push the IGWs outwards and not inwards. As the IGWs enter the CZ they are exponentially damped and deposit their energy there, which is periodically driving convective motions and mixing fresh hydrogen and entropy into the CZ. After $8 \cdot 10^7$ s the wave pattern in the stable layer changes qualitatively into a homogeneously rotating flow. The reason for that is unclear, but we see that as soon as this pattern gets in contact with the convective

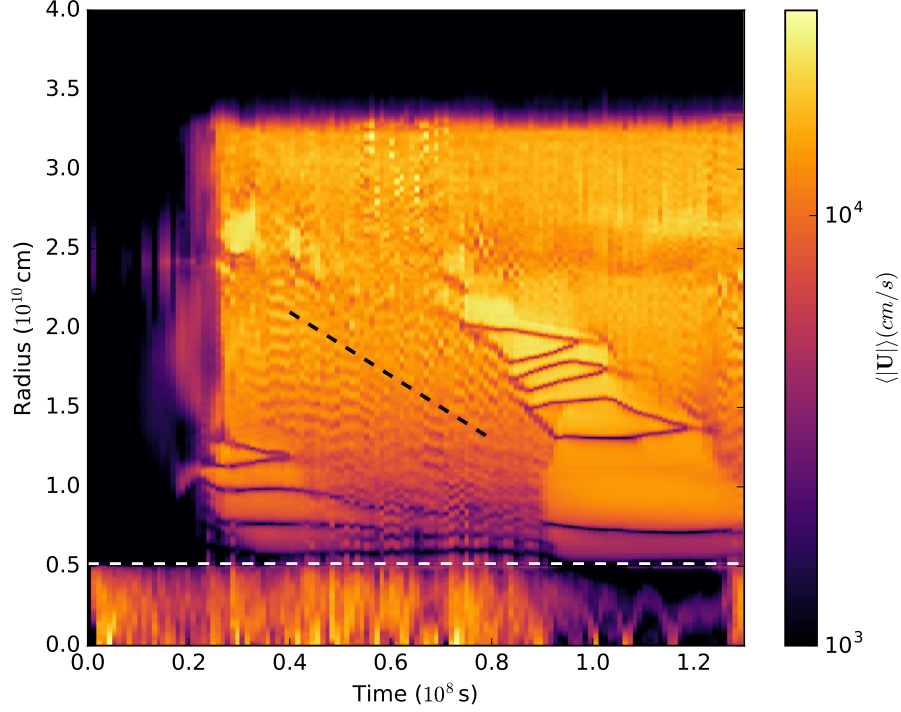


Figure 4.22: Colour plot of a series of spherically averaged velocity magnitude profiles in the Lm3Hrk simulation, over a timespan of $1.3 \cdot 10^8$ s. The radial position of the initial Schwarzschild boundary and the propagation direction of IGWs are marked by white and black dashed lines, respectively.

boundary, the velocities in the CZ drop drastically. It seems like that this new wave pattern is suppressing convection in the CZ.

In Lm3Hrk-025 and Lm3Hrk-05 the distance between the Schwarzschild boundary and the composition interface acts as a barrier between the CZ and the homogeneous wave pattern. The damping effect is therefore not noticeable. Velocities in the CZ remain large and therefore the mixing rate goes above the one from Lm3Hrk. In fact, the velocities in the CZ of Lm3Hrk-025 and Lm3Hrk-05 increase during that time, which leads to the peculiar behaviour of Lm3Hrk-05 switching from an episodic mixing to a continuous mixing at later times.

The driving of convection by artificial waves suggests that the mixing in stars should actually be smaller than observed in our models and therefore we should also use a smaller overshooting parameter. A value of $f_{ov} = 0.005$ is therefore most likely

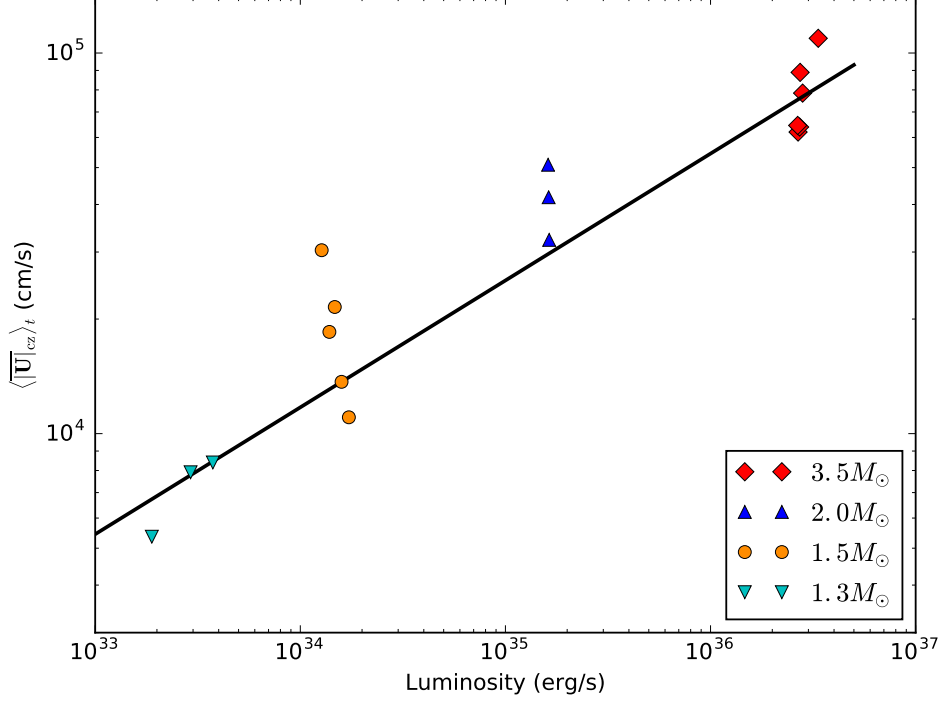


Figure 4.23: Time averaged convective velocities as a function of stellar luminosity. The predicted MLT scaling is shown as a black line.

gives an overestimation for the amount of mass mixing. We continue to argue that $f_{ov} \lesssim 0.005$, since Lm3Hrk-05 has at least a partially episodic mixing behaviour during which we can apply the same argument as before.

4.7.4 Summary

Based on the simulations with different masses we can now investigate some general trends. First we can look at the density weighted averaged velocities in the CZ \overline{U}_{CZ} and compare it with the expected $\propto L^{1/3}$ luminosity scaling from MLT (see 2.1). In Fig. 4.23 we compare this scaling (solid line) with time averaged values of \overline{U}_{CZ} (dots) and find a good general agreement over the considered luminosity range. Simulations of the same mass, but with different overshooting parameter, have very similar luminosities. The spread in velocity, however, is larger than expected from the scaling relation. This indicates that the scaling relation is only accurate to first order. One second order effect is the actual size of the CZ, which tends to be slightly

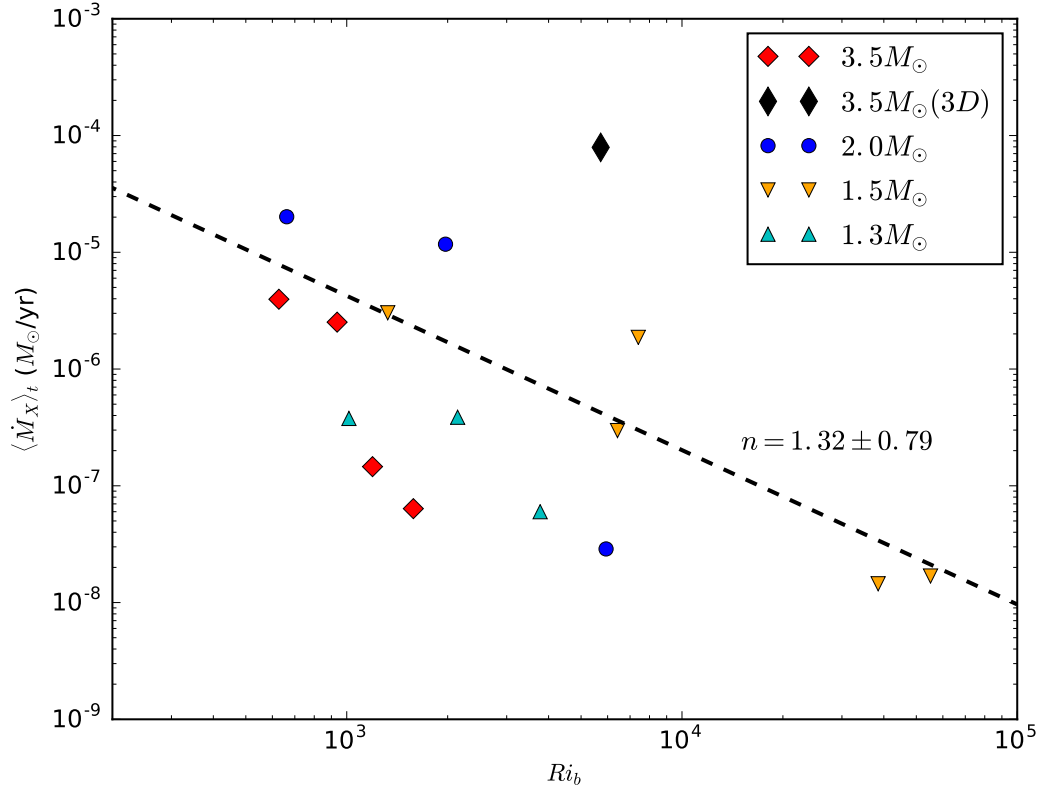


Figure 4.24: Time averaged mass entrainment rate as a function of the bulk Richardson number for all simulations. Each dot corresponds to a different model. The black dashed line represents an entrainment law according to Eq. 2.18 with $n=1.32$.

larger in the overshooting models due to the self-consistent evolution of the initial models. The change in stiffness at the convective boundary might also have an influence on the convective velocities. It might be worth investigating these second order effects to get more accurate velocity estimates for 1D stellar evolution.

The entrainment law 2.18 suggests that it is universally valid and only depends on the stiffness of the boundary Ri_b . We compute Ri_b values for all our simulations analogous to the discussion in 4.5, where the integration width d_i is chosen based on the largest distance between the composition interface and the Schwarzschild boundary for each model set and the typical lengthscale L is taken from the radial velocity correlation at the composition interface. As we go to less massive models, we find that L is slightly decreasing, while Ri_b tends to increase, which is mainly due to the reduced velocity in the CZ at lower luminosities. Between the 1.5 and $1.3 M_\odot$

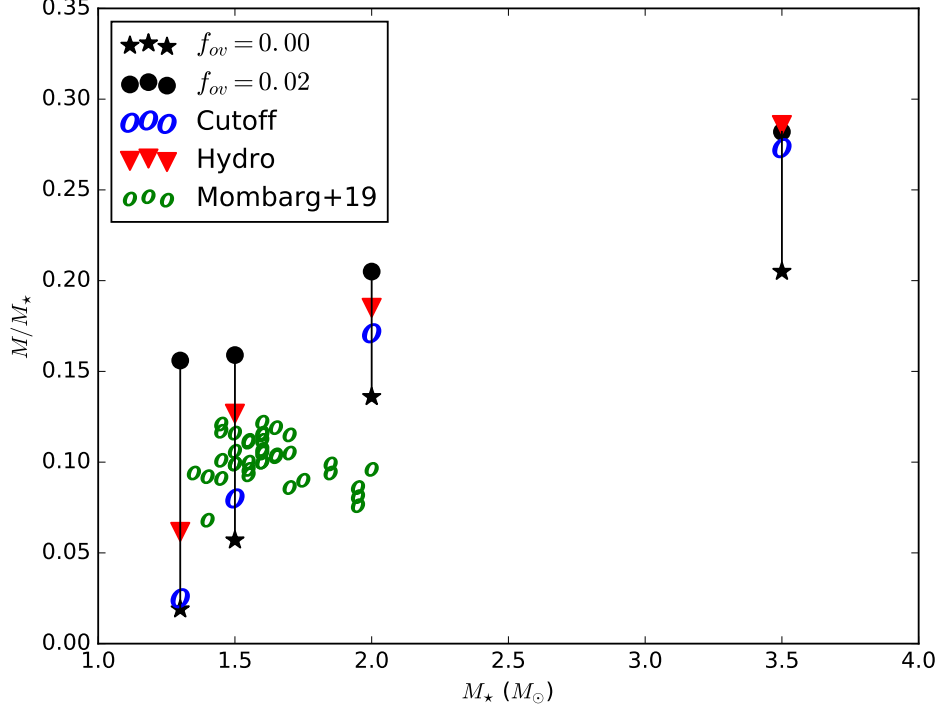


Figure 4.25: Convectively mixed core mass for models with (black dots) and without overshooting (black stars). Blue and green ellipses show the same quantity, but using a geometrical cutoff for the overshooting and observational constraints by Mombarg et al. (2019), respectively. The red triangles denote the derived upper limits from our simulations.

simulations Ri_b decreases, not because the boundary is less stiff, but because the integration distance d_i in the $1.5M_\odot$ star is considerably larger than in the $1.3M_\odot$ model.

Using the Ri_b values of all simulations in combination with their respective time averaged mixing rates $\langle \dot{M}_X \rangle_t$ we find Fig. 4.24. A linear fit to the datapoints in Fig. 4.24 gives an universal entrainment law with $n = 1.32 \pm 0.79$ and $A = 4 \cdot 10^{-2}$. The datapoint from the 3D simulation (black diamond) is excluded for this fit. The scatter of n is large indicating that an entrainment law solely based on Ri_b is not universal. Looking at the individual sets of simulations we only find a good agreement with the $1.5M_\odot$ mass set.

Finally we can also look at the scaling of f_{ov} with mass and compare it to our 1D models.

As expected, mixing rates tend to decrease with decreasing stellar mass. Within each model set we also find that an increase of f_{ov} leads to a decrease of the mixing rate. This effect gets stronger when we go to lower masses. We therefore conclude that models with a small convective core indeed require a smaller overshooting parameter. We argued that models that show an episodic mixing behaviour are dominated by diffusion, which is overestimated in our simulations. Models with an episodic mixing behaviour therefore represent upper limits for f_{ov} . We compare these upper limits with 1D models in Fig. 4.25. Due to different implementations and a different treatment of extreme cases, overshooting parameters between different 1D codes are not necessarily directly comparable. We therefore show the mass of the mixed region as a more universal quantity in Figure 4.25, which also makes it easier to compare with observations. Figure 4.25 shows results for 1D models with and without overshooting as black stars and dots respectively. The overshooting estimates are based on the canonical value $f_{ov} = 0.02$ and do not use any form of limiting the amount of overshooting. Our hydrodynamical upper limits are shown in red. These values are also given in the 6th column of Table 4.3.

Comparing the hydrodynamical estimates with the unrestricted overshooting we find that the latter largely overestimates the core masses at the lower mass end. For the $3.5 M_{\odot}$ star, however, the two values agree perfectly. It is hence evident that some form of overshooting restriction is necessary. Figure 4.25 also contains blue circles that indicate 1D Models with $f_{ov} = 0.02$ which use the geometrical overshooting cutoff Eq. 2.13. We find excellent agreement between the geometrical cutoff and the simulations for $2.0 M_{\odot}$ stars. Above and below $2.0 M_{\odot}$ the cutoff predicts a mixed region that is slightly smaller than the hydro estimates. In Fig. 4.25 we also show constraints on the mass of the homogeneously mixed core by Mombarg et al. (2019), which were derived from asteroseismological observations of γ Dor stars. The observations are clustered around $1.5 M_{\odot}$ and agree perfectly with our hydrodynamical limit for that mass. However, some of the observations indicate stellar masses of $\approx 2.0 M_{\odot}$ and convectively mixed cores less massive than those of the models without overshooting. The most likely reason for this discrepancy is the uncertainty of the stellar mass estimates in Mombarg et al. (2019), which according to them is $\pm 0.1 M_{\odot}$. Furthermore, we note that all hydrodynamically estimated upper limits also fulfil the upper limit by Roxburgh (1992), which restricts the radial extend of the overshooting layer to a size smaller than 20% of the CZ. Overall, we find that using the size of the CZ as a limiting factor for the mixed region seems to be a valid approach.

Here we want to stress that these limits on the overshooting parameter only apply for central convective zones and not for convective envelopes. The convective boundary

of convective envelopes tends to be less stiff and therefore ballistic overshooting has a larger impact. The diffusion by IGWs is also less efficient for surface CZs, because in these CZs the IGWs created by convection are actually damped as they travel into denser matter.

Chapter 5

3D simulations

In the previous chapter we showed that it is possible to test the parameter space of stellar evolution models using 2D simulations. We also showed that 2D convective flows are dominated by large scale vortices. However, convection in stars is expected to be highly turbulent, i.e., flows should easily decay into smaller structures. In this chapter we will see that these small scale structures can only be reproduced by 3D simulations, which leads to a fundamentally different flow morphology. A fully conclusive answer to the mixing at convective boundaries can therefore only be obtained with three dimensional simulations.

We performed six 3D simulations of a $3.5 M_{\odot}$ star using different initial models, integration methods, and resolutions of 512^3 and 1024^3 zones, respectively. The models were computed on the cobra cluster of the Max Planck Society and used $7.7 \cdot 10^6$ CPU hours. An overview is given in Table 5.1, where we follow a similar naming convention as in the 2D models. A 'M' or 'H' in the model name stands for a resolution of 512^3 or 1024^3 zones, respectively.

5.1 Transient

In order to analyse the influence of dimensionality on our results, we used the same domain sizes and damping parameters for the 2D and 3D simulations. The initial models of simulations with corresponding name pairs are also identical.

Consequently the initial phase of the 3D simulations resembles that of the 2D runs. Energy from the slightly superadiabatic temperature stratification is released and drives fast turbulent motions in the CZ at a velocity comparable to that found in the corresponding 2D simulations. Shortly after this initial burst the density weighted averaged convective velocities inside the CZ, $|\overline{U}|_{CZ}$, rapidly decrease by almost an order of magnitude (see Fig. 5.1). While this is qualitatively the same behaviour as the 2D simulations, the velocity drops more in 3D, i.e., the convective velocities after the initial transient are about one order of magnitude smaller in 3D than in 2D.

In the stable layer, the velocity evolution also shows some discrepancies to the 2D results. In Fig. 5.2 we show snapshots of the simulations ImMpc3d, ImMrk3d, and

Name	1D Model	f_{ov}	Int.	dt	t_{\max}	$\frac{t_{\max}}{\tau_{\text{conv}}}$	Mixing Rate	Ri_b
ImHrk3d	∇_{ex}	0	RK	\mathcal{U}	48	11	$4.0 \cdot 10^{-6}$	8307
ImMrk3d	∇_{ex}	0	RK	\mathcal{U}	9.1	2	$1.8 \cdot 10^{-5}$	36948
ImMpc3d	T	0	PC	\mathcal{U}	6.0	2	$5.2 \cdot 10^{-7}$	31860
ImHpc3dT	T	0	PC	\mathcal{U}	7.2	4	$3.8 \cdot 10^{-5}$	5891
ImMrk3dS	$\nabla_{\text{ex}} - 10^{-5}$	0	RK	100 s	13	5	$7.9 \cdot 10^{-5}$	5721
ImMrk3dS-2	$\nabla_{\text{ex}} - 10^{-5}$	0.02	RK	100 s	17	6	$1.4 \cdot 10^{-16}$	31554

Table 5.1: Overview of our 3D simulations of $3.5 M_{\odot}$ stars. A 'M' in the model name stands for a grid resolution of 512^3 zones, while a 'H' represents simulations with 1024^3 zones. The second column gives the preserved quantity during reintegration of the initial 1D model, which has been computed with an overshooting parameter according to the third column. The time integration method and the timestep criterion are characterized by the 4th and 5th columns, respectively, where a numerical value in the 5th column stands for a constant timestep with that value. The 6th and 7th column give the total simulation time and the corresponding number of convective turnover times. The time averaged mixing rate is given in column 8 in units of M_{\odot}/yr . The last column shows the bulk Richardson number at the convective boundary.

ImMrk3dS in the left, middle and right panels respectively. The color represents the velocity magnitude in an equatorial slice through the computational domain, where each row in Fig. 5.2 corresponds to the time indicated in the bottom left corner of the left panels.

In contrast to the 2D simulations (see e.g., Fig. 4.4) the velocities in the stable layer in the ImMpc3d and ImMrk3d simulations surpass the velocities in the CZ, which is marked by a white dashed line in Fig. 5.2. Comparing the left and middle panels of Fig. 5.2 shows that the simulation with the Runge-Kutta (RK) time integrator generates smaller velocities in the stable layer than the predictor-corrector scheme (PC), indicating that these velocities are again caused by unresolved IGWs.

The fact that these velocities are concentrated along the diagonals of the computational domain, indicates that the radial resolution has a large influence on the IGWs. Due to the Cartesian grid the radial resolution varies depending on the angle of a zone with respect to the domain centre. In the diagonals of the 3D domain the radial width of a cell is $\sqrt{3}$ times larger than along the domain axes. In 2D simulations this factor is only $\sqrt{2}$, which reduces the influence of this effect. Nevertheless it is still noticeable in 2D that the diagonals are less resolved, e.g., the radial velocities in the stable layer shown in Fig. 4.11 show some slight variations along the diagonals, which is not seen along the coordinate axes.

In 4.1 we showed that increasing the spatial resolution will decrease the unphysical

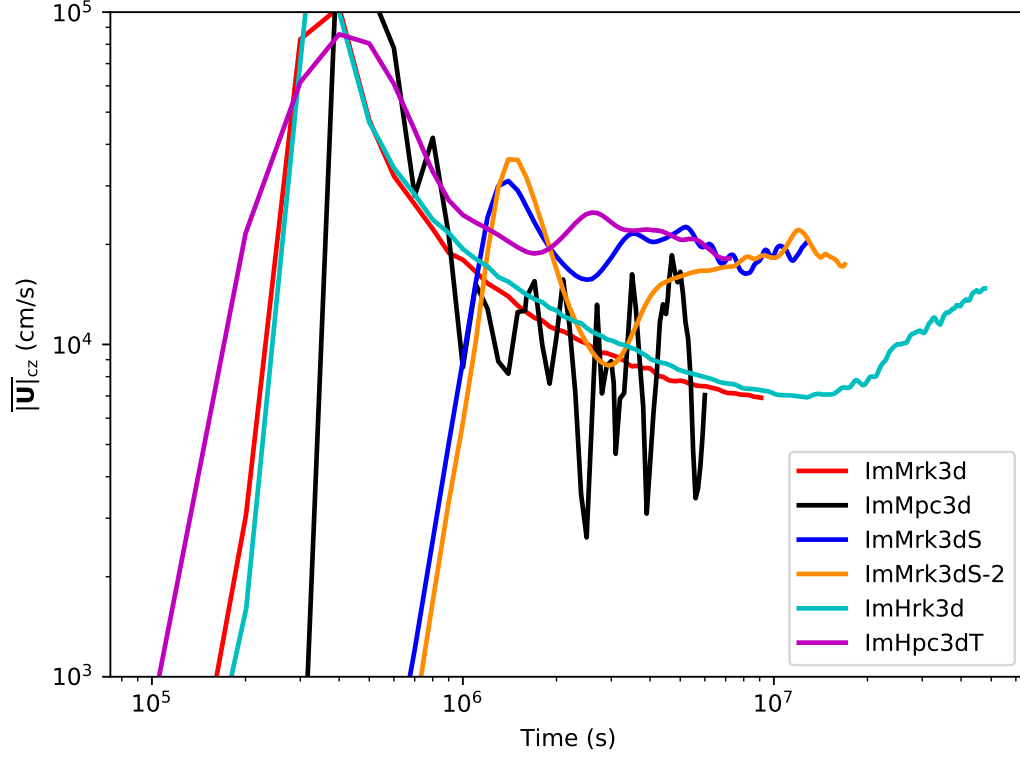


Figure 5.1: Time evolution of the density weighted averaged velocity inside the CZ (analogous to Fig. 4.1) for the 3D simulations.

velocities in the stable layer. Indeed, when we compare the velocity profiles of the simulations ImMrk3d and ImHrk3d in Fig. 5.3, we find that the velocities in the stable layer are much smaller in the high resolution simulation ImHrk3d. However, these velocities are still of the same order of magnitude as $|\overline{U}|_{CZ}$. While we expect that an even higher resolution should improve the situation further we are limited by our computational resources. Moreover, initial tests simulating only an octant of the star have shown that even increasing the resolution by another factor of two does not reduce the velocities in the stable layer significantly below $|\overline{U}|_{CZ}$.

When we continue the simulations beyond the initial transient we also see some qualitative differences between the velocity evolution in 2D and 3D. Looking at the evolution of $|\overline{U}|_{CZ}$ in Fig. 5.1 we find that the models ImMrk3d, ImMpc3d, and ImHrk3d that use the same input model as our favoured 2D simulation ImHrk do not reach a quasi-steady state after the initial velocity peak. Instead the velocity keeps decreasing for another $2 \cdot 10^7$ s, before it starts increasing again. The

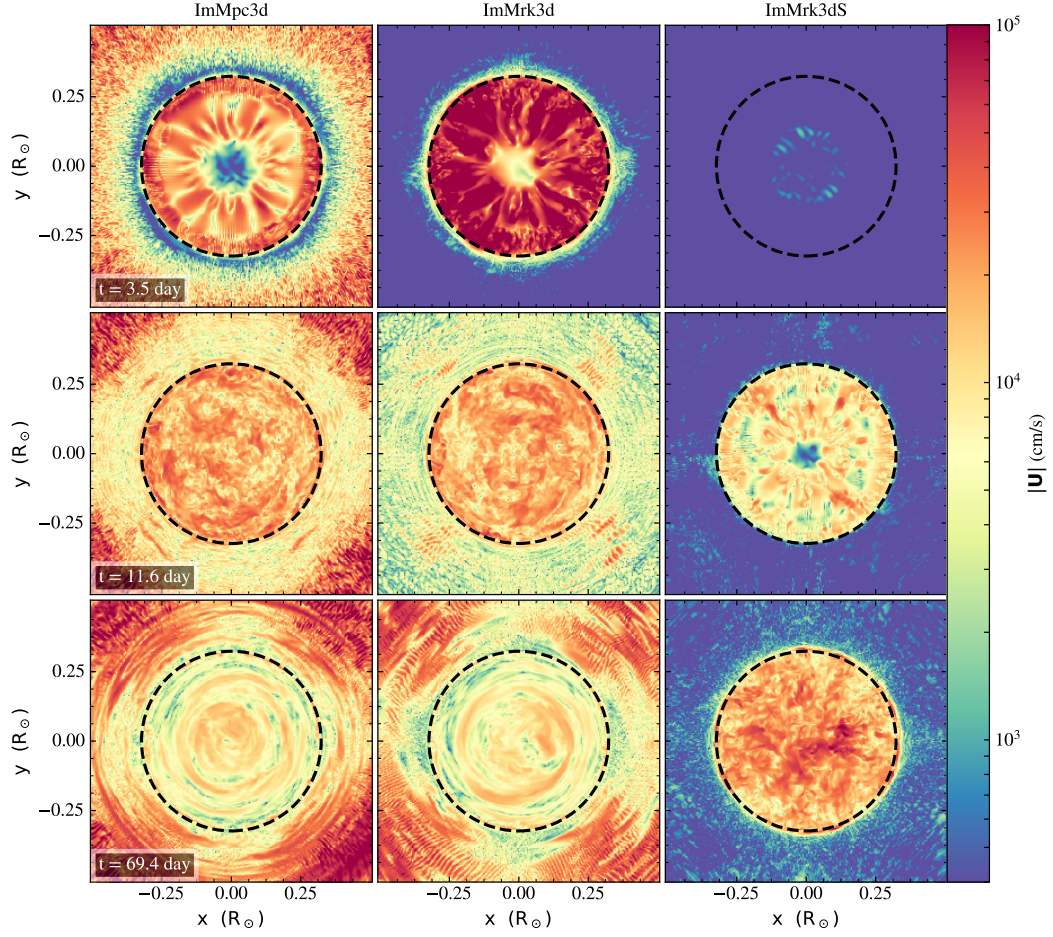


Figure 5.2: Equatorial slices of the velocity magnitude from the ImMpc3d, ImMrk3d, and ImMrk3dS simulations are shown in the left, middle and right panels, respectively. Each row shows a specific time, given in the lower left corner of the left panels. The black dashed circle indicates the location of the initial Schwarzschild boundary.

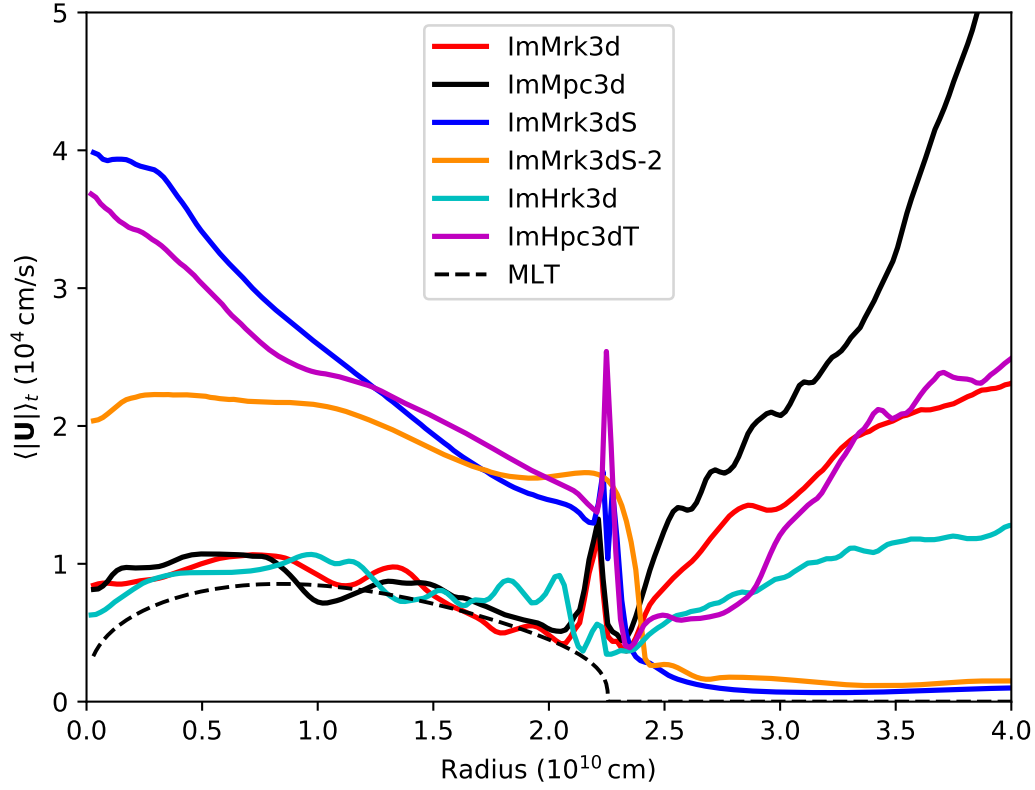


Figure 5.3: Spherically averaged velocity profiles for the 3D simulations time averaged from $5 \cdot 10^6$ s to 10^7 s. (analogous to Fig. 4.4)

reason for that behaviour is that during the initial transient, convection draws more energy than the adiabatic gradient is able to store, i.e., the heating from nuclear burning is not fast enough to restore the energy and the stratification becomes marginally stable. Therefore, the energy transport by convection subsides, which leads to a damping of the radial velocity component. The outcome of these events is a slowly rotating velocity field inside the CZ (see top right panel of Fig. 5.4, where we show the tangential velocity component in an equatorial slice of the ImHrk3d simulation and the size of the initial CZ is marked by a black dashed circle). It is also noticeable that the tangential velocity component at that point has formed large spherical structures inside the CZ.

Over time the heating from nuclear burning slowly restores the temperature gradient in the CZ and rejuvenates the convective motions, i.e., the large scale flow pattern is replaced with a small scale turbulent flow. Since the heating term is strongest in the very centre, convection starts to grow slowly from the inside to the outside, which is

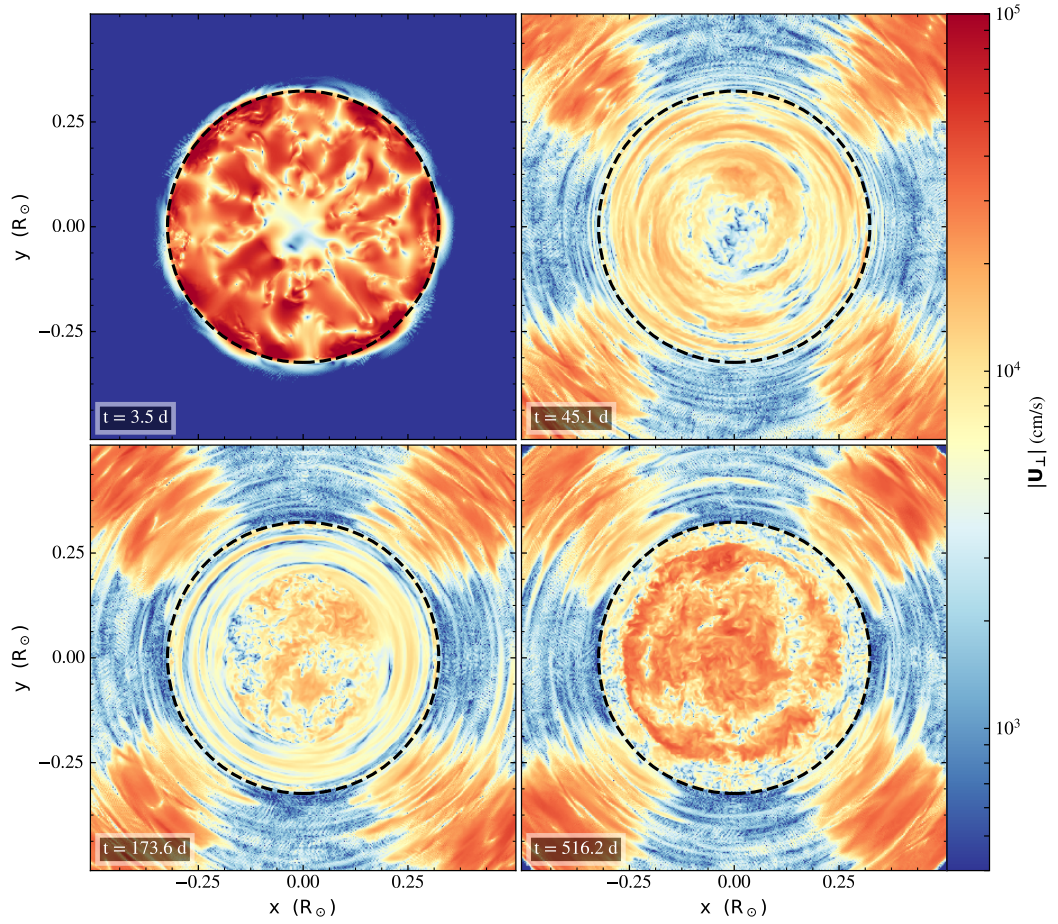


Figure 5.4: Equatorial slices from the ImHrk3d simulation showing the tangential velocity magnitude. The black dashed circle denotes the location of the initial Schwarzschild boundary.

a rather slow process. The bottom left panel of Fig. 5.4 shows that after 173 days heating has increased the amount of turbulent motions in the inner half of the CZ. However, the outer half of the CZ is still slowly rotating without any significant radial motions.

With time the turbulent region grows, but when it reaches the extent that corresponds to the bottom right panel in Fig. 5.4 it suddenly stops growing without reaching the initial convective boundary. The reason being that the initial transient has caused a stabilizing chemical gradient in this layer. Similar to the 2D simulations, the transient is connected with a strong mixing event. In the 2D simulations the hydrogen rich matter is quickly distributed across the CZ, but due to the quickly dying convection this is not the case in 3D. Instead the horizontal motion and diffusion will evenly distribute the hydrogen rich matter in a small layer near the initial Schwarzschild boundary, effectively creating an additional hydrogen interface within the CZ. Furthermore, the molecular gradient from this interface creates a layer that is stable against convection. Once the rejuvenated turbulent motion reaches this new composition interface it needs to overcome the stable gradient. Therefore, the growth of turbulence is stopped until the interface is mixed into the rest of the CZ. Due to the immense computational cost of these simulations we are not able to simulate until this happens. Therefore, the models ImMrk3d, ImMpc3d, and ImHrk3d never reach a quasi-steady state.

In nature convection is not initiated by a superadiabatic temperature gradient, but rather by a slow conversion from a stable to an unstable stratification. We therefore conclude that the transient events are due to the unphysical setup of the initial model, and that the unforeseeable consequences of transients can only be avoided reliably by removing the transient entirely.

Interestingly, model ImHpc3dT does seem to reach a quasi-steady state shortly after the initial transient (see magenta line in Fig. 5.1). ImHpc3dT is using an initial model analogous to ImHpcT where the temperature of the 1D stellar evolution has been preserved during the initial model preparation. Such an initial model has a larger superadiabaticity in the CZ, as discussed in 3.6. Consequently, the energy reservoir in the thermal stratification is not depleted as quickly as in, e.g., in models ImHrk3d. ImHpc3dT therefore does not go through the phase of damped radial velocities after the initial transient, i.e., the flow field remains turbulent throughout the simulation.

However, in 4.1 we showed that models with initially larger superadiabaticity reach a steady state with larger velocities than the models that preserve the temperature stratification of the 1D stellar models. We therefore cannot be sure that the quasi-steady state in ImHpc3dT corresponds to realistic velocity amplitudes. Nevertheless, this model shows that it is possible to find initial models that maintain the original CZ and show a well behaved velocity evolution into a quasi-steady state analogous

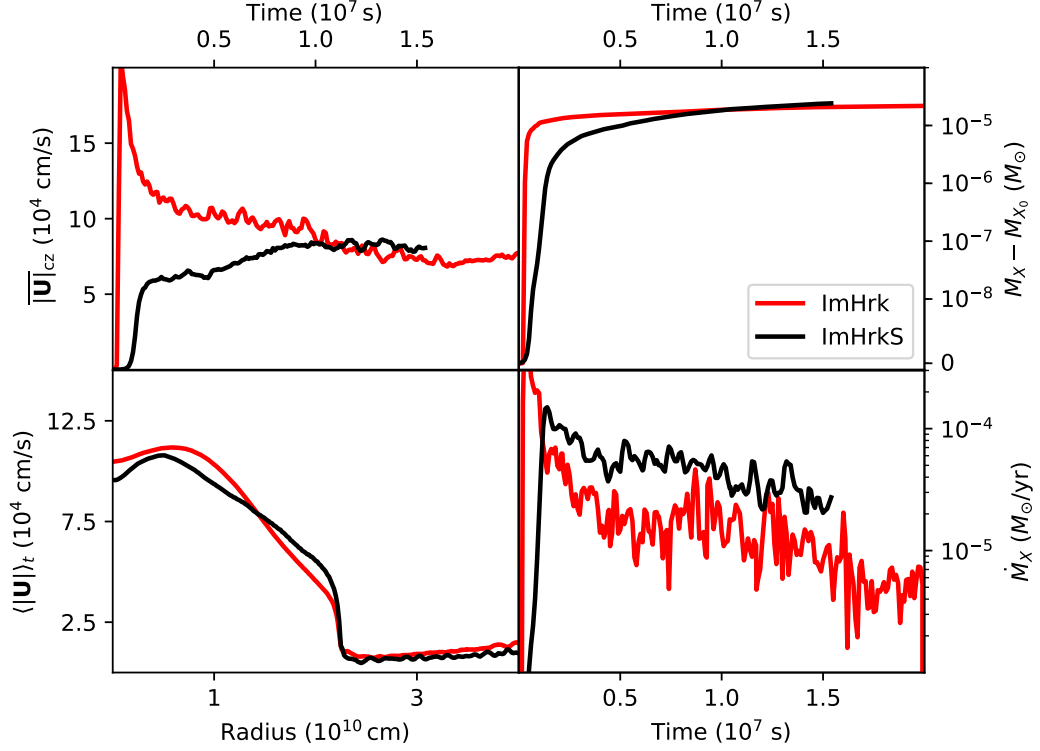


Figure 5.5: Comparison of the 2D models ImHrkS and ImHrk. The left panels show the time evolution of the average velocity in the CZ (top) and time averaged radial velocity profiles (bottom), respectively. The right panels show the time evolution of the total mixed hydrogen mass (top) and the corresponding mixing rate (bottom) (analogous to Fig. 4.8).

to the 2D simulations.

In an attempt to reduce transient effects altogether, we constructed a new set of initial models, that are initially formally stable throughout the whole star, including layers that are predicted to be unstable by 1D stellar evolution models. To achieve such a stratification we enforced a temperature gradient excess $\nabla_{\text{ex}} = \nabla - \nabla_{\text{ad}}$ in the initial models that is 10^{-5} smaller than predicted by the 1D model. This leads to a tiny subadiabaticity in the core region. Therefore, we will continue to denote the core region as a CZ, even though it is initially not convective. The effect of this modification of the temperature gradient in the stable layer is negligible, since the subadiabaticity there is in general much larger.

With such a stratification, the star will not develop convection unless the heating

function overcomes the subadiabaticity. We therefore expect that this approach will start convection in a natural way that is not connected to the sudden release of internal energy.

We tested this initial model in the 2D simulation ImHrkS to see the influence of such a modification on the results obtained in Chapter 4. A comparison between models ImHrk¹ and ImHrkS is given in Fig. 5.5. We find that ImHrkS behaves exactly as predicted. Convection sets in later than in the convective model ImHrk, but then a quasi-steady state is quickly established without causing a large peak in $|\overline{U}|_{\text{CZ}}$ (see top left panel in Fig. 5.5). Model ImHrkS reaches a similar convective velocity as model ImHrk, and also reproduces the velocity profile of the ImHrk simulation (bottom left panel in Fig. 5.5). The velocity at the convective boundary in ImHrkS is slightly larger than in ImHrk leading to a larger mixing rate (bottom right panel in Fig. 5.5). The time averaged mixing rate for $t > 5 \cdot 10^6$ s of ImHrkS is $4.3 \cdot 10^{-5} M_{\odot}/\text{yr}$. This is one order of magnitude larger than the value quoted for ImHrk in Table 4.2. However, the total mass of mixed hydrogen in ImHrk is dominated by the mixing during the transient, which increases the distance between the convectively unstable region and the composition interface early on. Therefore, it is not surprising that the mixing rate in the quasi-steady state is smaller in ImHrk than in ImHrkS, where layers with higher hydrogen content can still be accessed easily. After $\approx 10^7$ s ImHrkS has compensated the missing initial mixing due to its larger mixing rate (top right panel in Fig. 5.5).

Encouraged by the 2D test of the stably stratified model, we repeated the simulation in 3D. In order to reduce the computational cost, we used a medium resolution of 512^3 zones for the ImMrk3dS simulation. We expect that the lower resolution does not have a significant influence on the convective flow inside the CZ, because a comparison between ImMrk3d and ImHrk3d shows that the velocity evolution in the CZ is already converged at a resolution of 512^3 zones (see Fig. 5.1). Fig. 5.1 shows that $|\overline{U}|_{\text{CZ}}$ of ImMrk3dS quickly reaches a quasi-steady state, without developing a velocity peak in the very beginning of the simulation, i.e., exactly the behaviour we intended to achieve. As soon as convection sets in, the CZ in the ImMrk3dS simulation becomes turbulent as can be seen from the right panels of Fig. 5.2.

Furthermore, we see that ImMrk3dS also does not develop the large velocities along the diagonals after 70 days as seen in ImMpc3d, ImMrk3d, and ImHrk3d (see bottom panels in Fig. 5.2). Fig. 5.6 shows the time evolution of the density averaged velocity magnitude in the stable layer $|\overline{U}|_{\text{stable}}$ outside of $3 \cdot 10^{10}$ cm. In all simulations $|\overline{U}|_{\text{stable}}$ increases rapidly in the beginning of the simulations. The large velocities

¹This simulation uses an initial model, where the exact ∇_{ex} of the 1D model is preserved during the initial model preparation (see Table 4.1).

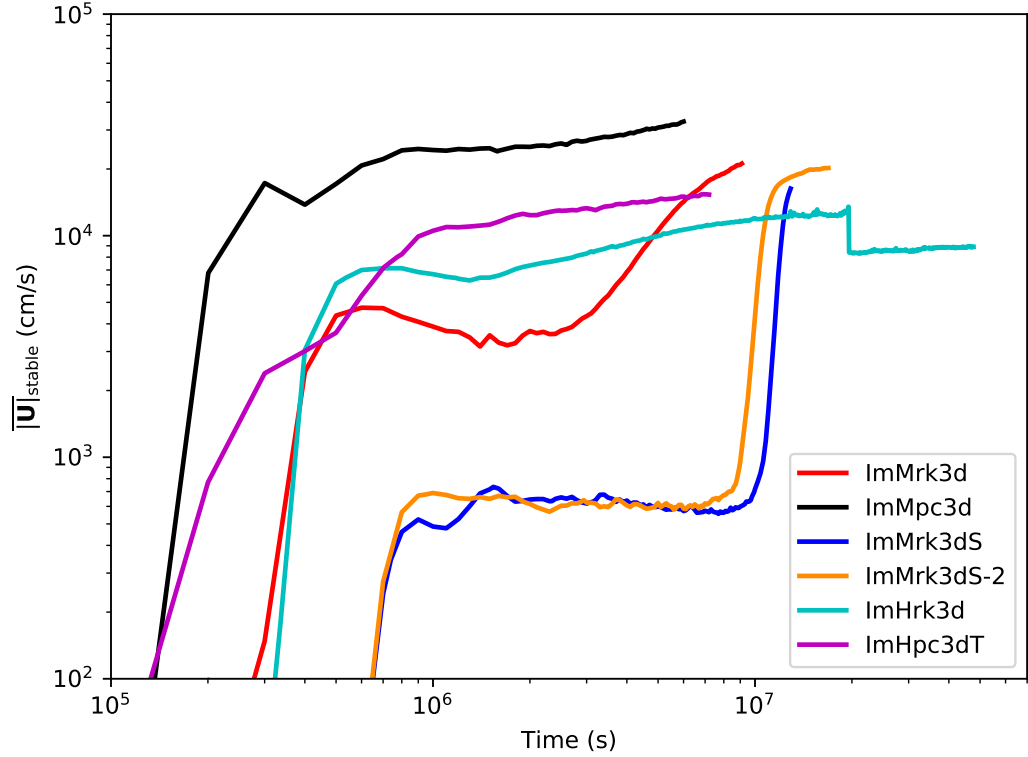


Figure 5.6: Time evolution of the average velocity in the stable layer outside of $3 \cdot 10^{10}$ cm for the 3D simulations.

seen along the diagonal in Fig. 5.2 and Fig. 5.4 are the main contribution to $|\overline{U}|_{\text{stable}}$. We further notice that the rise of velocities is delayed by several 10^5 s when we use the RK time integrator, indicating that the large velocities in the stable layer can be suppressed by increasing the accuracy of the time integration. However, as discussed before $|\overline{U}|_{\text{stable}}$ of ImMrk3d is still on the same order of magnitude as $|\overline{U}|_{\text{CZ}}$. To increase the accuracy in ImMrk3dS even further we decided to limit the timestep size to $dt < 100$ s, as indicated in Table 5.1, which is about 20% of the size of the timesteps in ImMrk3d. Limiting the timesteps increases the computational cost, but the chosen limit still provides a speed-up compared to the high resolution simulation ImHrk3d.

Fig. 5.6 shows that the higher accuracy in time used in ImMrk3dS leads to an one order of magnitude smaller $|\overline{U}|_{\text{stable}}$ during the initial 10^7 s of the simulation. Similarly, switching to the RK integrator and thereby reducing the timestep only delays the onset of the instability. After 10^7 s the instability starts to grow again until $|\overline{U}|_{\text{stable}}$ reaches a non negligible level, where an influence on the mixing can

no longer be excluded. This limits the maximum duration of the simulations, but we will see in 5.4 that this is still sufficient to investigate the differences in mixing between 2D and 3D simulations.

5.2 Flow Field

As already indicated in the previous section, the flow in 3D simulations is fundamentally different from that in 2D simulations. Instead of large scale vortices the flow in 3D is much more turbulent as we can see in Fig. 5.7, where we show a volumetric rendering of the CZ in ImMrk3dS after $8 \cdot 10^6$ s. At the time of the rendering, convection is fully developed and a quasi-steady state has been reached. Depicted is the radial velocity, where red colors indicate outflows and blue colors indicate inflows. The flow is fragmented into many tiny features, indicating a turbulent flow. However, on top of the small scale features there is also a large scale flow originating from the centre of the star, where the heating by nuclear burning is the largest. The temperature/entropy in the centre therefore increases faster than in the surrounding layers and plumes will start to move away from the CZ. These plumes will rise all the way up to the convective boundary as indicated by the continuous red patches in Fig. 5.7. Once the plumes are in the vicinity of the Schwarzschild boundary they start to turn around. In this process the plumes convert most of their radial velocities into tangential velocities as can be seen in the lower left corner of Fig. 5.7, which lacks any radial velocities. Then the plume starts to cool down and drops back all the way into the centre, creating a global circular flow pattern.

In MLT such a flow pattern would correspond to a mixing length α of the radius of the CZ. Comparing the radial extent of the CZ with the local pressure scale height H_p we find that at the Schwarzschild boundary $H_p \approx 1.5 \cdot 10^{10}$ cm, i.e., $\alpha \approx 1.5$. The pressure scale height increases towards the centre. Hence, the locally estimated α decreases. $\alpha \lesssim 1.5$ indicates that the mixing length in interior CZs should be smaller than the solar calibrated values of $\alpha \approx 1.8$.

We can also compare the time averaged velocity profiles shown in Fig. 5.3 with the MLT prediction, shown as a black dashed line.

Obviously, the simulations ImMrk3d, ImMpc3d, and ImHrk3d perfectly match the MLT predictions. However, we also have to consider that these models have not yet fully developed convection and are far away from reaching a quasi-steady state. Therefore, there is no reason why the 1D convection model should agree with the 3D results of these models. Hence, we argue that the perfect agreement between MLT and the simulations is a coincidence.

For the models that have fully developed convective motions ImHpc3dT, ImMrk3dS,

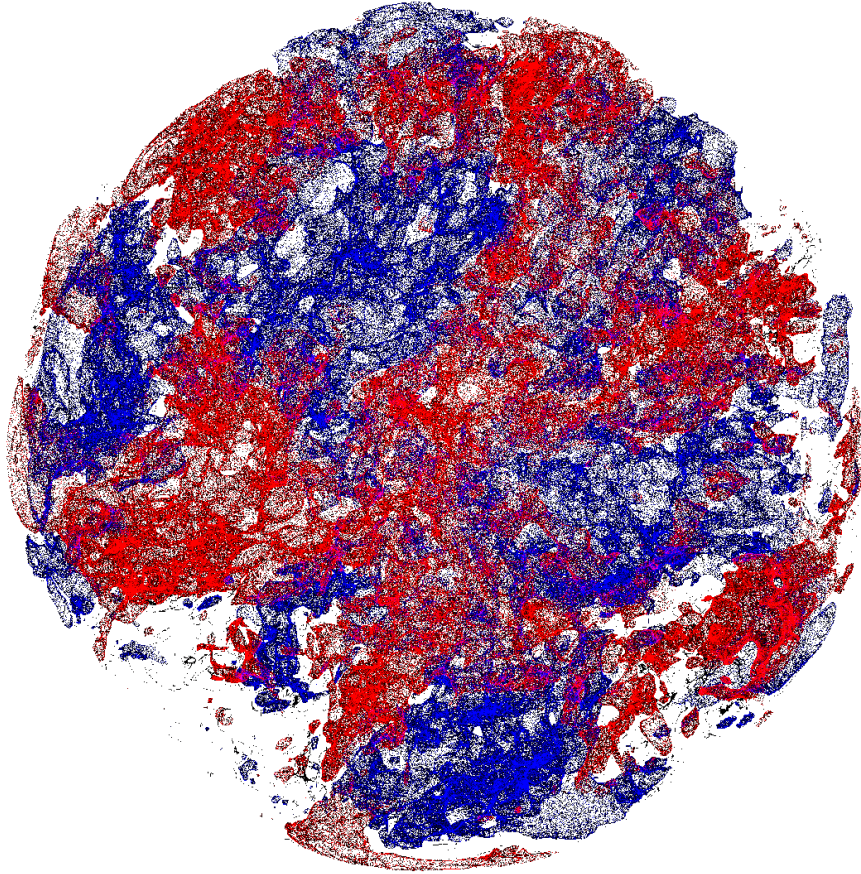


Figure 5.7: Volume render plot of the radial velocity in the ImMrk3dS simulation at $8 \cdot 10^6$ s. Red and blue colors represent outflows and inflows, respectively. Only cells that are within the CZ have been included in the rendering.

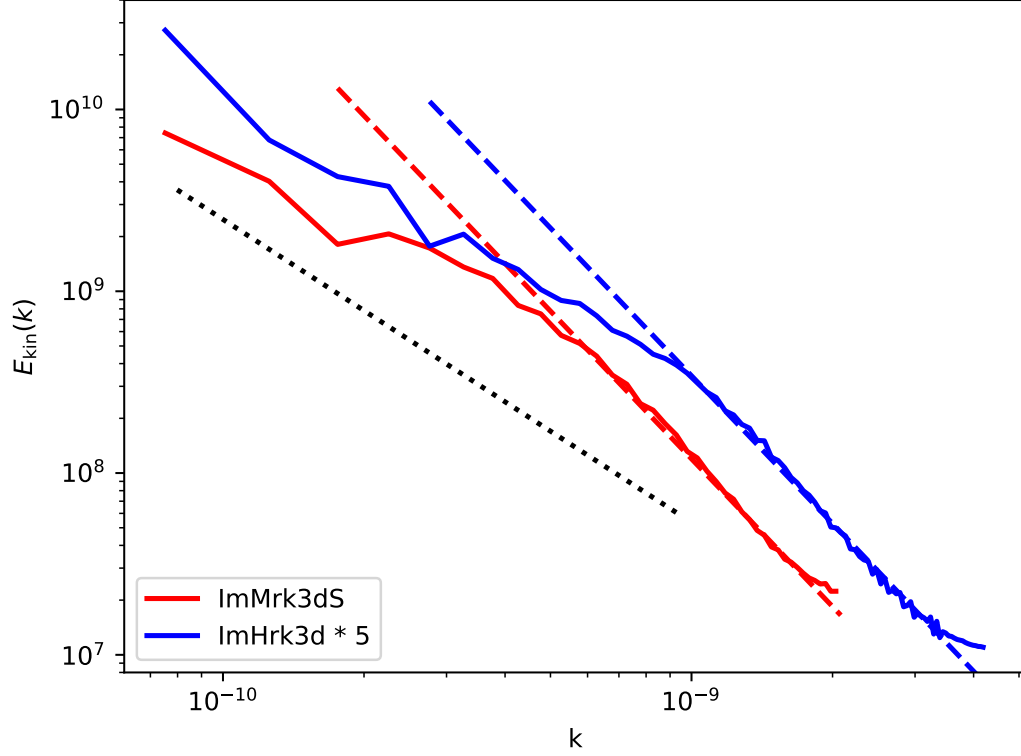


Figure 5.8: Turbulent kinetic energy as a function of wavenumber k . The dotted line indicates a $E_{\text{kin}}(k) \propto k^{-5/3}$ scaling, while the dashed lines show $E_{\text{kin}}(k) \propto k^{-2.7}$.

and ImMrk3dS-2 the velocity profiles follow the shape of the MLT prediction, scaled up by a factor of three. The small deviations from the MLT prediction in the centre of the star and directly at the boundary are due to the boundary assumption of MLT (see discussion in 4.1) and a small peak of N^2 right at the convective boundary, respectively. The small peak of N^2 is caused by the molecular gradient at the composition interface and acts as an additional IGW cavity, where IGWs can get trapped and pile up to larger velocities. In ImMrk3dS-2 we do not see this velocity peak right at the Schwarzschild boundary, because there the composition interface and therefore the N^2 peak is located further outwards.

Another quantity that characterizes turbulent flows is the power spectrum of the turbulent kinetic energy $E_{\text{kin}}(k)$. Using a Fourier transform we analyse the power spectrum of the ImMrk3dS and ImHrk3d simulations. To ensure that only convective flows are included in the analysis we reduce our output data to a cube of

width $1 \cdot 10^{10}$ cm within the CZ. For the ImHrk3d simulation we chose an output file, where the box overlaps with the rejuvenated convection, i.e., we do not expect an influence from the slowly rotating flow structure seen in the top right and bottom left panels of Fig. 5.4.

The resulting power spectra are shown in Fig. 5.8, where we multiplied the result of ImHrk3d by a factor of 5 to increase the visibility of the otherwise overlapping curves. Additionally we added a black dotted line to Fig. 5.8 corresponding to $E_{\text{kin}}(k) \propto k^{-5/3}$. This is the expected scaling for homogeneous, isotropic turbulent flows as was shown by Kolmogorov (1941) using a dimensional analysis of the Navier-Stokes equations. We see that the Kolmogorov scaling only matches the largest analysed scales.

On the other hand, at smaller scales our results show a much steeper scaling relation of $E_{\text{kin}}(k) \propto k^{-2.7}$, which is shown by dashed lines in Fig. 5.8. Similar scaling relations have been found by Edelmann et al. (2019) in simulations of a $3 M_{\odot}$ star. They attribute the discrepancy to Kolmogorov scaling to the fact that the Reynolds number Re in their simulation is ten orders of magnitude lower than in typical stellar environments, where $\text{Re} = \frac{vL}{\nu}$ is determined by the typical velocity v , length scale L , and viscosity ν of the fluid. MAESTRO solves the Euler equations and therefore does not include viscosity effects, i.e., theoretically $\text{Re} = \text{inf}$. However, due to the grid discretisation used in MAESTRO there exists some numerical viscosity. On the other hand, Edelmann et al. (2019) included a physical viscosity that is 10^{14} times larger than typical stellar values in order to stabilize their low viscosity scheme. Since we find similar scaling relations we can assume that our numerical viscosity is of similar strength as the physical viscosity in Edelmann et al. (2019), i.e., our Re is also tiny compared with stellar values.

5.3 Convective Boundary

Motivated by the distinctively different flow structures in 2D and 3D simulations, we also analyse the differences in the behaviour of the various definitions of convective boundaries as defined in 4.2.

The time evolution of the boundaries in ImMrk3dS is shown in Fig. 5.9. As in 4.2 we use time averaged spherical profiles of the tangential velocity U_r , the superadiabaticity ∇_{ex} , and the combined variation of the radial kinetic energy profiles $\langle \sigma(E_{\text{kin}, U_r}) \rangle_t$ (see Eq. 4.4) to define the boundaries $R_{\text{dyn},1}$, $R_{\text{dyn},2}$, and R_{struc} , respectively. The width of the time averaging window of the profiles is 10^7 s. In 4.2 we computed ∇_{ex} based on the background pressure P_0 . For the 3D simulations we use P_{eos} instead, as it is one of the output quantities of MAESTRO. This choice does not influence the result as we already discussed in 4.6. The chemical boundary

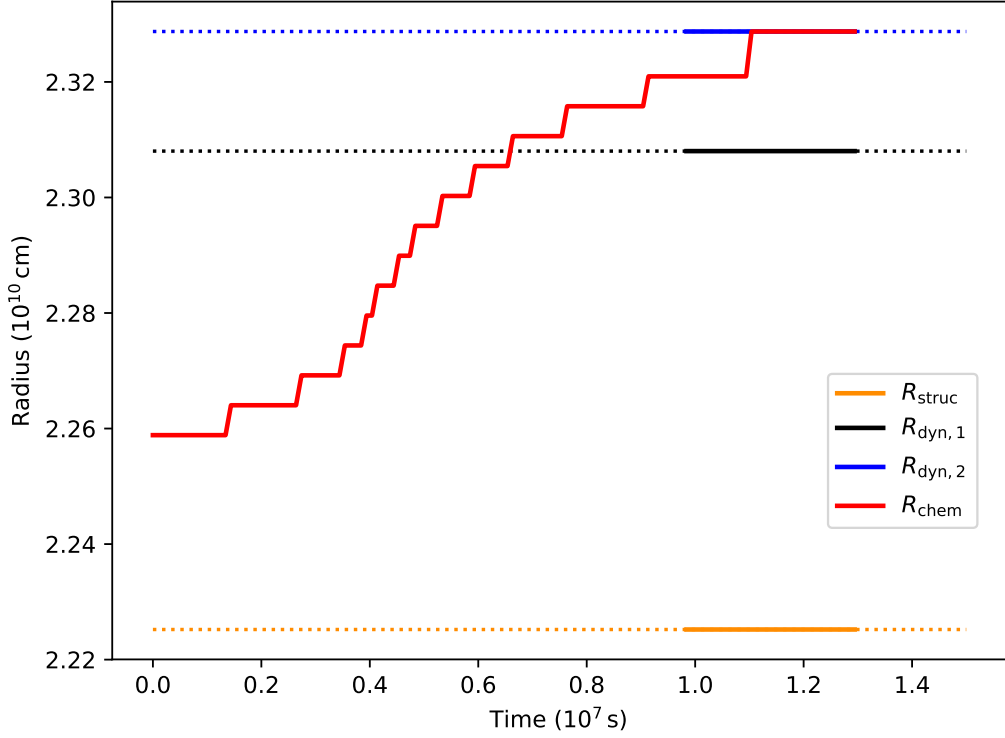


Figure 5.9: Analogous to Fig. 4.6, but for the ImMrk3dS run. The dotted lines extend the determined boundary locations for visual purposes.

R_{chem} is set by the spherically averaged profiles of the hydrogen mass fraction of each output file.

In our 2D simulations we saw an influence of the transient on the dynamical boundaries. Since the transient phase has been removed in ImMrk3dS we do not see such an influence in 3D. Therefore, we find that all boundaries except for R_{chem} are constant in time.

The initial model was set up to be slightly subadiabatic throughout the CZ predicted by the 1D stellar evolution. Therefore, there is no structural boundary initially. Once convection sets in, ImMrk3dS establishes a new R_{struc} , which is located at $2.18 \cdot 10^{10}$ cm, i.e., $0.05 H_p$ closer to the centre as predicted by the 1D model. However, this discrepancy between predicted and simulated R_{struc} is only half of the inward shift of R_{struc} induced by the transient event in 2D simulations

(see discussion in 4.2).

The distance between R_{struc} and $R_{\text{dyn},2}$ is about $0.07 H_p$ in ImMrk3dS, which is almost twice the distance compared with the 2D model ImHrk.

Therefore, we conclude that dynamical mixing events of ImMrk3dS extent farther into the stable layer than in 2D simulations, indicating that 3D boundaries are less stiff. However, when we compute the respective Ri_b values according to Eq. 2.16 we find that 3D simulations have one to two orders of magnitude larger Ri_b values than their respective 2D counterparts. The auto-correlation function of the radial velocity (Eq. 4.6) of the 3D simulations shows a similarly broad peak as in 2D around the composition interface, indicating that the typical length scale of convection is similar in both cases.

The discrepancy in Ri_b is therefore caused by the smaller convective velocities in 3D simulations. This also explains the exceptionally large difference between the ImMrk3d simulation and the respective 2D simulation ImMrk, because ImMrk3d was stopped in a phase of minimal convective velocity (see Fig. 5.1).

The evolution of R_{chem} follows exactly the simplified description of mixing given in 4.2, where the overshooting distance is set by dynamical events only. The step like evolution of R_{chem} in Fig. 5.1 is due to the radial bin size of the spherically averaged hydrogen profiles used to define R_{chem} .

During the first 10^6 s there are no significant velocities in the CZ of ImMrk3dS (see Fig. 5.1). Hence, no mixing occurs and R_{chem} remains constant. Once the convective flow has been build up, the mixing rate is increasing as can be seen from the shorter timespan between steps in the red line of Fig. 5.9 between 3 and $5 \cdot 10^6$ s.

After $5 \cdot 10^6$ s the mixing rate starts to slow down again. The decline of the mixing rate intensifies noticeably as soon as R_{chem} reaches values greater than $R_{\text{dyn},1}$ at $6 \cdot 10^6$ s. From that point on the bulk of the flow does not reach layers with larger hydrogen abundances any longer and rare events, reaching out to $R_{\text{dyn},2}$, have to account for the mixing. In contrast to the 2D simulations R_{chem} in ImMrk3dS does exceed $R_{\text{dyn},2}$, removing the need for an additional diffusive mixing to account for the observed overshooting distance. However, we would expect that R_{chem} grows beyond $R_{\text{dyn},2}$ at later times due to (numerical) diffusive mixing.

5.4 Mixing

In 4.4 we showed that diffusive mixing by IGWs contributes significantly to the mixing around convective boundaries in 2D simulations. For the 3D simulations we do not have enough output files to follow the diffusion by IGWs accurately enough,

but based on the average velocity amplitudes in the stable layer $|\overline{\mathbf{U}}|_{\text{stable}}$ we can estimate their influence in 3D simulations.

As discussed in 5.1, the higher temporal accuracy in the 3D simulations ImMrk3dS and ImMrk3dS-2 suppresses the large velocities along the diagonals in the stable layer for an extended period of time between 1 and $8 \cdot 10^6$ s (see Fig. 5.6). During that time we find that $|\overline{\mathbf{U}}|_{\text{stable}}$ is about one order of magnitude smaller than in 2D simulations, i.e., the amplitude of an IGW created by convection is also one order of magnitude smaller than in 2D simulations. This is a clear indication that 2D simulations largely overestimate diffusion by IGWs. A similar result is found for $|\overline{\mathbf{U}}|_{\text{CZ}}$, hinting towards a strong correlation between $|\overline{\mathbf{U}}|_{\text{CZ}}$ and $|\overline{\mathbf{U}}|_{\text{stable}}$.

Combining the estimated values of D from 2D simulations with the expected scaling of D with $|\overline{\mathbf{U}}|_{\text{CZ}}$ based on the results of Rogers & McElwaine (2017), we find that in 2D simulations D is overestimated by four orders of magnitude.

While this is still two orders of magnitude larger than the predictions of D by Moravveji et al. (2016) based on asteroseismic observations, it also corresponds to a mixing distance of the order of $0.1 H_p$ during the main sequence lifetime in perfect agreement with our overshooting expectations.

The amplitude and diffusion constant of propagating IGWs are damped by diffusive radiative energy transport (see e.g. Ratnasingam et al., 2019). Since we cannot follow the respective thermal timescales of radiation transport in our simulations we would therefore expect that in a star D decreases further the farther a wave propagates. Such an additional damping of IGWs in the outer layers might explain the diffusion estimates by Moravveji et al. (2016).

Considering the good agreement between the overshooting distance and the diffusion estimates from our 3D simulations in combination with an additional damping at greater distances to the convective boundary, we argue that our 3D simulations provide decent estimates for D close to the convective boundary, but overestimate it farther away from it.

We can also use the 3D simulation ImMrk3dS-2 to again analyse the numerical diffusion of composition. Analysing the motion of the low end tail of the hydrogen mass fraction profile analogous to 4.4 and 4.7.2, we see that the motion is almost constant throughout the simulation ImMrk3dS-2 (Fig. 5.10). The resulting diffusion coefficient is to be estimated of the order of $10^{10} \text{ cm}^2/\text{s}$, in agreement with the previous estimates. This agreement between 2D and 3D with different initial models again suggests that numerical diffusion is the dominating effect.

Finally, we also compare the obtained mixing rates of the 2D and 3D simulations, showing in Fig. 5.11 the evolution of the hydrogen mass M_X inside the mass shell that corresponds to the initial Schwarzschild boundary.

Looking at this figure and comparing it with the right panels of Fig. 4.10 we find

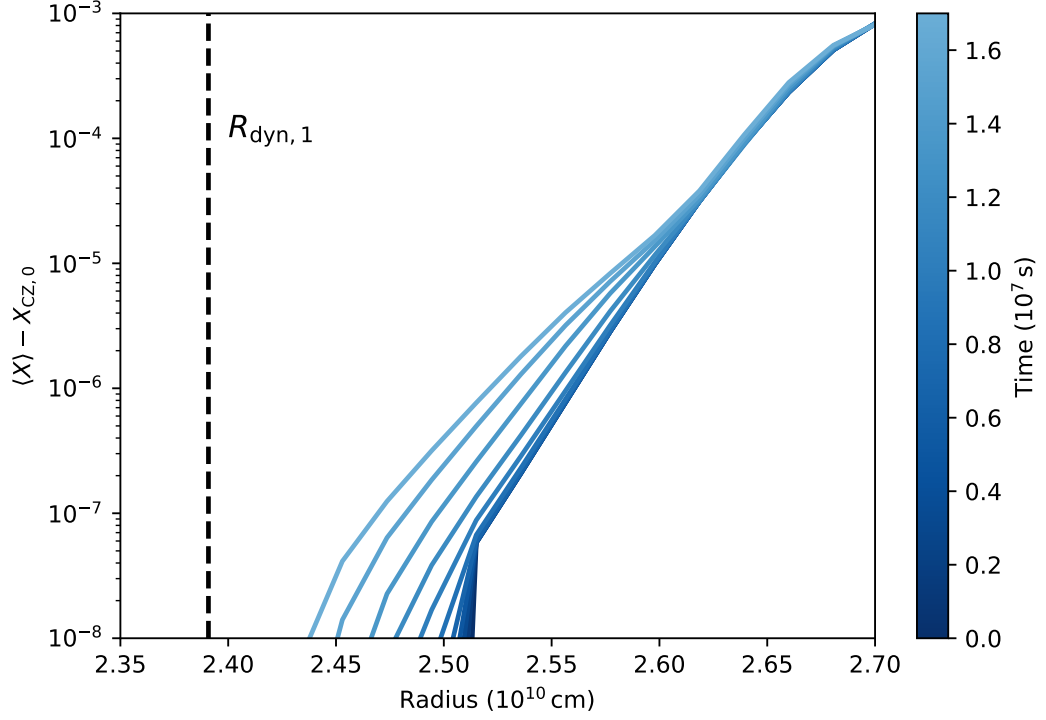


Figure 5.10: Analogous to Fig. 4.13 but for the ImMrk3dS-2 simulation.

that the time evolution of mixing in 2D and 3D agrees qualitatively well for the models without overshooting. On the other hand, the 3D simulation ImMrk3dS-2 does not show the episodic mixing behaviour we see in the 2D model ImHrk-2. This is due to the transient event in ImHrk-2 which gives an initial boost to the diffusive mixing in 2D and quickly brings the composition interface in contact with the dynamical events. Once we will reach this point in ImMrk3dS-2, we expect that it also develops an episodic mixing behaviour. From Fig. 5.10 we can estimate that it would be necessary to extent the simulation by $\approx 10^7$ s in order for the low end tail of the hydrogen profile to reach the dynamical mixing layer. Unfortunately, we cannot simulate that long because the IGW velocities along the diagonals exceed the convective velocities long before the phase of episodic mixing.

Furthermore, we find that the time averaged mixing rate in ImMrk3dS is one order of magnitude larger than in the 2D simulation ImHrk (see Tables 4.2 and 5.1). We already saw a similar discrepancy between the 2D models ImHrkS and ImHrk in 5.1. There we attributed the different mixing rates to the missing transient in the ImHrkS simulation, which requires larger mixing rates over an extended period of

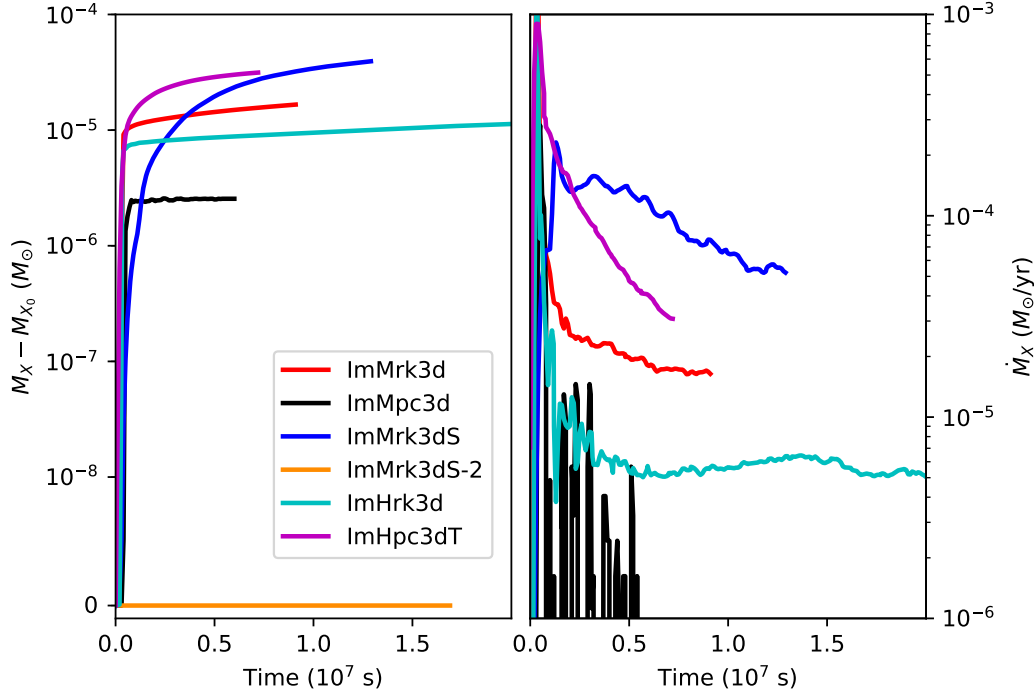


Figure 5.11: Left panel shows the change in hydrogen mass inside of the initial convective core for the $3.5M_{\odot}$ star 3D simulations. The right panel shows the time derivative of that quantity.

time in order to reach the same total mixing as during the transient event of ImHrk. The mixing rates of ImMrk3dS and ImHrk are therefore not directly comparable. However, we find that the mixing rates of ImMrk3dS is also two times larger than in ImHrkS.

We can also see this in Fig. 4.24 where we compare the Ri_b values of all 2D simulations with their respective mixing rates. The black diamond in Fig. 4.24 corresponds to the ImMrk3dS simulation and is located way above the entrainment law determined in 4.5. This is a clear indication against an universal entrainment law and for an increased entrainment speed, i.e., a less restrictive entrainment limit in 3D.

On the other hand, we find that the time averaged mixing rates of ImHrk and ImHrk3d agree perfectly well. However, we have to consider that ImHrk3d has not reached a steady state and shows increased convective velocities towards the end of the simulation (Fig. 5.1). Therefore, we would expect that the mixing rate in

ImHrk3d will exceed the one of ImHrk once convection is fully established.

Overall we see that the mixing rates obtained from 3D simulations are generally larger than in their 2D counterparts. However, the difference is only within a factor of a few, while the mixing rates between initial models with varying overshooting parameters differ by orders of magnitude. We therefore conclude that 2D simulations are a viable method to probe the extent of overshooting regions.

Chapter 6

Conclusion and Outlook

Turbulent mixing of matter across the boundary of convective cores on the main sequence strongly influences the evolution of stars that are more massive than $\approx 1.2M_{\odot}$. Mixing hydrogen into the convective burning region will extend a star's lifetime and determine the mass of the He-core at the end of the core hydrogen burning phase. To get reliable information about the involved mixing processes, and the extent and mass of the mixed zone, it is important to simulate the convective flow for as many convective turnovers as possible. We showed that 2D simulations with the low Mach number code MAESTRO are able to cover hundreds of convective turnovers at a reasonable computational cost. This allows one not only to study the evolution of mixing with time, but also to repeat the simulations with modified

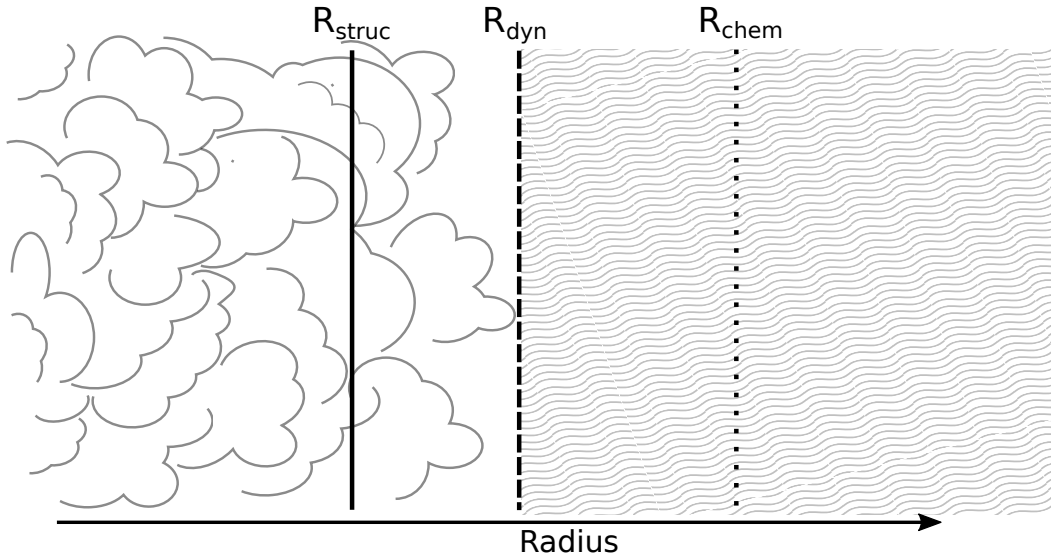


Figure 6.1: Schematics of a convective boundary. Cloudy parts represent convective motions and hatched regions indicate diffusion dominated transport mechanisms.

parameters to explore their influence as well. One of these parameters is the overshooting parameter f_{ov} , which determines the radial extent of the homogeneously mixed region surrounding CZs in 1D stellar evolution models.

We find that in 2D simulations the mixing is dominated by overturning plumes shearing along the stiff boundary of a CZ, which leads to Kelvin-Helmholtz-instabilities in the direct vicinity of the convective boundary, which has to be separated into different layers depending on the dominating mixing process. Fig. 6.1 displays a typical convective boundary, where the left most and right most regions are unstable and stable against convection, respectively. The stability is determined by the Schwarzschild stability criterion, which describes the driving of convection based on the temperature stratification. Fig. 6.1 denotes the location where the driving mechanism stops as R_{struc} . However, convective motions still penetrate to radii larger than R_{struc} . The maximum extent of these dynamical mixing events is labelled R_{dyn} . Our stellar evolution models predict a composition profile with a jump in composition in the stable layer, while the unstable layers is homogeneous. The location of the composition jump is denoted as R_{chem} in Fig. 6.1 and corresponds in our models to an increased hydrogen content in the stable layer. In simulations where there are layers with increased hydrogen content in the influence region of the shear, i.e., $R_{\text{chem}} < R_{\text{dyn}}$ we find an almost continuous flow of hydrogen into the CZ. Other mixing events by plumes that potentially penetrate farther than the shear mixing are rare. The mixing rate therefore drops when we increase the overshooting parameter f_{ov} in the initial model, i.e., when the distance between the Schwarzschild boundary of the CZ and the composition interface is increased.

However, the flow structure seen in 2D simulations is fundamentally different from that of 3D simulations. Vorticity conservation forces the flow to form large scale structures in two dimensions, while three dimensional turbulence is exhibiting smaller scale flows. Nevertheless, we showed in 5.2 that 3D simulations of convective cores also develop large scale flows on top of the small scale turbulence. Ultimately the mixing behaviour at the convective boundary is therefore rather similar in 2D and 3D simulations, which is also reflected by the matching of mixing rates obtained in 3D (5.4) and 2D (4.4). We therefore argue that it is justifiable to perform parameter studies in 2D rather than 3D in order to reduce the computing time and to allow for longer simulations.

One would expect that due to the long evolutionary time of stars on the main sequence even rare events will give rise to a significant amount of mixing, i.e., they will eventually set the size of the mixed core.

However, in 4.4 we found that even rare mixing events cannot account for the amount of mixing we see in simulations with an increased overshooting parameter f_{ov} . We identified additional diffusive mixing processes due to numerics and internal gravity

waves (IGW) that bring the composition interface in contact with the dynamical mixing events and supply the dynamical mixing across the convective boundary of matter of different composition. The hatched regions in Fig. 6.1 show the layers which are dominated by diffusive processes.

The effect of numerical diffusion can be best seen at the low end tail of the composition interface (see Figures 4.13, 4.20, and 5.10), where small amounts of hydrogen are transported close to the convective boundary. This corresponds to a diffusion coefficient of the order of $10^{10} \text{ cm}^2/\text{s}$ in the stable layer of a $3.5 M_{\odot}$ star, which is nine orders of magnitude larger than the value determined by Moravveji et al. (2016) based on asteroseismic observations. Moreover, we find similar values in simulations with smaller initial masses and also in 3D simulations, indicating that this excessive amount of diffusion is indeed a numerical effect.

A realistic source of diffusive mixing in the stable layer are IGWs. However, resolving IGWs in a low Mach number environment is numerically challenging due to their short timescales compared to those of the convective flow. Most problematic are high frequency waves that are numerically generated on the grid level, because they can be trapped in IGW cavities where they accumulate and grow to significant amplitudes. Reducing the size of the timesteps increases the fraction of well resolved IGWs and therefore reduces the amount of trapped artificial IGWs. However, such simulations are computationally very expensive. We showed in 3.5.3 that the pile up of IGWs in cavities can also be mitigated by changing the time integration algorithm of MAESTRO. Using a 4th order accurate Runge-Kutta time integrator instead of a 2nd order accurate predictor-corrector scheme reduces the velocities in IGW cavities by more than one order of magnitude.

The convective motion inside the CZ also creates IGWs, but at lower frequencies, which are properly resolved. Since we suppressed the effects of unresolved high-frequency IGWs we can analyse the diffusive mixing of resolved low-frequency IGWs by following the motion of tracer particles during the simulation. We find diffusion coefficients that are very large just outside the convective boundary, corresponding to the action of the farthest reaching dynamical mixing events. With increasing distance to the boundary the diffusion coefficients drop exponentially. This behaviour is expected and is in agreement with the mixing models used in most 1D stellar evolution codes, which describe the mixing by means of a diffusion coefficient, which is exponentially decaying with distance from the CZ boundary. In contrast to the most commonly used 1D overshooting model we find that the best fit to our simulations can be made by two connected exponential functions of different slope. The additional slope can be interpreted as an extended mixing due to IGWs. At even larger distances from the convective boundary we find that the diffusion coefficients increase again due to an increase of the amplitude of IGWs as they propagate into a less dense environment.

However, we find that the diffusion coefficients determined from the 2D simulations

are unrealistically large since they would lead to completely homogenized stars. In Chapter 5 we showed that 3D simulations with the same initial models as the 2D simulations develop convective velocities that are one order of magnitude smaller than in 2D. Consequently, the IGWs created by the convection in 3D also have much smaller amplitudes than in 2D. We therefore argue that the diffusive mixing by IGWs is largely overestimated by 2D simulations.

Therefore, it might be worth to remove a fraction of or even all of the IGWs from the stable layer in future simulations. One possible method to achieve that would be to implement a low pass filter in Fourier space thereby modifying the velocities. Removing IGWs would also allow us to simulate even longer timescales, especially in 3D, where the problem of unresolved IGWs is more persistent.

In 4.4 we showed that the mixing of hydrogen rich matter across the convective boundary in models with large overshooting parameters changes from a continuous flow to an episodic mixing, where short burst of mixing are followed by a long quiescent period. We argue that this mixing behaviour is due to a balance of diffusive mixing and rare dynamical mixing events that penetrate into the stable layer. While diffusive mixing continuously brings fresh hydrogen close to the boundary, the low end tail of this distribution is swept up by the rare dynamical mixing events and is transported across the convective boundary where it is quickly distributed across the whole CZ.

We argue again that this mixing balance is only possible due to the overestimated diffusive mixing we find in 2D simulations. Therefore, simulations that show an episodic mixing behaviour are expected to have no mixing in their natural counterpart. Indeed, we find that 3D simulations with an increased f_{ov} value show no episodic mixing in contrast to their corresponding 2D counterparts.

By comparing the mixing rates and mixing behaviours of models with varying f_{ov} it is then possible to define an upper limit for the overshooting parameter. In $3.5 M_{\odot}$ stars we find that an overshooting parameter of $f_{ov} \lesssim 0.02$ is in good agreement with our simulations as well as with empirical estimates of f_{ov} .

However, the empirical estimate does not hold for stars less massive than $\approx 2 M_{\odot}$. These stars have tiny convective cores with large pressure scale heights at the convective boundary. The formulation of the 1D overshooting model in terms of the pressure scale height therefore causes an unrealistically large overshooting layer if the empirical estimate is used. In 4.7 we showed that $2 M_{\odot}$ stars already require a significantly smaller f_{ov} value. At even lower masses we find that f_{ov} decreases further as was suggested in previous observational studies.

We were able to show that a cutoff function to the 1D overshooting model based on the radial extent of a CZ does fulfil all the limits set by our simulations. Due to the computational efficiency of 2D simulations it is possible to create a much denser grid

of simulations in the future, hopefully providing us with a functional form of f_{ov} depending either on mass or radial extent of the CZ.

In 4.5 we also investigated the idea that the mixing rate at convective boundaries is determined by the stiffness of the boundary, i.e., the buoyancy difference between the CZ and the stable region outside of the composition interface. While there seems to exist a general trend towards lower mixing rates at stiffer boundaries there does not seem to be a simple functional form to explain the dependency solely on the stiffness as it was proposed by previous simulations. There are, however, indications that the maximal mixing rate is limited by the stiffness. Such a limit would be irrelevant in long lasting stellar evolutionary phases like the main sequence or core helium burning, because there the extent of the mixed region is set by the maximal mixing distance of dynamical mixing events. On the other hand, in short evolutionary phases like oxygen burning a limited mixing rate might restrain the size of the mixed region.

In 4.6 we discussed the dependence of mixing at the convective boundary on the temperature stratification. Even though we are not able to simulate until the star is in thermal equilibrium, we showed that mixing of entropy does alter the temperature gradient just outside the convective boundary. In this so-called penetration layer the temperature stratification is found to be in between the radiative and the adiabatic temperature gradient. While we recommend to include the effects of penetration in 1D models, we cannot make a statement about the extent of this layer, because our simulations times are too short.

In future simulations one can explore the size of the penetration layer by using the same initial model, but varying the strength of the radiative energy transport. By boosting the radiative transport by orders of magnitude it is possible to force the simulation into a thermally relaxed state, which will give the right size of the penetration layer. Of course, this model is then no longer comparable to an actual star, but by varying the amount of radiative diffusion further one might be able to establish a scaling law for the size of the penetration layer and use this law to extrapolate the findings to the relevant regime for stars.

Bibliography

- Aerts, C., Christensen-Dalsgaard, J., & Kurtz, D. W. 2010, *Asteroseismology*
- Aerts, C., Mathis, S., & Rogers, T. 2018, arXiv e-prints, arXiv:1809.07779
- Almgren, A., Bell, J., & Crutchfield, W. 2000, *SIAM Journal on Scientific Computing*, 22, 1139
- Almgren, A. S., Bell, J. B., Nonaka, A., & Zingale, M. 2008, *ApJ*, 684, 449
- Almgren, A. S., Bell, J. B., Rendleman, C. A., & Zingale, M. 2006a, *ApJ*, 637, 922
- Almgren, A. S., Bell, J. B., Rendleman, C. A., & Zingale, M. 2006b, *ApJ*, 649, 927
- Almgren, A. S., Bell, J. B., & Szymczak, W. G. 1996, *SIAM J. Scientific Computing*, 17, 358
- Andrassy, R., Herwig, F., Woodward, P., & Ritter, C. 2018, arXiv e-prints, arXiv:1808.04014
- Andrássy, R. & Spruit, H. C. 2015, *A&A*, 578, A106
- Aparicio, A., Bertelli, G., Chiosi, C., & Garcia-Pelayo, J. M. 1990, *A&A*, 240, 262
- Arnett, D., Meakin, C., & Young, P. A. 2009, *ApJ*, 690, 1715
- Arthur, R. S., Venayagamoorthy, S. K., Koseff, J. R., & Fringer, O. B. 2017, *Journal of Fluid Mechanics*, 831, R2
- Baldwin, M. P., Gray, L. J., Dunkerton, T. J., et al. 2001, *Reviews of Geophysics*, 39, 179
- Baraffe, I., Pratt, J., Goffrey, T., et al. 2017, *ApJ*, 845, L6
- Batchelor, G. K. 1969, *Physics of Fluids*, 12, II
- Bell, J. B., Day, M. S., Almgren, A. S., Lijewski, M. J., & Rendleman, C. A. 2002, *International Journal for Numerical Methods in Fluids*, 40, 209
- Bertelli, G., Bressan, A., & Chiosi, C. 1992, *ApJ*, 392, 522

- Boesler, M. & Weber, N. 2017, arXiv e-prints, arXiv:1709.03158
- Böhm-Vitense, E. 1958, ZAp, 46, 108
- Boussinesq, J. 1903, Thōrie analytique de la chaleur mise en harmonie avec la thermodynamique et avec la thōrie mcanique de la lumi_re: Refroidissement et chauffage par rayonnement, conductibilit des tiges, lames et masses cristallines, courants de convection, thōrie mcanique de la lumi_re. 1903. xxxii, 625,[1] p, Vol. 2 (Gauthier-Villars)
- Bowman, D. M., Aerts, C., Johnston, C., et al. 2019, A&A, 621, A135
- Brummell, N. H., Clune, T. L., & Toomre, J. 2002, ApJ, 570, 825
- Cantiello, M., Mankovich, C., Bildsten, L., Christensen-Dalsgaard, J., & Paxton, B. 2014, ApJ, 788, 93
- Cargo, P. & LeRoux, A. 1994, COMPTES RENDUS DE L ACADEMIE DES SCIENCES SERIE I-MATHEMATIQUE, 318, 73
- Christy, R. F. 1966, ApJ, 144, 108
- Claret, A. & Torres, G. 2016, A&A, 592, A15
- Claret, A. & Torres, G. 2017, ApJ, 849, 18
- Claret, A. & Torres, G. 2018, ApJ, 859, 100
- Claret, A. & Torres, G. 2019, ApJ, 876, 134
- Colella, P. & Woodward, P. R. 1984, Journal of computational physics, 54, 174
- Constantino, T. & Baraffe, I. 2018, A&A, 618, A177
- Courant, R., Friedrichs, K., & Lewy, H. 1928, Mathematische annalen, 100, 32
- Couston, L.-A., Lecoanet, D., Favier, B., & Le Bars, M. 2018, Phys. Rev. Lett., 120, 244505
- Cristini, A., Hirschi, R., Meakin, C., et al. 2019, MNRAS, 484, 4645
- Cristini, A., Meakin, C., Hirschi, R., et al. 2017, MNRAS, 471, 279
- Deardorff, J. W., Willis, G. E., & Lilly, D. K. 1969, Journal of Fluid Mechanics, 35, 7
- Deheuvels, S., Brandão, I., Silva Aguirre, V., et al. 2016, A&A, 589, A93

- Durran, D. R. 1989, *Journal of Atmospheric Sciences*, 46, 1453
- Edelmann, P. V. F., Ratnasingam, R. P., Pedersen, M. G., et al. 2019, *ApJ*, 876, 4
- Fernando, H. J., Boyer, D. L., & Chen, R.-R. 1989, *Dynamics of atmospheres and oceans*, 13, 95
- Fernando, H. J. & Long, R. R. 1983, *Journal of Fluid Mechanics*, 133, 377
- Freytag, B., Ludwig, H.-G., & Steffen, M. 1996, *A&A*, 313, 497
- Fuller, J. 2017, *MNRAS*, 470, 1642
- Fuller, J., Cantiello, M., Lecoanet, D., & Quataert, E. 2015, *ApJ*, 810, 101
- Gilet, C., Almgren, A. S., Bell, J. B., et al. 2013, *ApJ*, 773, 137
- Gilet, C. E. 2012, PhD thesis, University of California, Berkeley
- Gresho, P. M. & Chan, S. T. 1990, *International Journal for Numerical Methods in Fluids*, 11, 621
- Grevesse, N. & Noels, A. 1993, in *Origin and Evolution of the Elements*, ed. N. Prantzos, E. Vangioni-Flam, & M. Casse, 15–25
- Guillard, H. & Murrone, A. 2004, *Computers & fluids*, 33, 655
- Hannoun, I. A., Fernando, H. J. S., & List, E. J. 1988, *Journal of Fluid Mechanics*, 189, 189
- Herwig, F., Freytag, B., Fuchs, T., et al. 2007, in *Astronomical Society of the Pacific Conference Series*, Vol. 378, *Why Galaxies Care About AGB Stars: Their Importance as Actors and Probes*, ed. F. Kerschbaum, C. Charbonnel, & R. F. Wing, 43
- Higl, J., Siess, L., Weiss, A., & Ritter, H. 2018, *A&A*, 617, A36
- Iben, I., J. 1975, *ApJ*, 196, 525
- Jacobs, A. M., Zingale, M., Nonaka, A., Almgren, A. S., & Bell, J. B. 2016, *ApJ*, 827, 84
- Jones, S., Andrassy, R., Sandalski, S., et al. 2017, *MNRAS*, 465, 2991
- Kippenhahn, R., Weigert, A., & Weiss, A. 2012, *Stellar Structure and Evolution*
- Kolmogorov, A. 1941, *Akademiia Nauk SSSR Doklady*, 30, 301

- Korre, L., Garaud, P., & Brummell, N. H. 2019, MNRAS, 484, 1220
- Kraichnan, R. H. 1967, Physics of Fluids, 10, 1417
- Kraichnan, R. H. & Montgomery, D. 1980, Reports on Progress in Physics, 43, 547
- Kutta, W. 1901, Z. Math. Phys., 46, 435
- Käpylä, P. J., Rheinhardt, M., Brandenburg, A., et al. 2017, The Astrophysical Journal, 845, L23
- Lai, M., Bell, J. B., & Colella, P. 1993, in AIAA 11th Computational Fluid Dynamics Conference, 776–783
- Lastennet, E. & Valls-Gabaud, D. 2002, A&A, 396, 551
- Lattanzio, J. C., Tout, C. A., Neumerzhitskii, E. V., Karakas, A. I., & Lesaffre, P. 2017, Mem. Soc. Astron. Italiana, 88, 248
- Lecoanet, D., Brown, B. P., Zweibel, E. G., et al. 2014, ApJ, 797, 94
- Ledoux, P. 1947, The Astrophysical Journal, 105, 305
- Li, Y. 2017, ApJ, 841, 10
- Linden, P. F. 1975, Journal of Fluid Mechanics, 71, 385
- Maeder, A. & Mermilliod, J. C. 1981, A&A, 93, 136
- Magic, Z., Serenelli, A., Weiss, A., & Chaboyer, B. 2010, ApJ, 718, 1378
- Mashayek, A., Salehipour, H., Bouffard, D., et al. 2017, Geophys. Res. Lett., 44, 6296
- Meakin, C. A. & Arnett, D. 2007, ApJ, 667, 448
- Miczek, F., Röpke, F. K., & Edelmann, P. V. F. 2015, A&A, 576, A50
- Mocák, M., Müller, E., Weiss, A., & Kifonidis, K. 2009, A&A, 501, 659
- Mombarg, J. S. G., Van Reeth, T., Pedersen, M. G., et al. 2019, MNRAS, 485, 3248
- Moravveji, E., Townsend, R. H. D., Aerts, C., & Mathis, S. 2016, ApJ, 823, 130
- Nonaka, A., Almgren, A. S., Bell, J. B., et al. 2010, ApJS, 188, 358
- Pedersen, M. G., Aerts, C., Pápics, P. I., & Rogers, T. M. 2018, A&A, 614, A128
- Plumb, R. & McEwan, A. 1978, Journal of the atmospheric sciences, 35, 1827

- Poala, A. B. 2017, Master's thesis, Ruprecht-Karls-Universität, Heidelberg
- Pols, O. R., Tout, C. A., Schroder, K.-P., Eggleton, P. P., & Manners, J. 1997, MNRAS, 289, 869
- Prandtl, L. 1926, NACA Tech. Memo, 62, 435
- Pratt, J., Baraffe, I., Goffrey, T., et al. 2017, A&A, 604, A125
- Ratnasingam, R. P., Edelmann, P. V. F., & Rogers, T. M. 2019, MNRAS, 482, 5500
- Rider, W., Kothe, D., Mosso, S., Cerutti, J., & Hochstein, J. 1995, in 33rd Aerospace Sciences Meeting and Exhibit, 699
- Robinson, F. J., Demarque, P., Li, L. H., et al. 2003, MNRAS, 340, 923
- Rogers, F. J. & Nayfonov, A. 2002, ApJ, 576, 1064
- Rogers, T. M. 2015, ApJ, 815, L30
- Rogers, T. M., Glatzmaier, G. A., & Jones, C. A. 2006, ApJ, 653, 765
- Rogers, T. M., Lin, D. N. C., McElwaine, J. N., & Lau, H. H. B. 2013, ApJ, 772, 21
- Rogers, T. M. & McElwaine, J. N. 2017, ApJ, 848, L1
- Roxburgh, I. W. 1992, A&A, 266, 291
- Runge, C. 1895, Mathematische Annalen, 46, 167
- Smeyers, P. & van Hoolst, T. 2010, in Astrophysics and Space Science Library, Vol. 371
- Spruit, H. C. 1997, Mem. Soc. Astron. Italiana, 68, 397
- Spruit, H. C. 2015, A&A, 582, L2
- Stancliffe, R. J., Fossati, L., Passy, J. C., & Schneider, F. R. N. 2015, A&A, 575, A117
- Stevens, D. E. & Bretherton, C. S. 1999, Quarterly Journal of the Royal Meteorological Society, 125, 425
- Tassoul, M. 1980, ApJS, 43, 469
- Timmes, F. X. 2000, ApJ, 528, 913
- Timmes, F. X. & Swesty, F. D. 2000, ApJS, 126, 501

- Toro, E. F. 2013, Riemann solvers and numerical methods for fluid dynamics: a practical introduction (Springer Science & Business Media)
- Turner, J. S. 1986, *Journal of Fluid Mechanics*, 173, 431
- Valle, G., Dell’Omodarme, M., Prada Moroni, P. G., & Degl’Innocenti, S. 2016, *A&A*, 587, A16
- van Ballegooijen, A. A. 1982, *A&A*, 113, 99
- Vasil, G. M., Lecoanet, D., Brown, B. P., Wood, T. S., & Zweibel, E. G. 2013, *ApJ*, 773, 169
- Ventura, P. 2007, in *EAS Publications Series*, ed. C. W. Straka, Y. Lebreton, & M. J. P. F. G. Monteiro, Vol. 26, 79–89
- Viallet, M., Meakin, C., Arnett, D., & Mocák, M. 2013, *ApJ*, 769, 1
- Vitense, E. 1953, *ZAp*, 32, 135
- Weaver, T. A., Zimmerman, G. B., & Woosley, S. E. 1978, *ApJ*, 225, 1021
- Weiss, A. & Schlattl, H. 2008, *Ap&SS*, 316, 99
- Yang, W. 2016, *ApJ*, 829, 68
- Zahn, J. P. 1991, *A&A*, 252, 179
- Zhang, W., Almgren, A., Beckner, V., et al. 2019, *Journal of Open Source Software*, 4, 1370
- Zingale, M., Almgren, A. S., Bell, J. B., Nonaka, A., & Woosley, S. E. 2009, *ApJ*, 704, 196

Acknowledgments

First and foremost I want to thank my supervisors Achim Weiss and Ewald Müller for giving me the opportunity to do this thesis project, and for encouraging me to keep moving forward even though they had to look at the same (unsatisfying) plot every week.

I also want to thank all my colleagues at MPA, especially the people from the stellar group, for all the scientific and non-scientific discussions we had during the last five years.

A special thanks also goes to my current and previous flat mates in the "Super Awesome WG" in Mintraching for the enjoyable time and long discussion sessions we had together. See you all in Argentina next year!

Zu guter Letzt möchte ich auch noch meinen Eltern Hans und Ursula Higl und meinen Brüdern Martin, Simon und Ulrich dafür danken, dass sie mich immer meinen Weg gehen ließen und mich darüber hinaus bei jedem Schritt unterstützt haben.